UNIVERSITÀ degli STUDI di CATANIA

PhD programme in MATERIALS SCIENCE AND NANOTECHNOLOGIES

Alberto Sciuto

Advanced laser annealing methods, from complex materials to nanoscale transport

PhD thesis

Supervisors:
Prof. ssa. Mara Grazia Grimaldi
Dr. Antonino La Magna

---

academic year 2021/2022

To live is to risk it all; otherwise you're just an inert chunk of randomly assembled molecules drifting wherever the universe blows you.

R.S

Per Luigi

Contents

1 Introduction **5**

2 LIAB: a powerful TCAD assisted simulation tool for Laser Thermal Annealing **15**

2.1 Optical excitations and relaxation phenomena and ultra-short laser pulse 15

2.2 Thermalization approximation and self-consistent electromagnetic calculations for the heat sources in laser annealing 18

2.3 Melting processes in laser annealing TCAD simulation . . . 21

2.3.1 Liquid-Phase transition fundamentals: free energy barrier, nucleation and evolution 22

2.3.2 Phase field and enthalpy formalisms 24

2.3.3 Simulation examples of melting processes in 1D, 2D and 3D systems 27

2.3.4 Advanced features: Impurity and Dopants evolution 30

2.4 LIAB workflow, basics and evolution 38

3 Simulations with complex materials, SiGe case study **41**

3.1 Calibration of the optical constants in SiGe 43

3.2 Benchmark of heat source calculations in patterned structures 50

3.3 Study of SiGe patterned structures and complex devices . . 55

4 Nanoscale effects on thermal transport **69**
4.1 Basic formulation 71
4.2 Heat transport model 74
4.3 Effective conductivity analysis 77
4.4 Model Validation with non equilibrium molecular dynamics 82
4.5 Simulations of complex systems 84

5 Simulations with complex dynamics: 2D explosive crystallization **91**

6 Conclusions **101**

7 Parameters **105**

Bibliography **115**

Acknowledgements **129**

Chapter 1

Introduction

A critical step in qualifying laser irradiation for use in nano-electronic applications and device fabrication is the ability to predict the alteration of materials and structures generated by the laser beam. The lack of integration of reliable and complete Laser Annealing (LA) simulators (including material calibration) into commercial Technology Computer Aided Design (TCAD) tools, which are commonly used in the technological development of devices, is still the most significant bottleneck preventing the widespread use of LA in micro- and nano-electronics.

One seemingly contradictory element of the current claim for the use of the LA is that the appeal of this process rises in tandem with the essential issue of its control, which appears to be a contradiction in terms. To be sure, the demand for LA features as a viable alternative to conventional thermal processes grows as the complexity of the device structures to be processed increases: it is not difficult to imagine that the irradiation effects in complex 2D/3D distributions of different materials are difficult to predict/control. Furthermore, in order to achieve a successful process integration, it is necessary to undergo a thorough retraining even in the case of minor design changes throughout the development of the same device class (i.e. in the case of new device generations).

For example, when an advanced device design requires some components to be placed on top of pre-fabricated layers that could be harmed if the heating stretches across the entire wafer, a query for targeted heating, which LA can ensure, is called. The propagation of the electromag-

netic (em) field, its absorption, and all of the phenomena activated by the structure-em field interaction are, without a doubt, vitally dependent on the geometry and material design of the devices, which are typically complex and difficult to construct.

Aside from the essential dependence of the LA process feature on the device design, the paradigm of "interest vs crucial control" occurs in other commonly invoked applications of this particular manufacturing method . Indeed, the activation of phase transitions (which are frequently confined and ultra-fast) is another major application class for LA technology. In this class, we find the classic LA application in semiconductor doping, i.e., the high dopant activation above the solubility level after melting and crystal regrowth [1, 2, 3], but also more difficult and critical applications such as the (explosive) crystallization of amorphous nano-structures or the formation of silicides when processing a metal layer deposited on semiconductive substrates

Beyond the difficulty of predicting phases and chemical component evolution during LA, ultra-fast phase transitions are also associated to the unusual behavior of the physical observables of interest, which should be studied and regulated as part of the whole process. Among these are the alloy redistribution [4, 5, 6, 7], the electrical activation of ion-implanted impurities [8, 9, 10], the defect evolution [11, 12, 13] and the observation of non-conventional extended defects [14, 15].

LA, in any case, induces a kinetics in the irradiated materials that is far from equilibrium, and the benefits of this non-equilibrium phenomenon (i.e., the potential process performance that is far beyond conventional annealing) are outweighed by the difficulties in process control, particularly if the process design is based solely on experimental Design of Experiments (DoE) procedures, as is the case with most DoE procedures.

Many of these far from equilibrium phenomena necessitate the use of atomistic techniques such as Molecular Dynamics or Kinetic Monte Carlo simulations for proper modeling. However, it is difficult to achieve a complete TCAD simulation of the LA process using only atomistic techniques because structures with multi-space scales react to the irradiation (for example, accurate simulations of nanostructures melting are only possible if the temperature field evolution is computed on the close-to-millimetre scale of wafer thickness is taken into account). Furthermore, in many cir-

cumstances, it is impossible to describe the entire process time scale (including the quenching stage and the pulse to pulse time in a multi-pulse mode) using atomistic simulations. As a result, continuum modeling, which is also merged with more realistic atomistic simulation findings, is a critical tool for the predictive knowledge and management of the LA process, among other things.

Our discussion will focus on the current state-of-the-art in continuum modeling of laser annealing (LA), utilizing the key characteristics contained in the core of LIAB, a tool that we created in collaboration with LASSE, an industry leader in the development of laser annealers. We are able to forecast the ultra-rapid evolution of average fields that are related to the micro-structural and atomistic evolution of the processed systems by employing this tool. The main focus of the thesis will be on the LA modeling of structures and materials that are relevant to nanoelectronics. In any case, the modeling methodologies are frequently convertible to different technological applications of LA, which is a positive development.

In the mid-1970s, Russian scientists proposed laser annealing as a new approach for activating dopants and removing damage in ion-implanted semiconductors [16, 17]. By the end of the 1970s, it had become a hot topic, and laser processing was mostly used for annealing ion-implanted layers, which was a big concern for the semiconductor industry at the time. Early experiments were carried out utilizing a pulsed Q-switched ruby (694 nm, 1.79 eV) laser with pulse durations in the tens of nanoseconds. Irradiation of ion implanted Si resulted in recrystallization of the amorphized silicon layer and activation of the implanted dopant impurities over a specific fluence.

Initially, two primary theories were presented to explain these findings: the melting model and a putative mechanism based on a highly excited electronic system that may keep its excitation for tens or hundreds of nanoseconds in the form of a 'hot dense plasma.' However, a variety of experimental evidences, including as time-resolved reflectivity, time-dependent Raman scattering, time-dependent X-ray Bragg scattering, and time-dependent electrical resistivity, clearly demonstrated that the melting model accurately represents the phenomenon. In reality, the energy delivered by the laser field to the electronic system is promptly

converted to phonons in less than 1 picosecond, resulting in melting of the near surface region.

The first focus of laser semiconductor processing was on the annealing of ion implanted layers in order to solve several implant-related issues, such as heating the entire sample to restore crystalline order. Laser irradiation enables for the heating of only the sample's surface without causing bulk deterioration of the substrate. The following are some of the benefits of pulsed laser processing: a "near-zero" thermal budget (due to laser pulses lasting only tens of nanoseconds); the extent of dopant diffusion is controlled by the melt depth (with negligible diffusion in the adjacent solid substrate); active dopant concentrations can exceed the solid solubility limit [18].

Laser annealing was a prominent issue in the late 1970s and early 1980s, and thanks to numerous research, it was possible to precisely establish the phase diagram of crystal, amorphous, and liquid Si over a wide range of temperature, quenching rate, and solidification velocity. It has been demonstrated that a-Si melts at temperatures 200 K below the crystalline melting point, and that a phenomenon known as explosive crystallization (EC) is triggered by the latent heat released by the resolidifying surface, resulting in a self-sustaining melting front towards the underlying a-Si [19, 20]. Measured pulsed laser processing quenching rates of the order of 1010 K/s have been reported, and at high interface velocities, above 20 m s-1, undercooling can drive the formation of a-Si.

In general, ion-implantation causes crystalline structure damage or amorphization, while laser irradiation causes structural alterations to the a-Si layer on crystalline silicon (c-Si). Various scenarios can be observed depending on the energy density: 1) When the energy density surpasses the melting point of the a-Si surface, EC is activated, converting the a-Si layer into fine grain polycrystalline silicon (FG-polysilicon). EC is triggered by the latent heat released by the resolidifying surface towards the underlying a-Si [21, 22], with the self-propagating buried liquid layer moving into the a-Si at a speed of 11-13 m/s [23, 24].

We note that, because amorphous silicon undergoes transformation into FG-polysilicon prior to primary melt propagation [21, 22], the melting temperature of irradiated film reported in literature (1500 K) [25] can be related to melting temperature of FG-polysilicon produced by explo-

sive crystallization, which results in a temperature well below that of c-Si; 3) by increasing the energy density, the maximum primary melt depth propagates into the FG-polysili If the FG-polysilicon layer is partially melted, resolidification begins at the solid/liquid interface, with epitaxial regrowth from FG-polysilicon. Because of the inherent inhomogeneities of the FG-polysilicon layer, the regeneration process will begin at random. If the energy density is high enough to melt the entire FG-polysilicon, resolidification will begin at the c-Si, resulting in epitaxial regrowth of the implanted layer [26, 27]. Melting a portion of the c-Si substrate guarantees epitaxial development of a substantially defect-free crystal with few "quenched-in" interstitials [28].

Despite the benefits of pulsed laser annealing of ion-implanted wafers, laser irradiation in the melt/regrowth regime was not widely used in the microelectronics industry since rapid thermal annealing (RTA) established in the solid phase regime could meet the technical requirements at the time. Indeed, RTA can heat wafers of any size, cassette to cassette, in seconds to eliminate damage, activate the implanted species with limited diffusion, and produce thin dielectric and/or metallic layers.

However, during the mid-1980s, a novel application of pulsed laser annealing to create the active layer of polycrystalline silicon thin film transistors was presented (TFTs). Over the last 40 years, polysilicon TFTs technology has been extensively researched for applications in active matrix liquid-crystal displays and, more crucially, active matrix organic light emitting displays, a technology that is now widely used in mass production of mobile phone displays. The Sony group [29] was among the first to demonstrate the ability to use excimer laser irradiation to convert thin (on the order of 10 – 100 nm) a-Si films placed on glass into polysilicon. The introduction of such technology resulted in a significant boost in the performance of polysilicon TFTs, resulting in electron field-effect mobilities greater than 100 cm2 (V s)-1.

Excimer lasers proved to be a critical tool in the amazing advancement of polysilicon TFT technology due to their main characteristics: UV light emission (output wavelengths 193 nm, 248 nm, and 308 nm for ArF, KrF, and XeCI gas combinations, respectively) with a short pulse duration (10-30 ns). The breakthrough made in excimer lasers and optical systems to manage laser beams aided in the industrialization of polysilicon TFT

technology. In the following part, we will go over some of the more important components of such technology. The combination of intense UV light optical absorption (> 106 cm^{-1}) and short heat diffusion length during the laser pulse (100 nm) in Si suggests that high temperatures can be formed in the Si surface region, inducing melting, without significant heating (400 °C) of the substrate. As a result, the excimer laser annealing method can be used on glass or even plastic substrates . Another advantage is that the polysilicon produced by the melt-regrowth method has outstanding crystallinity with minimal in-grain flaws, allowing for great device performance.

In the early 2000s, the increasingly rigorous requirements of c-Si metal-oxide-semiconductor technology, driven by device geometries downscaling, created the dilemma of finding an alternate approach to RTA to form ultrashallow junctions. Indeed, at nodes smaller than 90 nm, source/drain (S/D) abrupt junctions shallower than 50 nm with sheet resistance less than 500 were required to reduce short channel effects and the transistor's on-resistance.

Conventional RTA or even high-ramp-rate (400 C/s) short-time (1 s) high-temperature (> 1000 °C) "spike" annealing failed to create ultrashallow junctions due to nonequilibrium diffusion (transient-enhanced diffusion). This resulted in a revived interest in pulsed laser annealing for MOS applications , not only because of the process's key advantages, but also because of the great advance in excimer laser technology, pushed by the display sector, that occurred in the meanwhile. Excimer laser annealing in the melting regime has several advantages over alternative nonmelting-based techniques, including precise control over junction depth, greater dopant activation, and profile abruptness.

In reality, when Si is irradiated with sufficient energy density by laser light, a well-defined melted zone with a sharp transition from liquid to crystal phase is generated. Dopant diffusivity increases in the liquid state (2104 cm2/s), and the dopants can disperse uniformly throughout the melted layer, resulting in boxlike profiles following regrowth. Because of the large heat gradient between the liquid and solid phases, the liquid-crystal interface advances toward the surface at a velocity of 3 m/s soon after irradiation.

Because of the quick solidification (low-temperature solid-phase re-

growth is generally 1.5 1010 m/s at 550 C), less dopant is segregated into the liquid phase at the liquid-crystal interface, and dopant trapping is improved. Segregation (during regrowth), evaporation (during the melting phase), and ablation all influence the fraction of the implant dosage maintained within the semiconductor during ELA (during energy deposition). Electrical activation of the residual dopant in the regrown layer after ELA is finally limited by morphological instability at the liquid-crystal interface during regrowth, lattice strain, and thermodynamic limits. Several groups have reported on a variety of investigations for the creation of ultrashallow junctions, as well as process integration challenges in MOS-technology.

By the late 1990s and early 2000s, the semiconductor industry, which had a global revenue of around 250 billion euros at the time and supported a global market of more than 6 trillion euros in terms of electronic systems and services, was beginning the transition from microelectronics to nanoelectronics. The new era of nanoelectronics raised the ICT (Information and Communication Technology) society to unprecedented heights during that time period and enabled Europe's vision of Ambient Intelligence, i.e. living environments that are aware of our presence and responsive to our needs, is being realized. As a result, innovative solutions were required for the major device, process, and materials integration challenges for the technologies planned for the coming years. However, many issues had to be addressed in order to achieve technology nodes below 65 nm, such as short channel effect (SCE), gate leakage, and mobility degradation, and simple scaling down without proper optimisation based on experiments and simulation would have been useless. Furthermore, several device parameters, including contact and wiring resistances, were approaching their physical or technical limits: gate oxide thickness, source/drain junction depth, and parasitic resistance. As a result, the traditional scaling scheme came to an end, and a new one began. To improve VLSI performance even further, new material and/or processing concepts had to be presented.

To control the SCE and sub-threshold performances, the sub-90 nm MOSFET architecture required ultra-shallow junctions and the design of 2D dopant profiles. Indeed, the formation of ultra-shallow source-drain extensions with high doping levels and optimal dopant distribution in

the channel zone allows for the reduction of the parasitic effect of threshold voltage roll-off versus channel length decrease. Alternative annealing techniques were unquestionably required for technology nodes in the early 2000s. If it was a matter of 'courage,' Flash Lamp Annealing and/or Non Melting LTP with ultra violet or infrared sources were an extension of the now-defunct Rapid Thermal Annealing method, whereas the use of melting ELA required a significant effort of integration but provided doping profiles with distinct characteristics.

Thermal diffusion and inadequate dopant activation are limitations of conventional rapid thermal annealing (RTA). While maintaining up with Moore's Law meant reducing processing times, the 45 nm node required processing times of 10 ms or less, with almost no diffusion. This was beyond the present processing regime of lamp-based RTP systems, restricted to 1 s processing time. Fabricating ultra-shallow p+/n junctions was thus one of the primary hurdles for sub-65 nm pMOSFET manufacture. In addition to the deep junction and high doping level, a 2.5 nm/decade lateral abruptness was required to reduce the spreading resistance and hence the total resistance of the MOS circuit. The criteria for CMOS technology at the time were addressed by using low-energy ion implantation and the "spike annealing" approach. This allows for very fast ramp rates (250 °C/s) and very short soak annealing times. However, the resulting junction depth, electrical activation, and profile abruptness were unsuitable for following technology nodes. The proposed alternative used excimer laser annealing to generate ultra-thin abrupt junctions with strong electrical activity. Despite the fact that ELA systems were relatively developed at the time (see previous section), this technique had major technology integration challenges.

This strategy could potentially suit the needs of technological nodes. Many entries in the ITRS were red for technology nodes below 100 nm. Affordability, gate stack, junction depth, sheet resistance at contact and extension, power dissipation, and power dissi A fundamental challenge with the ELA approach remained its integration with the process steps and materials utilized for device manufacture. The interaction of the laser beam with doped silicon and the device's components, such as dielectrics, metal contacts, and polycrystalline silicon, was studied extensively. Determining lateral diffusion of doping contaminants beneath a mask was

thus explored in one and two dimensions. A manufacturing flow for the fabrication of a MOS device that incorporates the ELA method was finally developed and implemented. This included the evolution of the thermal field and dopant dispersion during ELA and subsequent quenching.

By suppressing lateral diffusion of the dopant, the Si melting regime reduces the short channel effects and size scaling. A real benefit over alternative annealing procedures could be established, influencing future technology requirements. However, in terms of device integration, this approach posed difficult hurdles.

In this context of a rapdly changing industry it was also possible to develop reliable computational packages, which were designed to be coupled and integrated with existing codes for process simulation. These packages were capable of simulating the interaction between the laser beam and the silicon device, including the evolution of the thermal field and dopant distribution during the ELA process and the subsequent quenching.

Our work follows the road paved by these early developers to achieve a reliable solution to simulate the full Laser Anneal process.

Chapter 2

LIAB: a powerful TCAD assisted simulation tool for Laser Thermal Annealing

The following is the chapter's organizational structure: We discuss briefly in sections 1-2 how the code deals with laser-matter interaction, taking into account optical excitations of electrons in solids activated by photons with $\sim$eV energies and the inner interaction leading to energy transfer from the electron system to the phonon bath (also known as thermalization); in section 3, we discuss the modelling of LA processes inducing the crystal-liquid-crystal phase transitions, focusing primarily on the computational complexity of non-equilibrium impurity kinetics and activation. Finally we will discuss how the code actually works, and the differences before and after my PhD work.

2.1 Optical excitations and relaxation phenomena and ultrashort laser pulse

Although not fundamental to our scope and far from the actual implementation of laser heating in LIAB, this section provides a brief overview of the main processes that occur in laser matter interaction, particularly

when using an ultrafast pulsed configuration with the specific scope to insert the thermalization approximation in the proper context. The current state-of-the-art TCAD models for LA assume this approximation, which in turn allows for affordable numerical simulations of the process also in complex device structures. Laser-induced changes in solid materials are complex processes [30, 31]. The excitation characteristic is largely reliant on pulse duration. Using ultra-short laser pulses, non-equilibrium energy distributions with high excited state populations can be created. It is possible to affect the structure and morphology of materials by using ultrafast processes that occur in laser–solid interactions. The work of [32] presents a thorough computational framework for the modeling of optical excitations and the following phonon-induced relaxation dynamics of nonequilibrium electrons.

Ultrashort laser pulses can study electron dynamics in solids or near surfaces on time scales of tens of femtoseconds. In rare circumstances, where only a few discrete channels for energy dissipation are available, coherent evolution of excited states of systems can be seen. Relaxation mechanisms break phase coherence and generate quasi-equilibrium electron distribution functions. While the system's coherence and subsequent relaxation dynamics necessitates a DMT description, the well-defined excitation energies allow for a quasi-particle band structure description. Calculating the quasi-particle band structure requires a self-consistent electronic structure computation as a starting point. Even while a single-step theory like time-dependent Density Functional Theory can theoretically describe excited state dynamics, it is computationally difficult and currently relies on approximations. Alternatively, we can utilize a two-step technique where DMT describes the relevant degrees of freedom of dynamics while DFT describes the microscopic processes (input as parameters into DMT equations). The density matrix theory-derived dynamical equations for ultra-fast solid response are valid for any multi-band system with any phonon mode. This generic framework enables for flexible dynamics modeling, either by maintaining only a few bands and fixing the remaining parameters empirically, or by working with an ab initio description of the electronic quasi-particle band structure and phonon modes. DFT can describe the surface atomic structure realistically. We can apply many-particle perturbation theory for excited states (GW ap-

proximation for single quasi-particle states and Bethe–Salpeter equation solutions for two-particle states [33]). The electron–electron interaction of optically stimulated states can also be used in the DMT equations [34].

The complete quantum technique described above is required to describe fs pulse phenomena, but not for longer laser pulses. A compromise between pulse duration and numerical method accuracy leads to reliable results with repeated approximations for extended irradiation.

The following qualitative factors justify the switch from quantum to semi-classical description. Initially, the initial electronic excitation causes a temporary coherent polarization. A de-phasing operation of 10 fs destroys this polarization. In the following 100 fs, non-thermal carrier-carrier interactions modify these states' occupation. The heated electron state emits phonons to cool. In 1 ps, electrons cool and phonons relax. Then thermal cooling happens > 1 ps.

Semi-classical approaches using the particle-like Monte-Carlo technique may accurately simulate charge carrier dynamics for pulses 10^{-12}-10^{-10} in duration. These methods use established band-structure and electron-phonon coupling characteristics. Time-dependent Maxwell equations can be closed form solved using carrier semi-classical evolution with electron-hole production.

However, The local average energy $Eave(t)$ of the overall electrons in the bands deviates from the pure ballistic energy $(Erms)$ due to different scattering events, leading to a different estimate of self-consistent optical coefficients. With pulsed irradiation, the electron energy distribution is asymmetrical compared to the electromagnetic one.

This stochastic simulation model may assess energy transfer from the electron system to the phonon bath. The electron system has an equivalent average temperature *Te* (electron temperature) orders of magnitude higher than the lattice system ($kTe \sim 1eV$ and maximal electron energy of order of several eVs).

A calibrated continuum model for pulses of this time employs two temperature fields, *Te* and *T* [35, 36]. The electron temperature *Te* converges towards the lattice temperature, i.e. $TesimT$, for long time scales $\sim 1ns$ and smooth fluctuations of the laser power density. The thermalization approximation ignores the delayed mediation by the electron system and uses the entire absorbed laser energy as a temperature source.

When compared to fs excitation, nanosecond pulses excite electrons in a very different way. Excited electrons transmit energy to the lattice during the duration of electron excitation when a ns pulse delivers energy to a material. Throughout the excitation process, electrons and the lattice are in equilibrium. During the duration of the laser pulse, the ns laser heats the solid to its melting point. Unlike fs absorption, the ns absorption processes are linear and have a substantially longer absorption length. Deeper melt depths may result from linear absorption. The ns-induced temperature difference between the molten layer and the solid substrate is lower and spread over a longer distance than in the fs-laser situation. As a result, the melt time is longer and the resolidification front speed is slower, resulting in a crystalline structure. For both ultrafast and ns lasers, absorption is caused via multiphoton absorption if the laser wavelength is transparent to the medium. When compared to an ultrafast laser, the ns laser will have a deeper penetration depth due to a smaller absorption cross section. For both lasers, the penetration depth for opaque materials is defined by the absorption coefficient owing to single-photon absorption. Due to a mix of linear and nonlinear absorption, an ultrafast laser with a modest absorption coefficient may have a shorter penetration depth.

2.2 Thermalization approximation and self-consistent electromagnetic calculations for the heat sources in laser annealing

It is possible to assume the spatial distribution of electromagnetic power to be uniform over areas of approximately cm^2 when laser annealing is performed with pulsed laser setups.The c oherence length Lc of the electromagnetic field is generally much smaller than the pulse dimension $Lc << 1cm$, but much bigger than the feature size of irradiated objects in general. This disparity in dimensions allows the heat source to be approximated as the one generated by a generic incident coherent electromagnetic plane wave with set angular frequency ω in a given polarization state, which may be described as follows: the total fluence (energy den-

sity) E_{laser} in [J/cm^2] units and the normalized power density $P_{norm}(t)$ of the laser pulse.

$$[H] \int_0^{\Delta t_{pulse}} P_{norm}(t)dt = 1 \tag{2.1}$$

where $P_{norm}(t) = 0$ when $t < 0$ or $t > \Delta t$.

For pulse duration longer than $\sim 1ns$ and photon energy of $\sim 1eV$, Δt_{pulse} is usually much larger than the inverse of the frequency

$$\nu^{-1} = (\omega/2\pi)^{-1} = (c/\lambda)^{-1} \tag{2.2}$$

where ω denotes the angular frequency and c denotes the speed of light. These constraints render any fully time dependent solution of the Maxwell equations worthless for calculating absorbed energy. A simple "adiabatic-like" formulation of the heating problem suffices, providing that the change in optical constants during annealing is slow in comparison to the system reaction to the electromagnetic stimulation. With the additional assumption that electromagnetic excitation is efficiently transmitted from electrons to photons, in this approximation we can determine the heat sources using a stationary (or time-harmonic) evaluation of the resistive heat averaging the "ultra-fast" time scales of the oscillating electromagnetic field

$$S_{laser}(t,r) = \frac{\varepsilon^{''}}{2\rho}|E^{th}(r)|^2 \cdot P_{norm}(t) \tag{2.3}$$

where $\varepsilon^{''}$ is the imaginary part of the complex dielectric constant $\varepsilon = \varepsilon^{'} + j\varepsilon^{''}$ of the material and E^{th} is the time-harmonic electric field $E = E^{th} \times exp(-j\omega t + \phi)$ that can be evaluated by the following time independent form (i.e. the time-harmonic Maxwell curl-curl problem)

$$\nabla \times (\mu^{-1}\nabla \times E^{th}) - j\omega(\sigma - j\omega^{''})E^{th} = j\omega J, \quad in \quad \Omega \tag{2.4}$$

and

$$n \times E^{th} = n \times E_0^{th}, \quad on \quad \delta\Omega_e \tag{2.5}$$

$$n \times (\mu^{-1}\nabla \times E^{th}) + j\omega n \times (\lambda(n \times E^{th})) = j\omega J_f + j\omega n \times H_0, \quad on \quad \delta\Omega_h \tag{2.6}$$

where

$$\delta\Omega = \delta\Omega_e \cap \delta\Omega_h \tag{2.7}$$

and

$$\delta\Omega_e \cup \delta\Omega_h = 0 \tag{2.8}$$

here Ω is an open, bounded domain with boundary $\Gamma = \delta\Omega$,$\delta\Omega_e$ and $\cup\delta\Omega_h$ are respectively boundaries where a condition on the electric or magnetic field is applied, J is the internal source and n is the outward normal vector to the boundary. We can modify Eq. 5 with the relations:

$$E^{th} = E_z^{th} z \tag{2.9}$$

$$\frac{\delta E^{th}}{\delta z} = 0 \tag{2.10}$$

Obtaining the Helmotz equation:

$$-\nabla(\mu^{-1}\nabla E_z^{th}) - j\omega(\sigma - j\omega\epsilon)E_z^{th} = 0 \tag{2.11}$$

and

$$E_z^{th} = E_0^{th}, \quad on \quad \delta\Omega_e \tag{2.12}$$

$$-n \cdot \nabla E_z^{th} - jkE_z^{th} = j\omega n \times H_0, \quad on \quad \delta\Omega_h \tag{2.13}$$

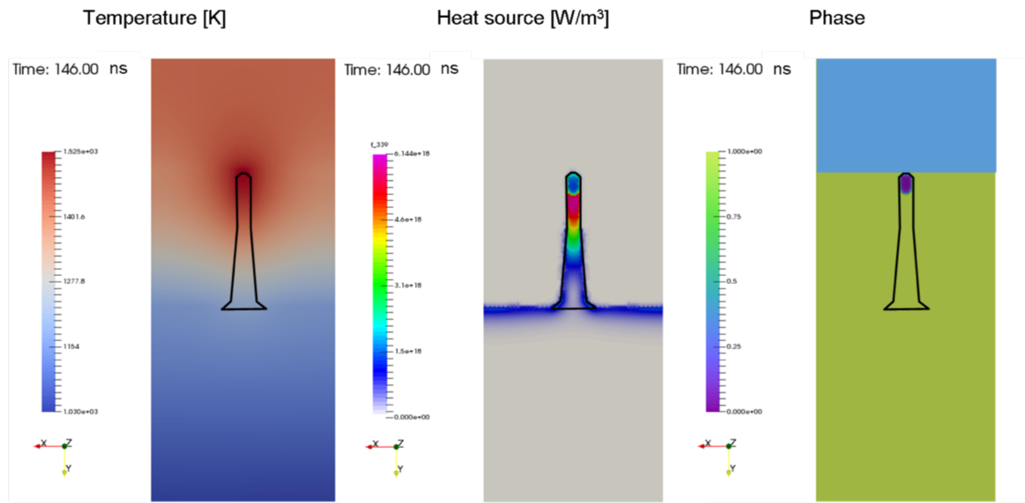

Figure 2.1: Temperature, heat source, and phase field pictures for a 135 nm FinFET irradiated at 0.6 J/cm^2 fluence and 90 degree polarization (transverse magnetic) at t=146ns, from left to right. Green indicates the solid domains in the phase field section, whereas violet represents the liquid domains. The shape of the FinFET structure is represented by the black line. [37]

2.3 Melting processes in laser annealing TCAD simulation

Transient and localized melting enhances the potential functions of the laser process by activating phenomena that are either too slow or do not occur in the solid phase of the material being melted. Obviously, controlling a laser process in the melting regime is much more complex, and TCAD techniques should take into account the nucleation and growth of the molten front, as well as the modeling of all of the aforementioned events and processes. Specifically, we will examine simulations for two-phase boundaries (i.e., solid-liquid or liquid crystal) with a particular emphasis on the doping of elemental semiconductors, such as Si or Ge

semiconductors, and a changing impurity density profile.

2.3.1 Liquid-Phase transition fundamentals: free energy barrier, nucleation and evolution

Melting/solidification is a first order phase transition caused by an energy imbalance between the material's solid/liquid free energies at a particular temperature TM. Within the Landau-Ginsberg formalism, a proper generic continuum formulation of the free energy $F(\phi, T)$ behavior can be obtained, where $F(\phi, T)$ is a double minimum function of an order parameter ϕ, with the minimum at $\phi = 0$ representing the liquid phase and the minimum at $\phi = 1$ representing the solid phase. A possible expression for $F(\phi, T)$, which forms the basis of the phase field model [2] used in the melting simulation [1]

$$-F(\phi, T) = f(\phi) + g(\phi)\, U(T - T_M) \tag{2.14}$$

where

$$f(\phi) = -\phi^2 (1 - \phi)^2 \tag{2.15}$$

$$g(\phi) = 8\left(\frac{1}{3}\phi^3 - \frac{1}{2}\phi^4 + \frac{1}{5}\phi^5\right) \tag{2.16}$$

and $U(T - T_M)$ a drift term which is 0 for $T = T_M$ and $U > 0 (U < 0)$ for $T > T_M (T < T_M)$.

The free energy function's behavior is depicted in Fig. 2.2. At $T = T\ M$ (green curve), the two minima separated by a free energy barrier are degenerate, whereas the absolute minimum is reached at the correct ϕ typical of the two phases$T < TM$ (blue line) and $T > TM$ (red line). The free energy barrier encapsulates the original event's nucleation mechanism: for example, a model based on Eq. 2.14 will preserve the solid value of ϕ even when $T > TM$ until the first liquid nucleus occurs. The mechanism of nucleation and the associated barrier are extremely challenging to examine using atomistic simulations. Only recently has the nucleation been examined using a Machine-Learning study of Molecular Dynamics (MD) Si trajectories [38] (see, for example, Fig. 2.2 (b)), validating the Landau-Ginsberg approach's reliability.

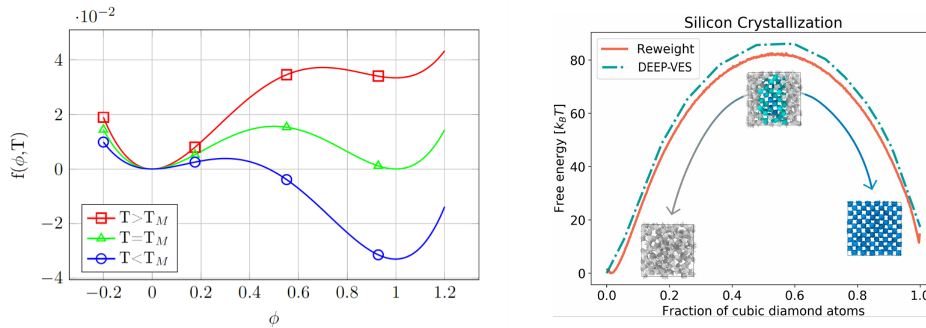

Figure 2.2: (a) The free-energy density F(ϕ T) of eq 2.14, displayed as a function of three values of temperature near the melting temperature T_M: for $T < T_M$, $T = T_M$ and $T > T_M$. (from S.L. Lombardo PhD Thesis [39]) (b) Machine Learning MD estimated Liquid/Solid free Energy barrier in Si. (From. Luigi Bonati, Yue-Yu Zhang, and Michele Parrinello PNAS September 3, 2019 116 (36) 17641-17647; Ref. [38]

Notably, consistent with the nucleation theory nature of the phase field-based formalism, the Landau-Ginsberg approach can also take into account the relative stability of the nucleated phase with respect to the nucleus size, for example, curvature effects in the kinetics of the evolving phase (for a detailed discussion, see the seminal paper [40]).

As a result of the preceding discussion, it is clear that under transient and strongly non-equilibrium conditions, the liquid/solid interface is not always equivalent to the one defined by the $T = TM$ condition, whereas under equilibrium, the thermal field's TM level set coincides with the melting front. As a result, a completely valid theory should additionally account for the interface speed's reliance on T. Fig. 2.3 illustrates a Fulcher-Vogel type expression fitted to experimental data for amorphous and crystal Si. Close to $T_T M$, the curves are approximately linear with a maximum in the under-cooling area (($T < T_M$) and monotonically increasing in absolute value as $T > TM$.

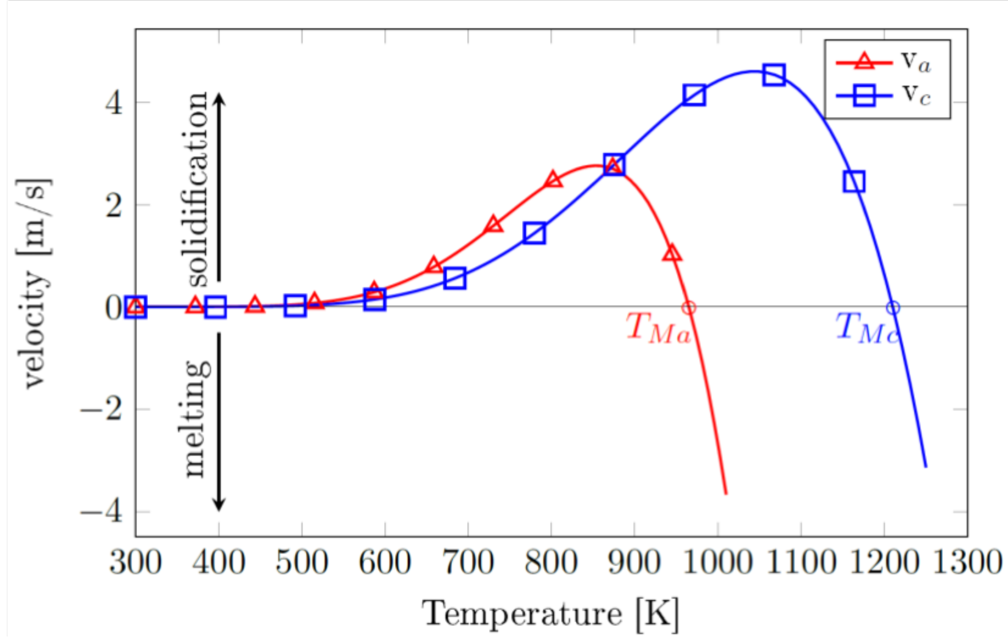

Figure 2.3: Interface speed for the crystalline (blue line and squares) and amorphous (red line and triangles) phases. In accordance with each phase's melting temperature, the velocity goes to zero.

2.3.2 Phase field and enthalpy formalisms

We now introduce the features of melting/solidification by means of the phase field formalism.

The derivation is reported in several papers (see e.g. Ref. [41] Here we begin our discussion with the coupled PDEs:

$$\tau \frac{\partial \phi}{\partial t} = W^2 \nabla^2 \phi - \frac{\partial f}{\partial \phi} - U \frac{\partial g}{\partial \phi} \tag{2.17}$$

$$C(T) \frac{\partial T}{\partial t} = \nabla \left[k_{bulk} \left(\phi, T \right) \nabla T \right] + 30 L \phi^2 \left(1 - \phi \right)^2 \frac{\partial \phi}{\partial t} + S \tag{2.18}$$

where Eq. 2.17 is a diffuse interface equation in which the thickness of the solid/liquid front is determined by W, and the temperature equation

Eq. 2.18 phase includes a latent heat L term that is appropriately expressed so that the correct amount of latent heat is consumed (released) during melting (solidification).

Once a reliable nucleation model is integrated into the formalism (i.e. a method that allows for the stochastic formation of the early nucleus of the other phase citeLombExp in the deterministic PDE-based approach), the phase-field equations allow for an accurate continuum modeling of the melting kinetics.

Numerical integration of nonlinear Eqs. 2.17 and 2.18 phase may require a significant amount of CPU time, particularly for big and complicated 2D and 3D systems. As a result, approximated methods are frequently used in the class of so-called "Enthalpy" methods, which are trustworthy for flat liquid/solid interfaces and evolution close to equilibrium [42]. The "Enthalpy" method is based on a heat equation formally written as energy conservation law in terms of the (volumetric) enthalpy H:

$$\partial_t H + \nabla \cdot \overrightarrow{Q} = S \tag{2.19}$$

where H denotes the enthalpy per volume unit, $\overrightarrow{Q}$ denotes the heat flux, and S denotes the heat source. This law enables the determination of heat and phase transitions, as latent heat is incorporated in the enthalpy formulation. This equation, however, must be linked with an appropriate equation for the relationship between H and T. A more straightforward similar derivation [43] employs a modified C_p function in the Fourier Law that includes the heat absorbed (released) by phase transitions. The discontinuity of the modified C_p function's jump in the transition zone is critical for determining the interface's position. The latent heat change in the C_p function of T is incorporated into this enthalpy model formulation via a suitable Gaussian approximation of the associated Dirac δ function. As a result, the $C_p(T)$ function can be expressed as follows:

$$\widetilde{C_p} = C_p(T) + \frac{1}{T\sqrt{\pi}} e^{-\left(\frac{T-T_M}{\Delta T}\right)^2} L_f \tag{2.20}$$

with TM denoting the melting point, Lf indicating the latent heat of fusion, and ΔT representing the width of the gaussian (the phase transition region). This is the only parameter that the user can tweak in order to

obtain an accurate phase change calculation while simultaneously achieving numerical convergence. The "Enthalpy" technique views melting as a relatively simple adjustment to the standard heat equation. As a result, it enables straightforward implementation and less difficult numerical integration. In any case, it is necessary to evaluate the phase-field model's restrictions in order to select the appropriate numerical approach:

- The curvature role is not included, therefore the enthalpy model solutions can deviate significantly from the phase field ones in 2D and 3D cases especially in the presence of a constrained materials' interface;

- The $T = T_M$ level sets the solid/liquid front. This could cause numerical instability when T_M depends on other variables (e.g. the alloy fraction, see the following section);

- The studied problem has to belong to quasi-equilibrium: i.e. the temperature at the solid-liquid front must stay close to T_M. This is not the case of e.g. non-equilibrium phenomena as the explosive crystallization (see again the next section).

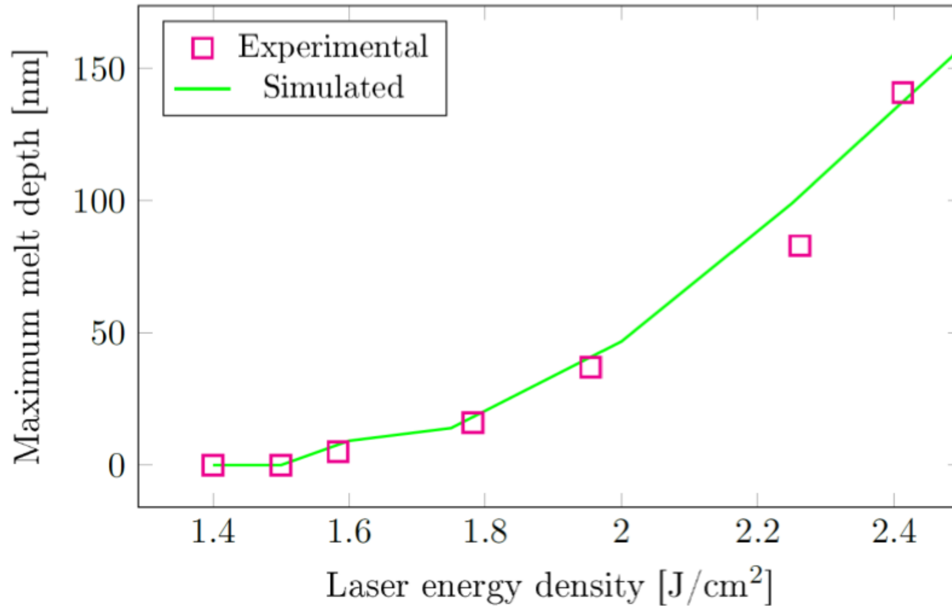

Figure 2.4: A comparison of the maximum melt depth as predicted by LIAB [37] (green line) and as observed (magenta squares). Silicon constitutes the 1D structure's core portion.

2.3.3 Simulation examples of melting processes in 1D, 2D and 3D systems

In blanket samples, the melt depth (i.e. the maximum extension of the molten film) can be determined as a function of the irradiation condition. As a result, comparisons between measured and predicted values of this quantity provide a viable method for validating simulations (model + parameter calibration). Fig. 2.4 plots the predicted melt depth in a pure Si substrate as a function of fluence for a laser process our standard pulse pulse ($\lambda = 308nm$). The agreement between simulation and experiment is excellent, revealing not just the maturity of the Si parameter calibration, but also the quality of the Si parameter calibration. As expected, phase field and ethalpy models produce identical findings in this basic scenario.

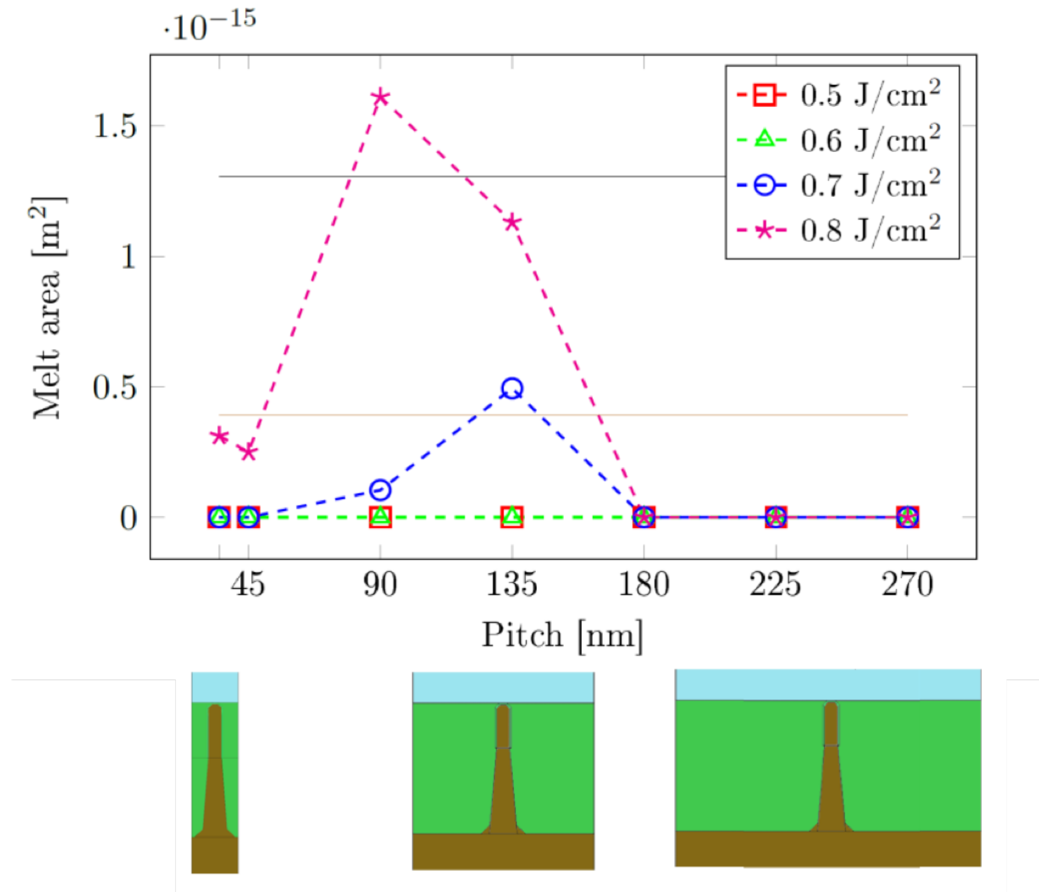

Figure 2.5: In the 45-degree polarization instance, the global maximum melting area for different laser energy was determined. Total areas of the upper and lower Fins are depicted by horizontal lines.

As expected, the complicated behavior of the laser process (namely, its reliance on geometric constraints in patterned samples) is increased in melting processes. A non-linear example of this tendency is illustrated in Fig. 2.5, which depicts the simulated total melt area for the FinFET structure discussed in the preceding section. By varying the periodicity of the FinFET array, a substantially non-linear dependence on the melt area is obtained, and the peak of these curves as a function of pitch occurs at different pitch values as the fluence changes.

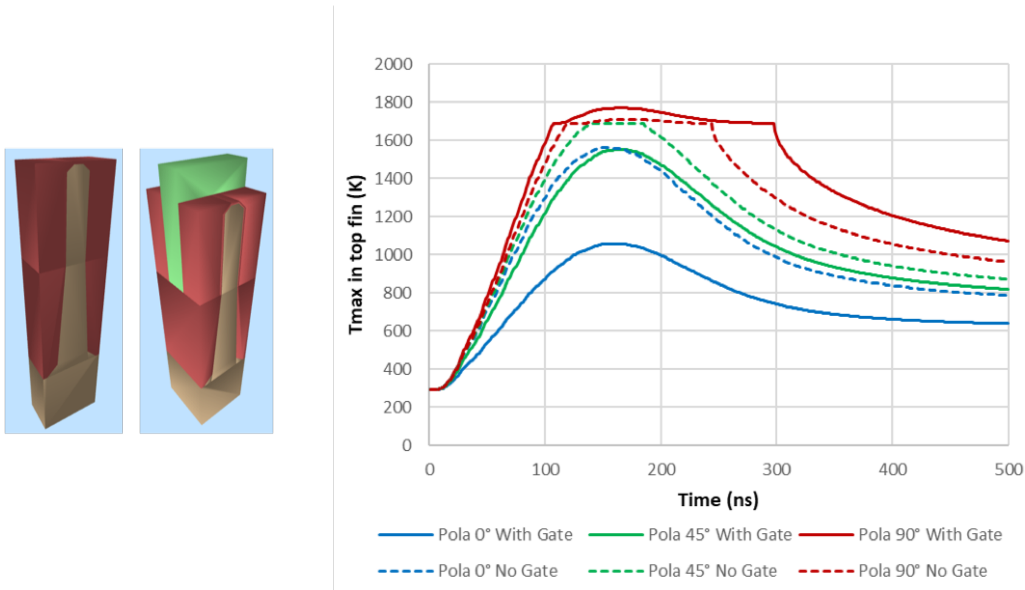

Figure 2.6: On the left there are Two- and three-dimensional models of a FinFET structure. 3D models provide the examination of a spatially constrained top gate. (b) Maximum temperature of the top Fin as a function of time during a 3D laser annealing simulation with varying polarization values and the presence/absence of a top gate. Ref. [37]) ,

Due to the intricate interplay of electromagnetic energy absorption, heating, and melting phenomena, process design with TCAD cannot be adequately addressed by simplifying the structure under consideration. For example, approximated simulations of 2D cuts, which are frequently used in the study of other thermal processes, are ineffective for the laser annealing process if the structure is intrinsically 3D (as illustrated in the left panel of Fig. 2.6). To illustrate the significance of this issue, the right panel of 2.6 compares the maximum temperature simulated in the 3D FinFET geometry (solid lines) to one alternative 2D (dashed lines) cut of the same system. Non-melting and melting processes (as indicated by the plateau of the temperature curves) are reproduced as a function of polarization in both cases with a similar qualitative trend. However, the quantitative findings are significantly different, indicating the need of

conducting the investigation in complete 3D.

2.3.4 Advanced features: Impurity and Dopants evolution

Transient melting achieved using pulsed laser processes also has the advantage of being a doping technique, as highly active (beyond the maximum solid solubility threshold) impurity profiles may be generated as a result of non-equilibrium phenomena. As a result, TCAD simulations rely heavily on the prediction of impurity evolution during a melting laser annealing process.

In contrast to the non-melting case, significant mass transfer on the nanosecond scale occurs throughout the melting stage, owing to the high diffusivity $\sim 10^{-4} cm^2/s$ (strong intermixing) of all impurities in the liquid phase, including doping impurities. As a result, the phase transition has a significant effect on the impurity chemical profiles, which remain basically constant during the extremely rapid heating.

To provide sufficiently trustworthy predictions of impurity redistribution, two major effects must be modeled: bulk diffusion and segregation behavior at the solid-liquid interface. The latter two phenomena are related to the density jump at the solid-liquid interface and are governed by the impurity coefficient of segregation in equilibrium under quasi-equilibrium conditions.

$$k_0 = C_{solid}/C_{liquid} \simeq Constant < 1 \tag{2.21}$$

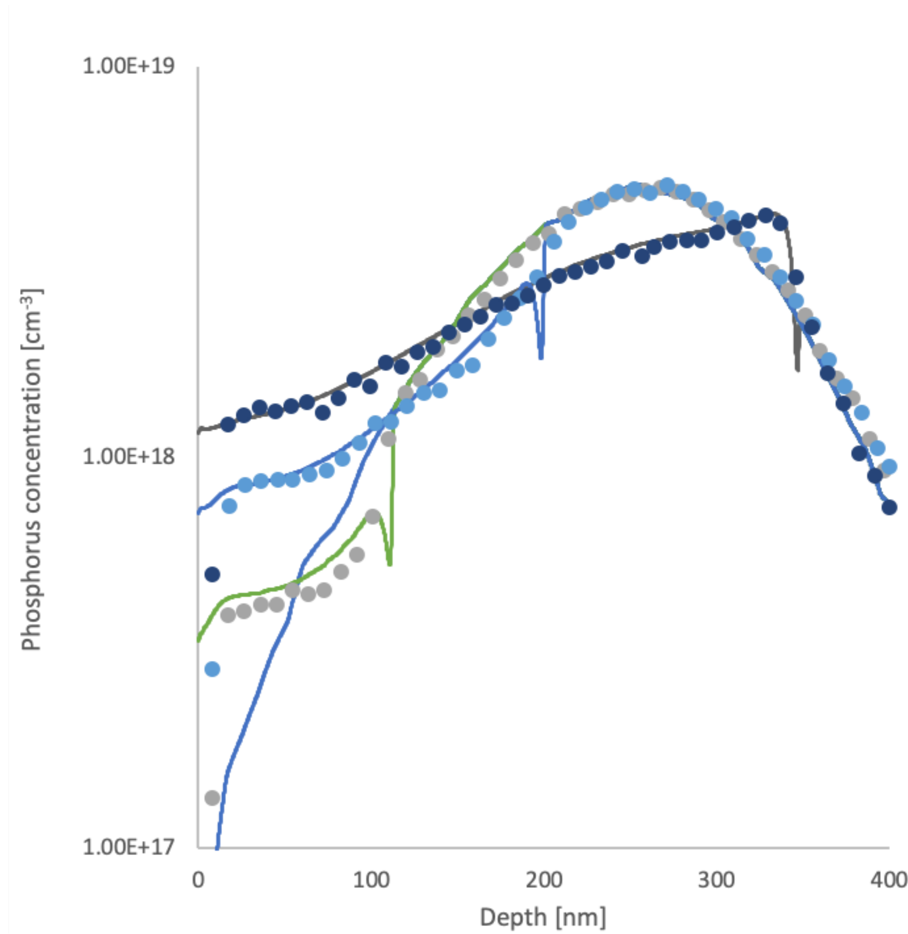

Figure 2.7: A comparison between LIAB [37] simulated continuum lines and SIMS profiles (point) of implanted P in Si (P 200 keV 10^{14} cm^{-2}, grey points) after laser annealing processes at different fluences ($\sim$ 160 ns pulse and $\lambda = 308$ nm).

Because phase field and enthalpy models accurately map the molten area (e.g., $\phi = 0$ in the phase field case and $T > TM$ in the enthalpy case), they may be used to describe diffusion and equilibrium segregation. We observe that the kinetic effect of the density jump (Eq. 2.21), particularly for small values of $k0$, has a significant effect on the final impurity profile with an accumulation peak (segregation peak) for the impurity density formed during the solidification stage in the shrinking molten region [2]. .

Indeed, modeling is hampered further by the fact that the (non-equilibrium) segregation coefficient is dependent on the local speed of the liquid-solid front and approaches to unity at very high speeds [44]. This behavior, referred to as solute trapping, is extremely beneficial for doping applications, but it complicates the numerical approach further by requiring the inclusion of the front speed in the dopant diffusion equation, and it also makes the use of enthalpy models less practical. Regardless, a global formulation of the phase and density fields using a generalized phase field technique [1, 2] enables an accurate formulation of the solute trapping effect within the coupled phase field equations for the phase and density variables. There is no requirement for a speed front evaluation, and the model is acceptable for integration in any dimension.

The integration of dopant evolution equations into laser annealing TCAD models demonstrates the ability to forecast dopant profiles in both blanket and structured samples. When these methodologies are used, examples of agreement between experimental and simulated profiles are shown in Fig. 2.7 for a blanket scenario (initial implanted P 1D profile) and Fig. 2.8 for a patterned case (initial implanted As 2D profile).

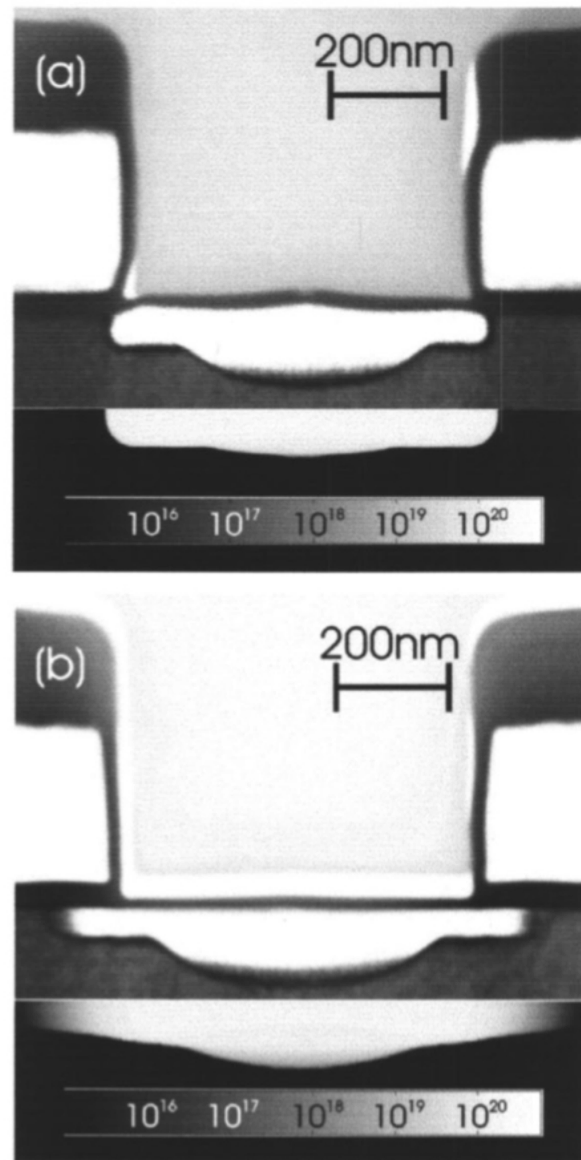

Figure 2.8: A comparison between the simulated dopant distribution and a transmission electron microscopy image of a dopant profile that had been delineated using the selective etching procedure. Annealing was performed on the specimen utilizing a one pulse at fluence 0.887 J/cm^2 (a) and 1 J/cm^2 (b) ($\sim$ 20 ns pulse and $\lambda = 308$ nm). Ref. [3].

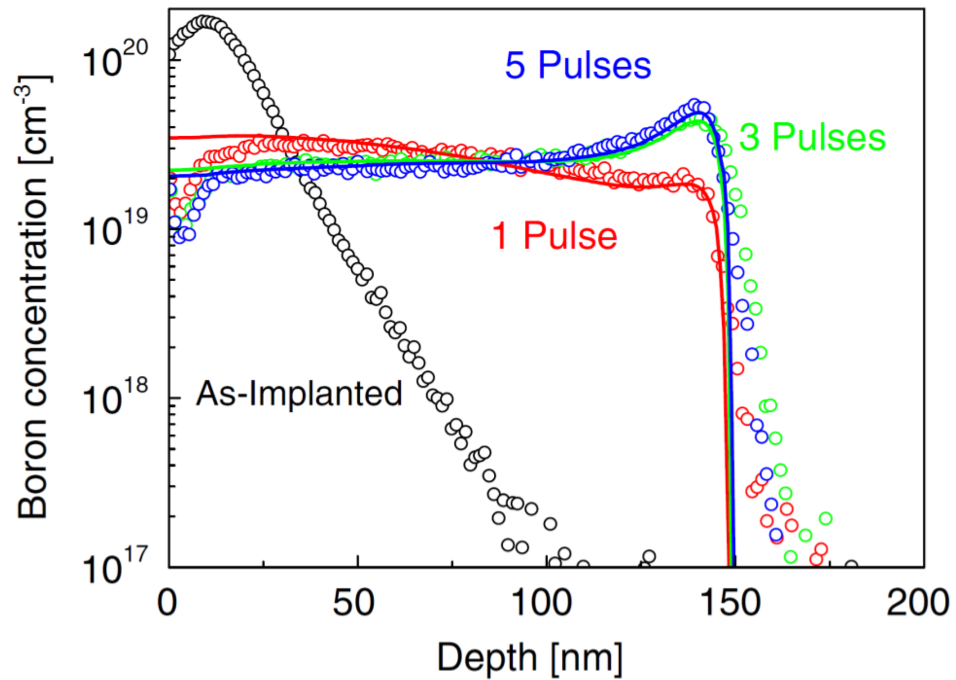

Figure 2.9: Dopant redistribution in the melting phase in implanted Si following exposure to multiple pulses of laser irradiation, as seen experimentally (circles) and simulatedly (lines). (2.6 J/cm^2). Ref. [4].

Impurity evolution during melting pulsed LA processes can be simulated using calibrated diffusion equations (Fick-law) and segregation models [44, 2]. However, especially for ultra shallow profiles, the diffuse profiles often indicate anomalies that necessitate model adjustment. In shallow profiles of implanted Si-X and Ge-X (X = B, P, and As) alloys after LA, anomalous peaks (see e.g. Fig. 2.9 [45, 46, 5, 7].

The anomalous redistribution of impurities is treated as an indirect impact of their diffusion mechanism in the liquid semiconductor in Ref [4]. The essential premise is that the solute atoms dispersed in the liquid semiconductor have two states with suitable bonding arrangement [47, 48, 49]. These states, with wildly varying mobilities, are in a dynamic equilibrium governed by local temperature. In emphl-Si, the balance of these two components of solute density leads to worldwide diffusion of impurities that defies Fick's law (Ge). The diffusion model is expressed by the following equations:

$$\frac{\partial c}{\partial t} = \frac{\partial c^{HD}}{\partial t} + \frac{\partial c^{LD}}{\partial t} \tag{2.22}$$

$$\frac{\partial c^{HD}}{\partial t} = \nabla \left[D^{HD} \nabla c^{HD} \right] + k^{\tau} \left(c^{LD} - \bar{R} \cdot c^{HD} \right) \tag{2.23}$$

$$\frac{\partial c^{LD}}{\partial t} = \nabla \left[D^{LD} \nabla c^{LD} \right] - k^{\tau} \left(c^{LD} - \bar{R} \cdot c^{HD} \right) \tag{2.24}$$

where D^{HD} and D^{LD} are the impurity diffusivities in the liquid phase. The concentrations are c^{HD} and c^{LD}. It is the ratio of low to high diffusivity states at constant T. Please note that for non-equilibrium processes, the liquid phase temperature is not limited to $> Tm$. In under-cooled locations, poorer diffusivity impurity atoms dominate migration [49] and impurity kinetics have $\bar{R}(T) < 1$ for T over the melting point and atoms in the higher diffusivity state. This is called standard diffusion in the solid phase, and it is described in [50]. k^{τ} controls the transition between the two states and is connected to the bonding order fluctuations in *l*-Si and *l*-Ge and I ts value is fixed [4, 5].

In regions with $T < Tm$, lower diffusivity dopant atoms are preferred, while greater diffusivity dopant atoms describe impurity kinetics in stable liquid regions. The two-state model predicts temperature-dependent

diffusivity in the liquid phase. However, the anomalous redistribution is a secondary consequence, linked to the local imbalance between states with high and low mobility.

Comparison of the model's predicted diffusion profiles to SIMS observed Boron (B) density profiles in implanted Si (B 3 keV energy, 5×10)

The dose (black circles in the figures) after single pulse LA procedures at varying energy densities is presented in Fig 2.9. The diffusion model's anticipated post-LA B profiles (solid lines in Fig.reffig:non-fick) match the experimental ones.

An extended melting front across the defective implanted regions promotes complete healing of the damage after regrowth, a typically epitaxial regrowth mode, and strong activation of the dopant profiles. Some technical applications necessitate partial melting of implanted layers (pockets). Destruction evolution and activation efficiency in locations not touched by the melting front are therefore interesting.

Today's TCAD models for conventional annealing procedures use continuum and Monte-Carlo modeling of implanted defect evolution in solid sections during LA. The rate parameters are depending on the local (space dependent) temperature field [11]. Without a doubt, the defect and defect-impurity aggregates evolve in these LA models, as they do in traditional annealing processes, via the mobile species density field [51]. In the end, they don't explain how fast extended defects arise in experiments and in molecular dynamics simulations.

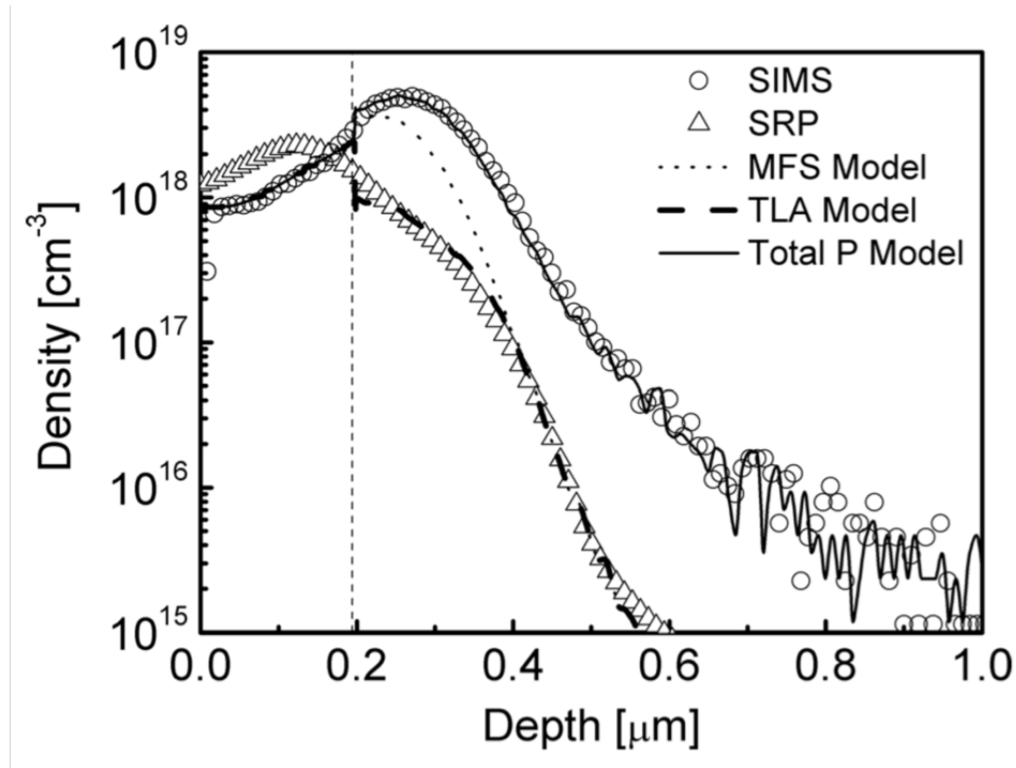

Figure 2.10: Experimental results from SRP measurements (open triangles) and the simulated (thick dashes) P active profile as a function of depth after a single pulse laser process (3.0 J/cm^2) of an implanted Si substrate (P 200 keV energy, 10^{14} cm^{-2} dose). Thin dashes: the model's simulation of the P active profile. Solid line: the total redistribution of P that was simulated. The open circles are for the SIMS analysis, and the vertical line is for the experimental melt depth. Ref. [52].

Despite this flaw, continuum modelling of systems with defects-impurities accurately reproduces dopant activation kinetics during pulsed LA procedures. Figure 2.10 compares the simulated active profile of implanted P in Si after partial melting LA to the active profile measured by Spreading Resistance Probe (SRP).

2.4 LIAB workflow, basics and evolution

It is our intention to use this brief section to provide a quick overview of the many computational processes that we employ in LIAB, which have already been thoroughly detailed in the preceding sections.

The first point to address is how to use the application. LIAB is mostly utilized through its graphical user interface (GUI), which takes the user through the CAD design process and the setup of all of the parameters. Because everything is handled by xml files, an experienced developer can set up a variety of customs scenarios (such as the ones we'll see in chapter 4), which are useful for more complicated configurations. The first stage is the definition of geometry.

When we design our 1d, 2d, or 3d models using the CAD modeler built into the LIAB GUI or by writing an ex-novo xml input file. In the LIAB GUI, we can define our simulation space by assigning a name and dimensions to each region. We can also specify what kind of material will fill that space - for example, we can choose between Si, Ge, or GaAs. We can even specify impurities that will be added to the material, which can affect its properties. Finally, we can specify whether or not the region will be melted in the simulation. All of these choices are important in defining the geometry of our simulations. By carefully choosing the dimensions and materials of each region, we can control how the light interacts with our devices and create structures with desired properties. In finite element analysis, the quality of the results is directly related to the quality of the mesh. A good mesh will have elements of uniform size and shape, with minimal gaps or overlaps. In contrast, a bad mesh will have inaccurately sized or shaped elements, leading to errors in the final results. The meshing step is therefore crucial in ensuring the accuracy of the final analysis. GMSH is a powerful open source mesher that is capable of creating high-quality meshes. In addition, GMSH is highly customizable, allowing users to fine-tune the mesh to their specific needs. As a result, GMSH is the perfect tool for handling the meshing step in our finite element analysis workflow.

While our main solver is the most sophisticated and computationally intensive stage, it is divided into many phases to make the process more manageable. The first stage is the electromagnetic calculation, which es-

tablishes the strength and direction of the magnetic field. Once this is known, a heat source can be computed, and then the heat diffusion stage takes over to complete the process. This division of labor ensures that each stage is performed with the utmost accuracy, resulting in a more reliable overall solution.

We will now proceed to the final stage of phase computation, where we will employ the phase field or enthalpy formalism to compute the phase change. This will be a more complicated calculation that includes alloy redistribution, dopant diffusion, and other such things. However, with this method, we will be able to obtain a more accurate result for the phase of our material. Additionally, this will allow us to study the effects of different dopants on the phase of our material. Finally, this method will also allow us to investigate the role of interfaces in phase transformations.

Prior to the beginning of this work, LIAB relied solely on the enthalpy model as the source computation method. As previously stated, this is a relatively fast but inaccurate method, which is useful for fast solutions involving simple geometries and materials that do not contain alloys or doped materials. The Phase Field model is a newer approach that overcomes these limitations, it is more accurate because it takes into account material transport. The implementation of a stable algorithm for the phase field accounted for a significant portion of the code's development.

As seen before the phase-field model is typically developed in such a way that the right interfacial dynamics can be retrieved even in the case of minuscule interface width (the so-called sharp interface limit). This renders the problem quite a stiff one, i.e. for which certain numerical methods for solving the equation are numerically unstable. Multiple checks on the numerical error between two stages are performed by the algorithm; if the error exceeds a user-defined threshold, the step is repeated with a smaller timestep.

The code has been parallelized using the Message Passing Interface (MPI) standard, in order to run on high-performance computing (HPC) clusters. The use of MPI allows for a great deal of flexibility, since the code can be easily used on systems with a variety of number of processors. This is due to the fact that the domain decomposition and load balancing are performed automatically by the MPI library. FEniCS, a

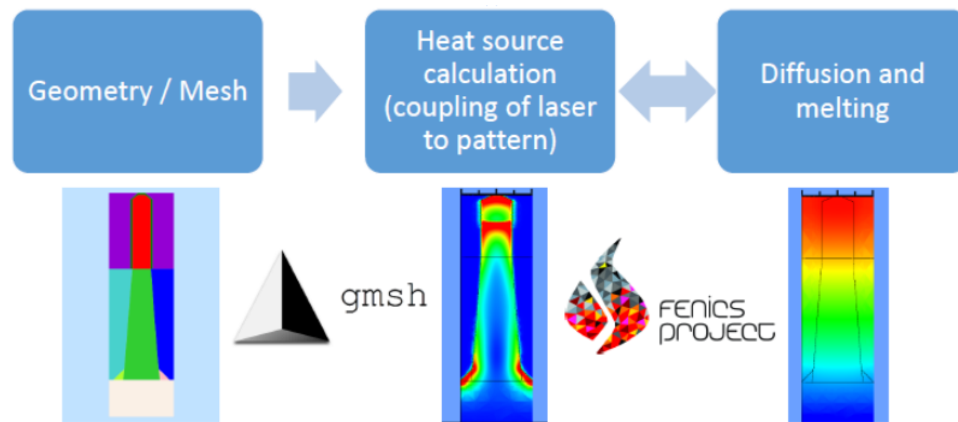

Figure 2.11: Schematic of the main stages of a LIAB simulation

prominent open-source computing platform for solving partial differential equations, is used to manage all solvers that include the use of differential equations.

We discussed how the code handles the laser-matter interaction, including optical excitations of electrons in solids caused by photons with energies of *sim*eV, as well as the inner interaction that leads to energy transfer from the electron system to the phonon bath (also known as thermalization). Then we spoke about simulating the LA mechanisms that cause crystal-liquid-crystal phase transitions. The main focus of this discussion was on the computational challenges of non-equilibrium impurity kinetics and activation. Finally, we'll discuss how the code really works, as well as the differences between the code before and after I finished my PhD.

Chapter 3

Simulations with complex materials, SiGe case study

In this chapter, we address one of the major issues with our continuous simulations: the lack of an atomistic description of the material alloys, particularly SiGe, which required a strong calibration of its parameters based on experimental and simulation data in order to work in our code. The calibration of the optical parameters is explained in the first section, and the first evaluation stage compares our Electromagnetic (EM) results with those derived from Dr Litho software developed at Fraunhofer institute. Dr Litho is a simulation environment for photolithography, and its EM results are fairly accurate. Following the validation section, we offer a Study of SiGe patterned structures to demonstrate the robustness of our calibration.
The main driving force of the CMOS industry is scaling rules, which require doubling the transistor aerial density per technology generation. Traditionally, scaling transistor dimensions by a factor of 0.7 has resulted in continuous performance improvement or a reduction in circuit delay. However, as transistors are scaled down, the rate of performance boost slows because parasitic device components begin to impact overall device performance.

To address this problem, strained Si has been used in the industry since the 90 nm technology node[53]. Tensile stress liners have been used to enable channel strain in n-MOSFETs and embedded silicon-germanium

(SiGe) source/drain (S/D) in p-MOSFETs. The embedded SiGe in the S/D regions applies compressive strain to the Si channel and has been tuned at each technological generation by the amount of Ge, boron doping, recess volume, and profile to assure the maximal strain advantage for p-MOSFETs manufactured on bulk or SOI substrates [54, 55].On the other hand, it has been demonstrated that as the contacting gate pitch size is reduced, the positive impact of these known stressors is considerably reduced[56]. This problem is exacerbated when nonplanar topologies such as trigates, FinFETs, or gate-all-around nanowires are manufactured on SOI substrates. One possibility is to replace the Si with a material with great mobility, such as SiGe or Ge. Utilization of globally strained materials, such as strained Si for nFETs and strained SiGe for pFETs, appears to be a near-term technological solution, whereas replacing the channel with other candidates, such as III-V or pure Ge, appears to be a long-term solution for advanced high-performance technologies.

The complex simulation of the melting processes of Si1 $-$ X GeX alloy is mostly due to the material characteristics' dependency on the local alloy fraction X, which evolves as the impurity profile during transient melting governed by a diffusion/segregation equation. This dependence is especially important for numerical simulations of melting temperatures $TM(X)$ since it has a substantial impact on the dynamics of the solid/liquid interface and increases the non-linearity of the diffusion/segregation model. Finally, the problems of the simulation technique are related to achieving a proper calibration of the thermal and optical parameters, which, in addition to temperature dependency, utilizes a dependence on X.

As previously stated, the interaction between the segregation behavior of the X field and the X dependent melting point renders the enthalpy approach inapplicable, because the ultra fast change of X at the solid/liquid interface artificially and instantly displaces the position of the interface itself (which is located at the $T = TM(X)$ level in the enthalpy model).

The additional phase equation governs the interface in the phase field model, and the $TM(X)$ variable influences the interface speed (U term in refeq:phase), not its position, allowing for a reasonable, albeit challenging, numerical implementation. A reliable TCAD model of the SiGe LA process has just been obtained [57]. The phase field type technique and

relative calibration have been validated both in blanket samples (see next section for further details) and in sophisticated device designs (for example, see Fig. 3.14 for an example of a TCAD simulation in a SiGe-based nanodevice structure) while also taking dopant atoms into account. Despite the highly non-linear nature of the alloy's continuum model, the numerical solutions are shown to be adequately stable, at least in the 2D case, after careful tuning of the FEM technique.

3.1 Calibration of the optical constants in SiGe

SiGe is a nearly perfect binary alloy system in which Si and Ge are entirely miscible across the whole composition range. Because of this, the linear interpolation of the physical properties of Si and Ge (using the Ge alloy fraction variable X) is a reasonable starting point for the calibration of this material (5). However, there are several crucial uncertainties. A more precise determination of the optical parameters' dependency on X in each phase is required. Furthermore, direct measurements are insufficient to determine the dependency of the parameters in the disordered phases (liquid and amorphous) on X: The conventional technique is to apply the same relationships as for the crystalline phase. The optical parameter P (e.g., the real or imaginary component of the dielectric function) is denoted as:

$$P_{SiGe}(T,X) = P_{Ge}(T) f_P^n(X,T) + P_{Si}(T)[1 - f_P^n(X,T)] \tag{3.1}$$

where $f_P^n(X,T)$ is monotonically growing polynomial function of degree n satisfying the obvious relationships $f_P^n(0,T) = 0$, $f_P^n(1,T) = 1$ while $P_{Ge}(T)$ and $P_{Si}(T)$ are the Ge and Si parameters present in our database. Therefore, only $f_P^n(X,T)$ has an unknown form and calibration. If we consider a second order polynomial function $f_P^2(X,T)$, we have:

$$f_P^2(X,T) = a(T)X^2 + [1 - a(T)]X \tag{3.2}$$

We note here that such a function fulfils the $f_P^2(0,T) = 0$, $f_P^2(1,T) = 1$ constraints that reflect the limiting conditions where the content of Ge is either 0% (pure Silicon) or 100% (pure Germanium). In order to consider the temperature dependence of the optical constants, function $a(T)$ has

been further calibrated as a second-order unrestricted polynomial function:

$$a(T) = bT^2 + cT + d \tag{3.3}$$

where b, c and d represent the calibrated parameters from the experimental measurements. A second level of calibration is necessary when SiGe samples are doped. In this case, a function $E_{SiGe}(T, X, C)$ can be introduced, where C represents the dopant concentration in the samples:

$$E_{SiGe}(T, X, C) = P_{SiGe}(T, X)g(C, T) \tag{3.4}$$

where $g(C, T) = 1 - m(T)C/C0$. Here, $m(T) = b'T^2 + c'T + d'$ is an unrestricted second-order polynomial function of temperature with parameters b', c' and d', while C0 is a constant that allows for $g(C, T) \approx 1$ in the case of very low-doping (hence, for very low doping, $E_{SiGe}(T, X, C) \approx P_{SiGe}(T, X)$). The full parametrization and optical constant calibration for wavelength $\lambda = 308$ nm (corresponding to the used laser line during laser annealing experiments) is reported in Table 3.1.

Parameter	Description	Values related to Real Permittivity	Values related to Imaginary Permittivity
$P_{Ge}(T)$	Permittivity function for Ge	3.91230E-06*T^2-1.35530E-02*T+8.94077	-5.22533E-06*T^2+1.59269E-02*T+23.5712
$P_{Si}(T)$	Permittivity function for Si	-9.025E-07*T^2-6.55813E-03*T+13.8925	9.652E-03*T+35.0688
b	Parameter for function $a(T)$	2.69960559E-06	6.16719594E-07
c	Parameter for function $a(T)$	-8.93283612E-03	-3.76779637E-03
d	Parameter for function $a(T)$	2.7473922E+00	7.240882338E-01
b′	Parameter for function $m(T)$	-3.04319581E-08	-1.55547589E-09
c′	Parameter for function $m(T)$	8.79752533E-05	5.51655818E-07
d′	Parameter for function $m(T)$	-4.73111366E-03	4.13092579E-03
C_0	Constant for function $g(C,T)$	1.00E+19	1.00E+19

Table 3.1: Calibrated parameters and base functions for the real and imaginary permittivity of SiGe alloys which allow one to describe these permittivities as a function of temperature, alloy fraction and boron doping concentration. The calibration has been performed considering optical data with a wavelength of 308 nm. The unit of temperature in P_{Ge} and P_{Si} is Kelvin whereas the unit of C_0 is cm^{-3}.

Figure 3.1 shows the calculated reflectivity for undoped (a) and boron-doped (b) samples, based on the real and imaginary dielectric functions of our theoretical scheme. In Figure 3.1 a, we note that calibration for undoped samples took place for different Ge contents, also including the cases of pure silicon and pure germanium at room temperature (as limit cases). The calibration in Figure 3.1 b (regarding boron-doped samples) was instead based on a single Ge content (30%) and different dopant concentrations.

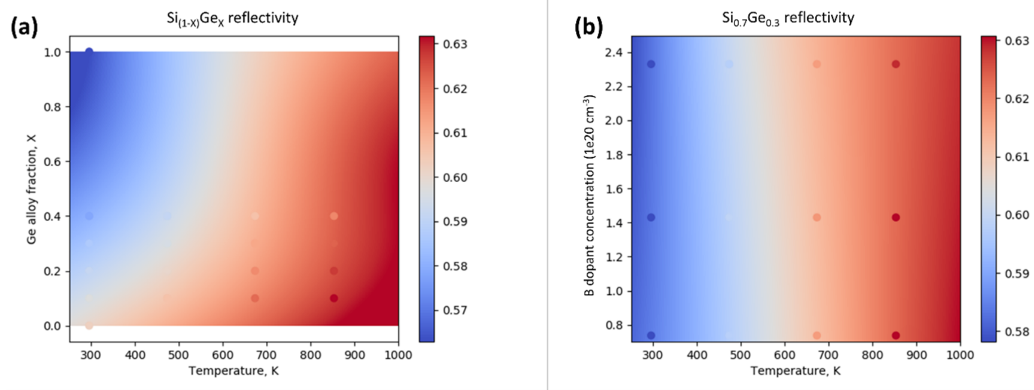

Figure 3.1: : (a) The reflectivity of samples of undoped SiGe as a function of the amount of Ge in the alloy and the temperature. (b) The reflectivity of samples of B-doped Si0.7Ge0.3 as a function of the amount of dopant and the temperature. The value of the reflectivity is shown on the color scale. The experimental values are shown by colored dots. For both experimental and theoretical results, a photon wavelength of 308 nm was taken into account.

Finally, to make uniform the calibration scheme beyond the dielectric permittivity, we have defined all other SiGe parameters of interest for LA simulations as a linear interpolation of the respective values for pure silicon and germanium, on the basis of their percentage within the SiGe alloy.

We present now two different case scenarios where the simulated data comes directly from LIAB while the SIMS experimental data comes from two different laboratories. In Fig. 3.2, simulated and experimental alloy

fraction profiles and total melt depth for an irradiated system constituted of 30 nm thick layer epitaxially grown SiGe on a Si substrate are compared. The segregation effects are significant and appropriately modelled (see Fig. 3.2 a)) both for the cases where only the SiGe melts and for the case at 2.23 J/cm^2 fluence when the molten layer expands in the Si substrate.

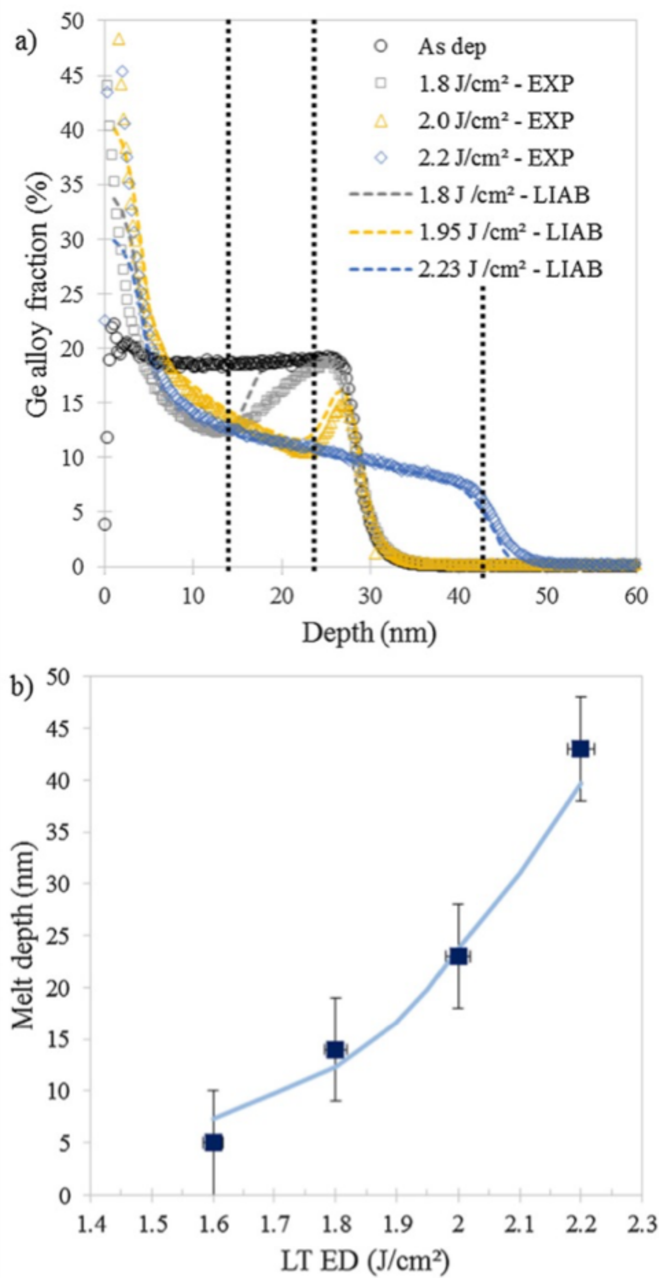

Figure 3.2: Simulated (dashed lines) Si SIMS depth profiles for $Si_{0.8}Ge_{0.2}$ 30 nm thick layer case superposed to experimental SIMS after laser annealing for fluences = 1.8, 2.0 and 2.2 J/cm^2. (b) Melting depth as a function of laser fluence extracted from Si SIMS profiles (symbols) and simulated after calibration of the Si(1-X)GeX optical properties (solid line). Ref. [57]

In partnership with CEA, an early evaluation of the proposed calibrated SiGe system was undertaken. These simulations aimed to replicate analogous experimental processes for low-doped blanket $Si0.7Ge0.3$ samples treated with CEA-LETI's pulsed excimer laser annealing system. The laser line had a 308 nm wavelength and a pulse duration of 160 ns, and it irradiated 15x15 mm^2 regions. It is worth noting that the LA code may dynamically import pre-annealing profiles for Si, Ge, and the dopant, tracking their time evolution during the annealing process. Simulations and experiments both focus on a single pulse annealing process. For three different laser fluences (1.6 J/cm^2, 1.95 J/cm^2, and 2.2J/cm^2), we fixed the total time duration of the simulation at 400 ns: no substantial evolution of the alloy fraction and dopant field occurs after this time step. This energy range is useful for a wide range of regimes and melting depths, as we can see. Figure 3.3 shows comparative results for the concentration of Ge throughout the sample depth. We see an overall good agreement between the simulated and actual profiles, especially at lower laser fluences, where a partial-melt zone close to the sample surface can be observed. The melt region grows as the laser fluence increases, and a full melt regime can be simulated with a fluence of 2.2 J/cm^2.

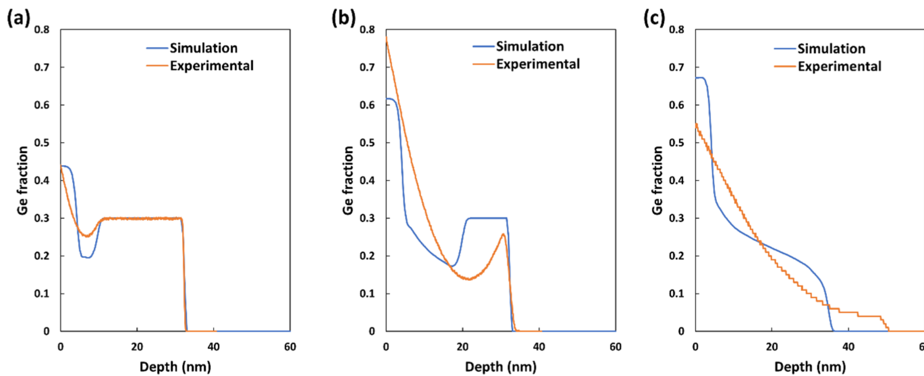

Figure 3.3: : Simulation of laser annealing processes for a $Si_{0.7}Ge_{0.3}$ sample (blue lines) and comparison with experimental SIMS profiles (orange lines), taking into account three different laser fluences: (a) 1.6 J/cm^2, 1.95 J/cm^2 and 2.2J/cm^2 The first Ge profile had a constant value of 0.3 over the entire depth of the SiGe sample, which was (≈32nm).

3.2 Benchmark of heat source calculations in patterned structures

The proper description of heating in laser annealing models represents one of the key issues for the reliable simulation of actual processes. In the custom tools owned by the CNR and CEA,that, at the core are the em mmodel used in LIAB, heating is modelled as the time harmonic solution of Maxwell's equations, where the laser heat source $S(r,t)$ is described as:

$$S(r,t) = \epsilon_2/2\rho|E_{(t-h)}|^2 \tag{3.5}$$

The imaginary part of the complex dielectric function of the heated material is denoted by $\epsilon 2$, the time harmonic electric field is denoted by $E(t-h)$, and the square of the time harmonic electric field denotes the strength of the electromagnetic field. The findings of heating source dispersion in complex SiGe structures generated from these bespoke tools were compared with EMW calculations performed using the Dr. LiTHO software citeFhner2007[58] to demonstrate the accuracy of this approach.The latter method, which is based on the finite-difference time-domain (FDTD) and the waveguide methods, provides precise estimates of the dissipation of electromagnetic energy in these complicated geometries. Within the irradiated materials, two quantities have been measured: a spatial distribution of electromagnetic wave intensity and an absorption of electromagnetic waves (which is related to a material's heat generation density) in the material itself.

Figure 3.4 illustrates a simplified geometry of the periodic $Si0.9Ge0.1$ FinFET structure (with periodic boundary conditions at the left and right borders) on a silicon substrate. According to the results for both the intensity and absorption of electromagnetic waves, the quasi-adiabatic technique used by the custom laser annealing solvers can adequately model the heating process. It is critical to check for electromagnetic congruency at temperatures higher than room temperature since the laser process itself should cause heating up to melting temperatures, which is required for the activation of dopants. This is a challenging problem to solve. The comparison of findings between the two approaches for a $Si0.8Ge0.2$ FinFET structure at three different constant temperatures is depicted in Fig-

ure 3.5 (300 K, 873 K, 1273 K). It is also obvious in this case that there is agreement between the two theoretical schemes, with the electromagnetic intensity exhibiting two maxima at the lateral edges of the FinFET at 300 K, which tend to merge as the temperature rises. At long last, we looked at the compatibility of the two techniques for more complex geometries, such as an over-etched FinFET structure (Figure 3.6) and a SiGe trench with an oxide mask on top (Figure 3.7). We discover that, given the trench structure, a distinct variation in EMW intensity can be observed in the oxide and SiGe portions of the layer, as previously stated. Although the results were satisfactory even for these complicated geometry structures, the quasi-adiabatic method to heating in laser annealing simulations was found to be even more valid in this case. A decision was made in light of the aforementioned findings to continue the simulation campaign using the quasi-adiabatic model of the custom laser annealing equipment.

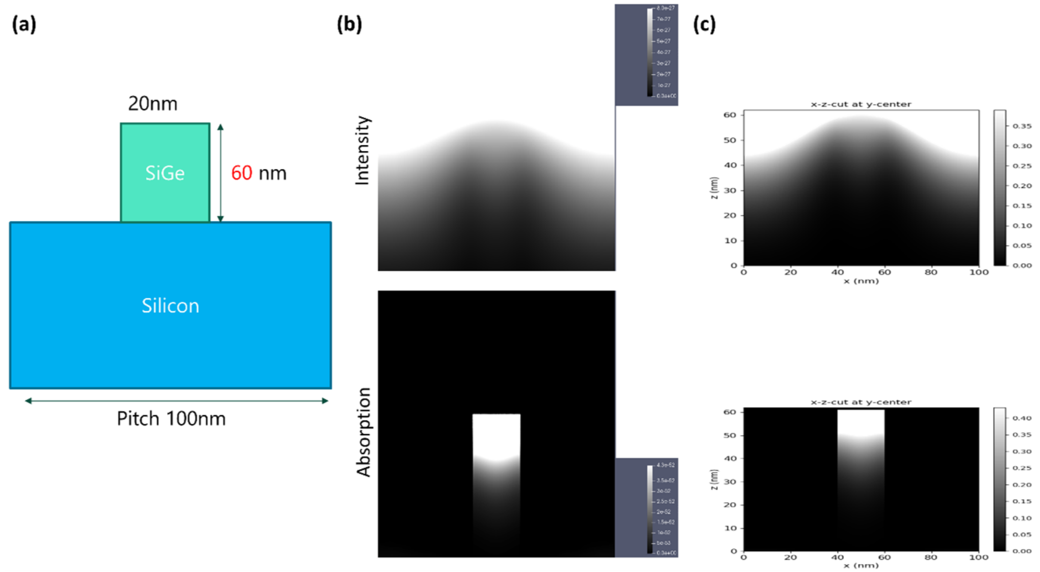

Figure 3.4: (a) A FinFET structure made of $Si0.9Ge0.1$ with a width of 20 nm, a height of 60 nm, on a 100 nm pitched silicon substrate. (b) Calculations of the intensity of the electromagnetic field's spatial distribution (upper) and how it is absorbed by the $Si0.9Ge0.1$ material (lower) at 300 K, based on custom research tools at the CNR that use quasi-adiabatic methods. (c) Dr. Litho software calculations as in (b), based on how much power is lost. The different number scales in the two programs are caused by the way they are normalized.

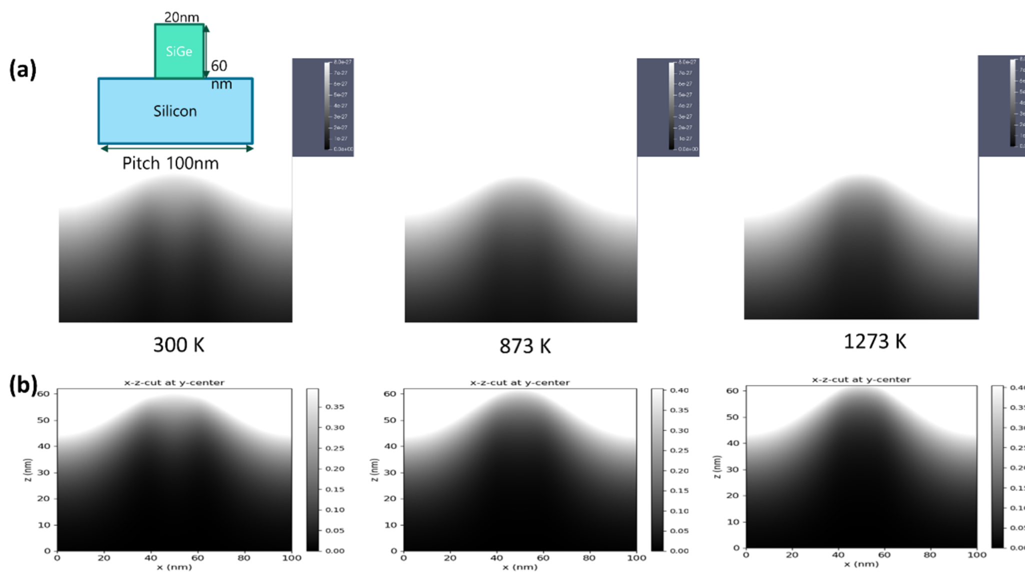

Figure 3.5: Comparison between the spatial distribution of electromagnetic wave intensity for different temperatures based on custom research tools at the CNR (a) and the Dr. Litho software (b). The target structure is a FinFET based on $Si_{0.8}Ge_{0.2}$ with a width of 20 nm and a height of 60 nm on a silicon substrate with a pitch of 100 nm.

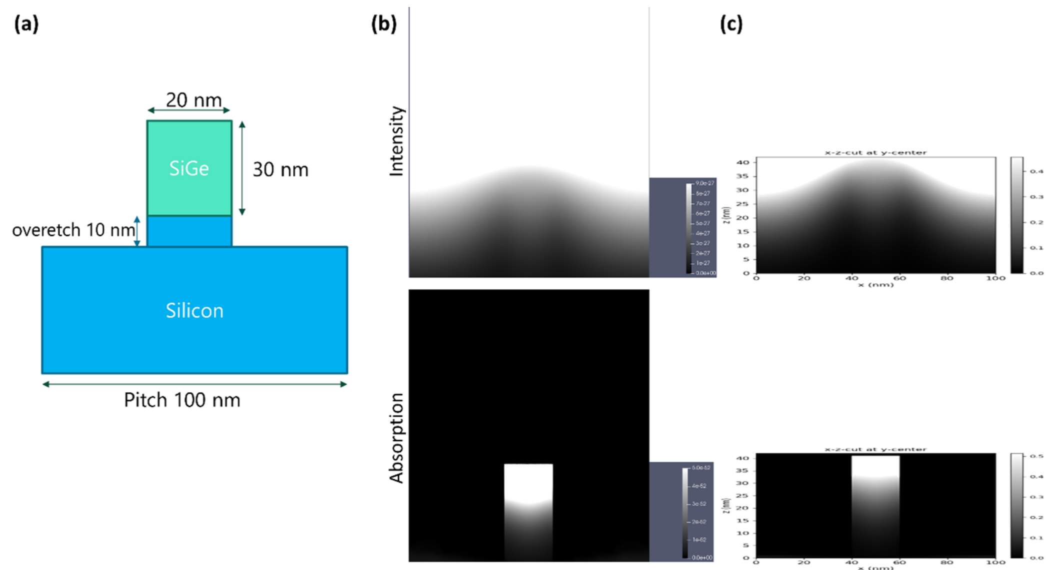

Figure 3.6: (a) Overetched FinFET structure based on Si0.9Ge0.1 with a width of 20 nm and a height of 30 nm on a 10-nm-high silicon etching, on top of a silicon substrate with a pitch of 100 nm. (b) Calculations of the spatial distribution of the intensity of the electromagnetic field (upper) and its absorption by the $Si_{0.9}Ge_{0.1}$-Si material (lower) at 300 K, based on custom research tools at the CNR using quasi-adiabatic methods. (c) Similar calculations as in (b) based on power dissipation, using the Dr. Litho software.

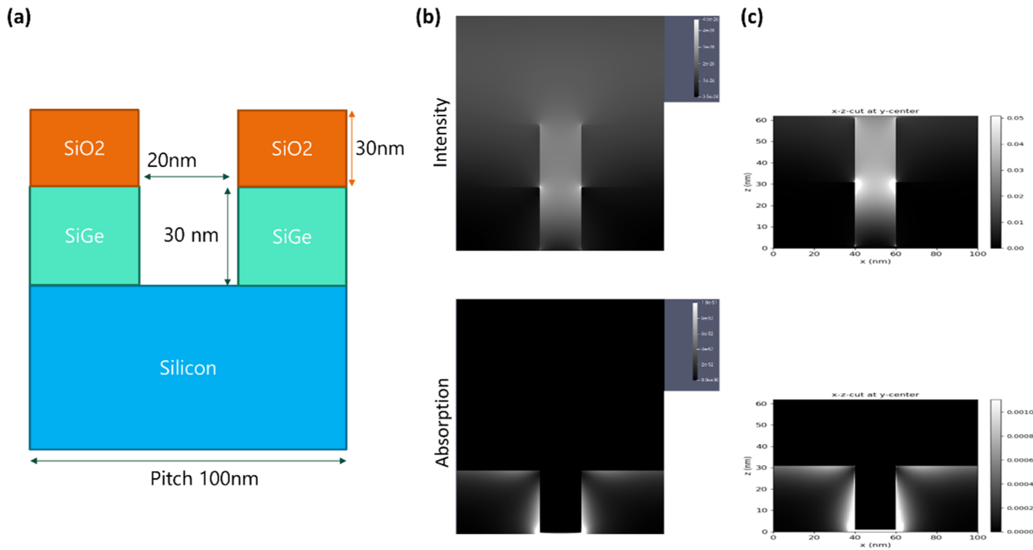

Figure 3.7: (a) Si0.9Ge0.1 trench structure having an oxide mask with a width of 20 nm and a height of 30 nm on a silicon substrate with a pitch of 100 nm. (b) Calculations of the spatial distribution of the intensity of the electromagnetic field (upper) and its absorption by the SiO2 and $Si_{0.9}Ge_{0.1}$ materials (lower) at 300 K, based on custom research tools at the CNR using quasi-adiabatic methods. (c) Similar calculations as in (b) based on power dissipation, using the Dr. Litho software.

3.3 Study of SiGe patterned structures and complex devices

Using a simulated analysis of the laser annealing process in two-dimensional patterns, it was possible to identify laser process windows that may be used in future experiments. These investigations should be devoted to the investigation of patterning effects in material modification and dopant redistribution induced by irradiation using various characterisation techniques, as well as the development of new patterns. In this study, we use epitaxial SiGe/Si structures as reference substrates, i.e., 30nm strained substrates with varying degrees of Ge alloy percentage and B dopants,

as well as strained SiGe/Si epitaxial structures. Additional lithographic methods may be used to create periodic SiO2 trenches with varying pitches, heights, and widths; as a result, we simulated the LA using the same calibration set described in the preceding section as a function of the fluence, polarization, and structural geometry. Figure 3.8 depicts a schematic of the structure with the geometry modifications taken into consideration during the simulation study.

In this section, we discuss the generic behavior of the simulated evolutions, which exhibit qualitatively similar characteristics while exhibiting quantitatively different characteristics in dependence on the laser parameters, geometry, alloy fraction, and doping level, as illustrated by a specific case. Among the structure's distinguishing characteristics is the time-dependent variation of its temperature field, which reaches its maximum at the core of the structure. All of the investigated examples exhibit this modulation as a result of the irradiation, with the center-border differences depending on the laser strength, polarization, and geometry, among other factors. Besides transverse electric (TE), transverse magnetic (TM), and mixed polarization (Θ=45°), we have also studied transverse magnetic (TM). However, when the polarization is changed, the solutions are relatively comparable, indicating that this is not a key process parameter for the chosen geometry, as we would expect given the peculiar and highly symmetric nature of the patterning (SiO2 material). It is the persistence of the antireflective effect in the patterned systems that is responsible for the temperature modulation. As a result, it is a direct consequence of the modification of absorbed power. For the 308nm laser irradiation, we see that the effective $\lambda/4$ thickness is close to 50nm, resulting in a maximal reflectivity decrease of more than 45% for a blanket SiO2+SiGe stack for the SiGe materials under consideration. The temperature modulation has an effect on how the molten phase nucleates in the SiGe at the center of the SiGe/SiO2 interface nucleates, which results in a two-dimensional distribution of the alloy fraction and the dopant during the early stages of the transient melting phenomenon (as shown in Figure 3.9a). There , the Ge fraction is depicted in a snapshot of the simulated evolution 5ns after the nucleation event for a LA process with fluence of 1.1 J/cm^2 and TE polarization in a structur ewith 100nm pitch, 80nm and 30nm oxide thickness and width, and a dopant level of 7.4×10^{19}. In this

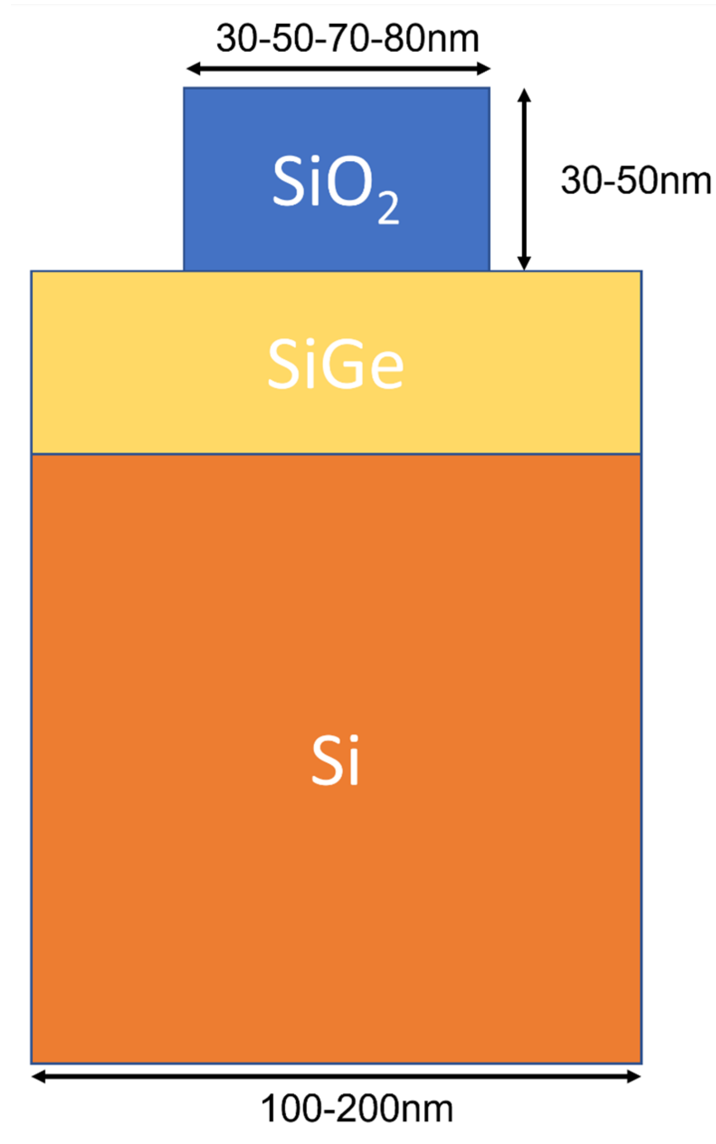

Figure 3.8: The diameters of the pitches, oxide heights, and widths for the case studies are shown in the schematic of the simulated geometries.

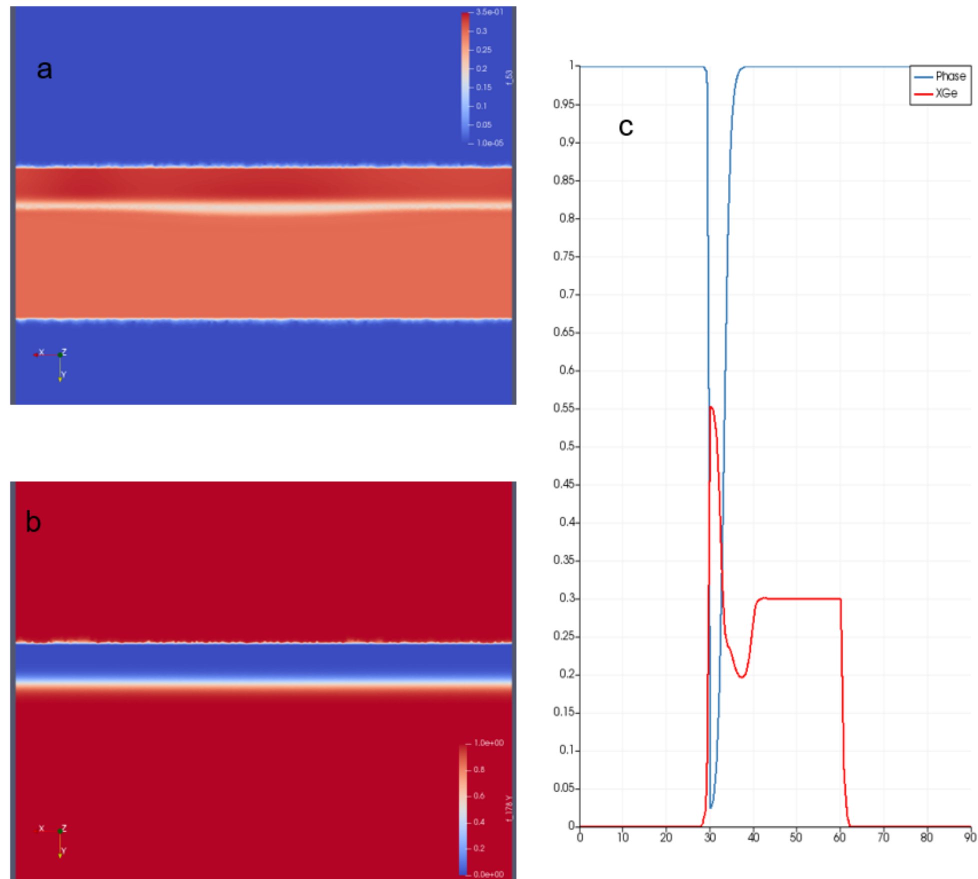

Figure 3.9: Comparison between Ge alloy fraction (a) and Phase function (0 and blue indicate liquid regions while 1 and red indicate solid regions) (b) after 5 ns with respect to the melting nucleation event. The comparison shows how the two quantities are linked, since the molten SiGe front is the main force behind the change in Ge concentration. This is clearer in (c), which shows a cutline of the phase and Ge concentration after 180 ns of LTA. at 1.1 J/cm^2.

particular instance, the process is quite close to the melting threshold of 1.0 $J/cm2$.

This flattening of the simulated melt front in these nano-systems is caused by a capillarity effect inherent in the phase field formulations (as shown in Figure 3.9b) for the same process and time step previously mentioned. Indeed, the curvature dependency of the overheated value results in differing local normal speeds (also with inverted signs) from one site of the l-s front to another region of the l-s front, which hinders the growth of a curved surface (we notice that extremely small curvature radius occurs easily in nano-systems). After the completion of the regrowth process, the SiGe redistributed profile is dominated by the segregation effects (see Figure 3.9c) where the phase function and the SiGe profile are shown along a central cutline in the latest stage of the melting process for the TE 1.1 J/cm^2 fluence case).

Important 2D characteristics in the SiGe alloy profile are only visible for fluences close to the melting threshold E_{th} (i.e., E_{th}+0.1-0.2 J/cm^2), and not for higher fluences. The flattening of the profile, which occurs with increasing fluence size, makes these characteristics less significant.

Qualitatively similar considerations, as the one discussed for the alloy fraction, can be reported for the final dopant redistribution (see e.g. Figure 3.10 for the same process of Figure 3.9). 2D features of the dopant profile are relevant close to the E_{th}. Anyhow, the final profile (Figure 3.10) is the result of the complex overall kinetics of the melting front and some uniform behavior has been simulated (e.g. the oscillations of the final boron profile in central cutlines). Of course, all these features have to be verified especially due to the limitation of the continuum method for such small systems.

We conclude this simulation study with some useful indications of the process windows for the eventual experimental study. As already discussed, a fluence close to the melting threshold could produce a modulated dopant 2D distribution that can be investigated by means of scanning conductivity measurements (SCMs). Therefore, the melting threshold is an important parameter as a guideline of the central point for the experimental Design of Experiments (DoE). In Figure 15 a simulation analysis of the E_{th} as a function of the geometry is presented for the SiGe layer with X=0.3 alloy fraction and 7.4 $10^{19} cm^{-3}$ boron density. In

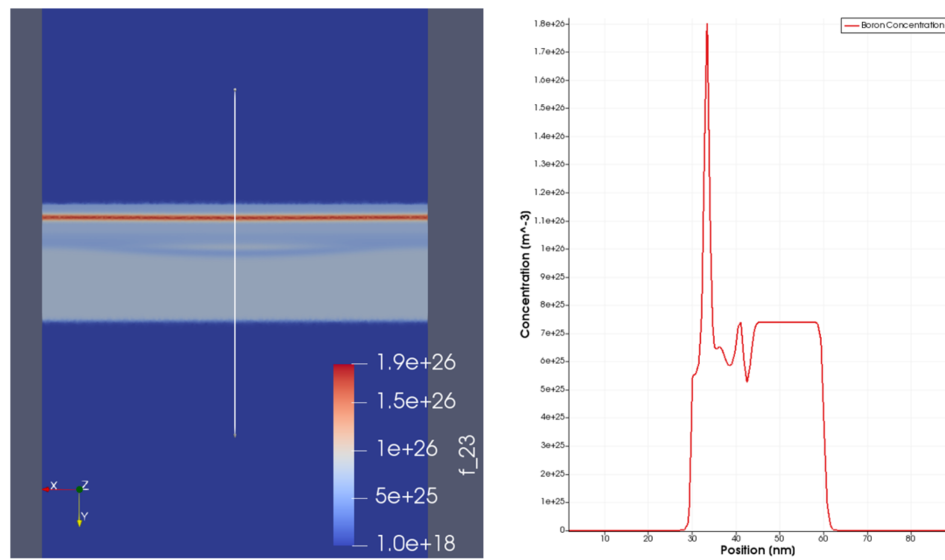

Figure 3.10: Boron concentration profile after 178 ns of LTA at $1.1 J/cm^2$, starting from a constant profile of $7.4\ 10^{25}$ On the left we have a 2d map of the concentration and highlighted the cutline whose results can be seen on the image on the right.

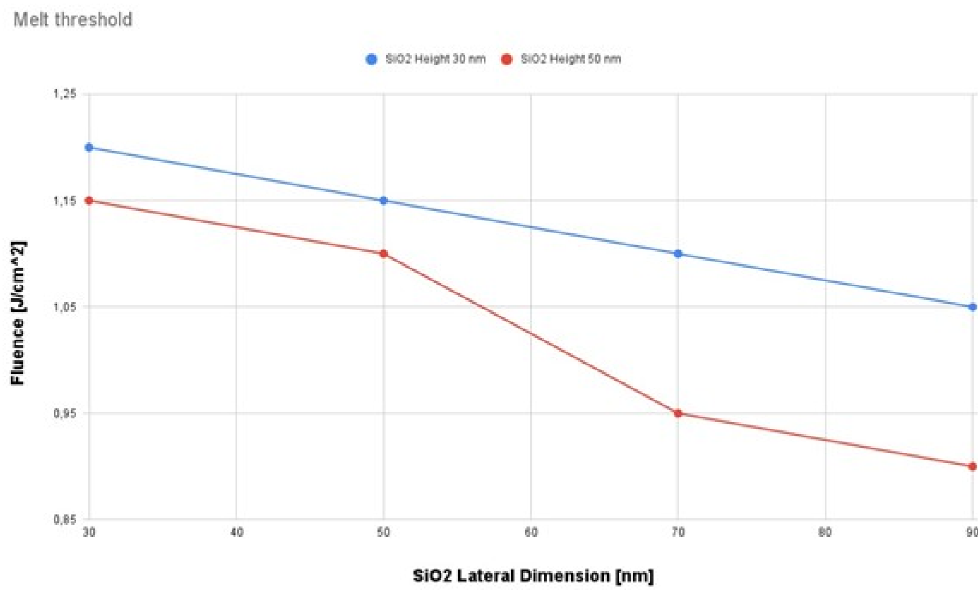

Figure 3.11: Melting threshold dependence on the trenches geometry for a SiGe layer with X=0.3 alloy fraction and 7.4 $10^{19} cm^{-3}$ boron density.

general, the E_{th} is smaller with respect to the 1D substrate case studied previously. As already discussed, this is the result of the anti-reflective effect. Of course, E_{th} is in general smaller for the oxide with 50nm thickness (close to the $\lambda/4$ value) and it monotonically decreases as the oxide width increases (the minimum value is obtained for a blanket stack).

The calibrated parameters are then applied to a more sophisticated construction in a realistic manner. Nanosecond laser annealing in the melt regime was performed on a 2D structure representative of a scaled finFET device to demonstrate on a practical example. The structure shape and dimensions, as shown in Figs. 3.12 a and b, consist of a 2D plane cut in a 3D device structure along the fin direction. They are the nodes of a high-performance PMOS finFET device that are currently in advanced technology.

The gate metal layer stack is made of tungsten (W), with an oxide (SiO2) hardmask on top and nitride (Si3N4) spacers on the sides, and the gate oxide is a thin layer of hafnium oxide (HfO2). The channel, extensions, and Source and Drain (S/D) regions are $Si_{0.75}Ge_{0.25}$, the top of the S/D area (contact) is $Si_{0.5}Ge_{0.5}$, and the bottom fin region is Si. Laser annealing occurs immediately after the contact dielectric opening process. Temperature and phase have a lateral boundary condition that is periodic. The concentrations of boron (B) dopant in the extension are $10^{19}cm-3$, $10^{20}cm-3$, and $510^{21}cm-3$ in the contact region. Boron diffusion parameters were established approximately identically to those in [59], calibrated for Si, where anomalous diffusion is well reproduced, and then extended to Si(1-x)Gex without accounting for alloy fraction dependency.

The laser emits light at 308 nm, with a pulse duration of 160 ns at full-width at half maximum and an ED of 0.75 J/cm^2. For a meaningful understanding of the process dynamics, a comprehensive 3D structural simulation would be required. Nonetheless, in the context of this study, such a 2D geometry allows for a sufficient assessment of trends.

Figure 3.13 displays a typical heat source distribution at the beginning of surface melting. The majority of the heat source is located on the near surface absorbing regions (gate, contact, and top of S/D) due to the limited optical penetration depth in these materials at the laser wavelength (10 nm for both Tungsten and SiGe). Fig 3.13 b represents the simulated temperature distribution and shows the maximum temperature obtained

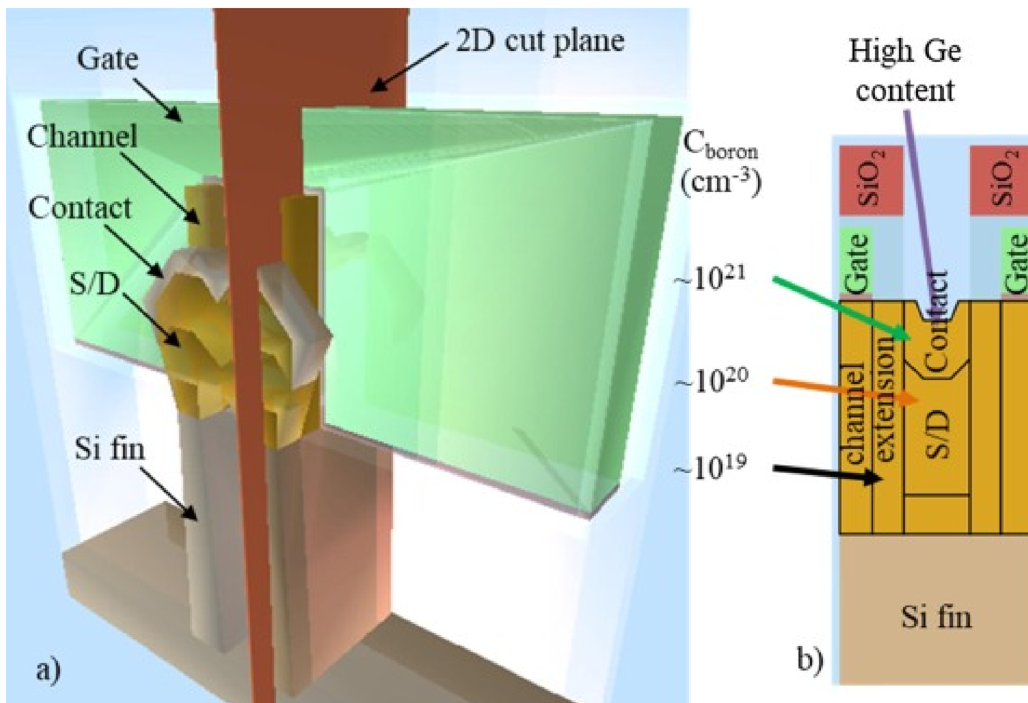

Figure 3.12: (a) A 3D drawing of the structure of the FinFET device of interest. b) Simulated two-dimensional structure cut along the direction of the fin (perpendicular to the gate direction). [57]

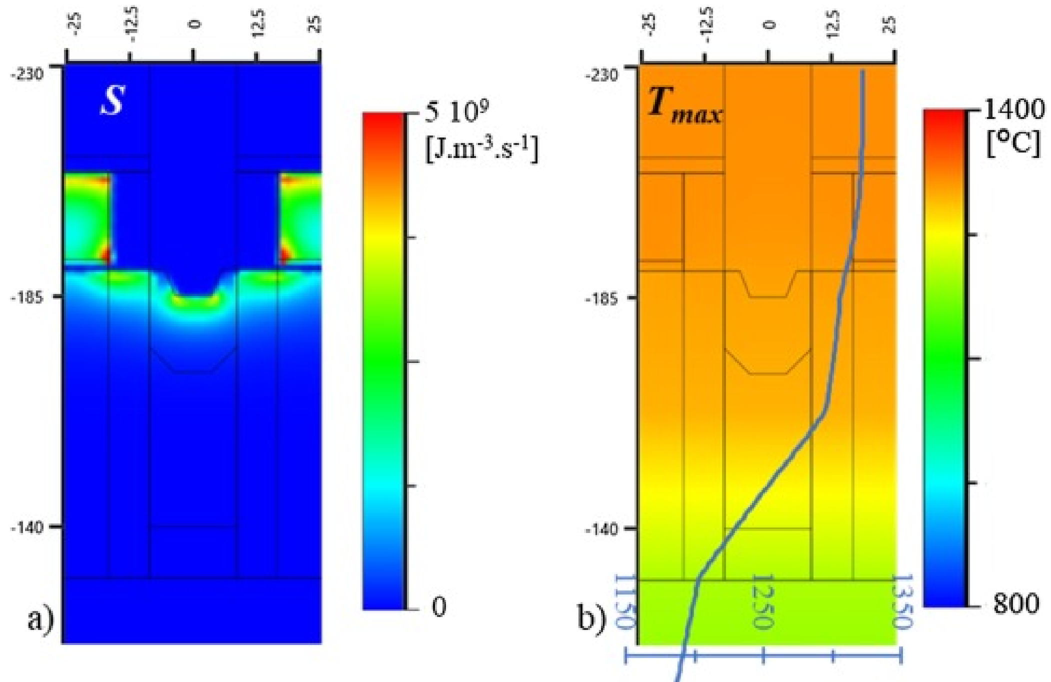

Figure 3.13: (a) Heat source at the time surface melting started. (b) Highest temperature reached during simulation, superimposed on the vertical temperature profile in the center of the structure. [57]

in the structure during the experiment. Because of the significantly scaled size in relation to the thermal diffusion length, the temperature is reasonably consistent laterally (1 m). The gradient inside the melting area is also rather small (0.5 °C/nm), as expected given the liquid layer's high heat conductivity. In non-melting SiGe sections, where thermal conductivity is an order of magnitude lower, the gradient is significantly steeper (up to 3 °C/nm). Such a thermal profile shows that the phase and temperature dependent local thermal conductivity dominates the thermal dynamics at first order in such nanometer-scaled devices during sub-s annealing periods.

Figure 3.14 depicts the distributions of phase (ϕ), temperature (T_{max}), Ge fraction (x_{Ge}), and B concentration fields at the surface melt initiation (t0), maximum melt time (t1), and final time (t2) (heat source). Because of

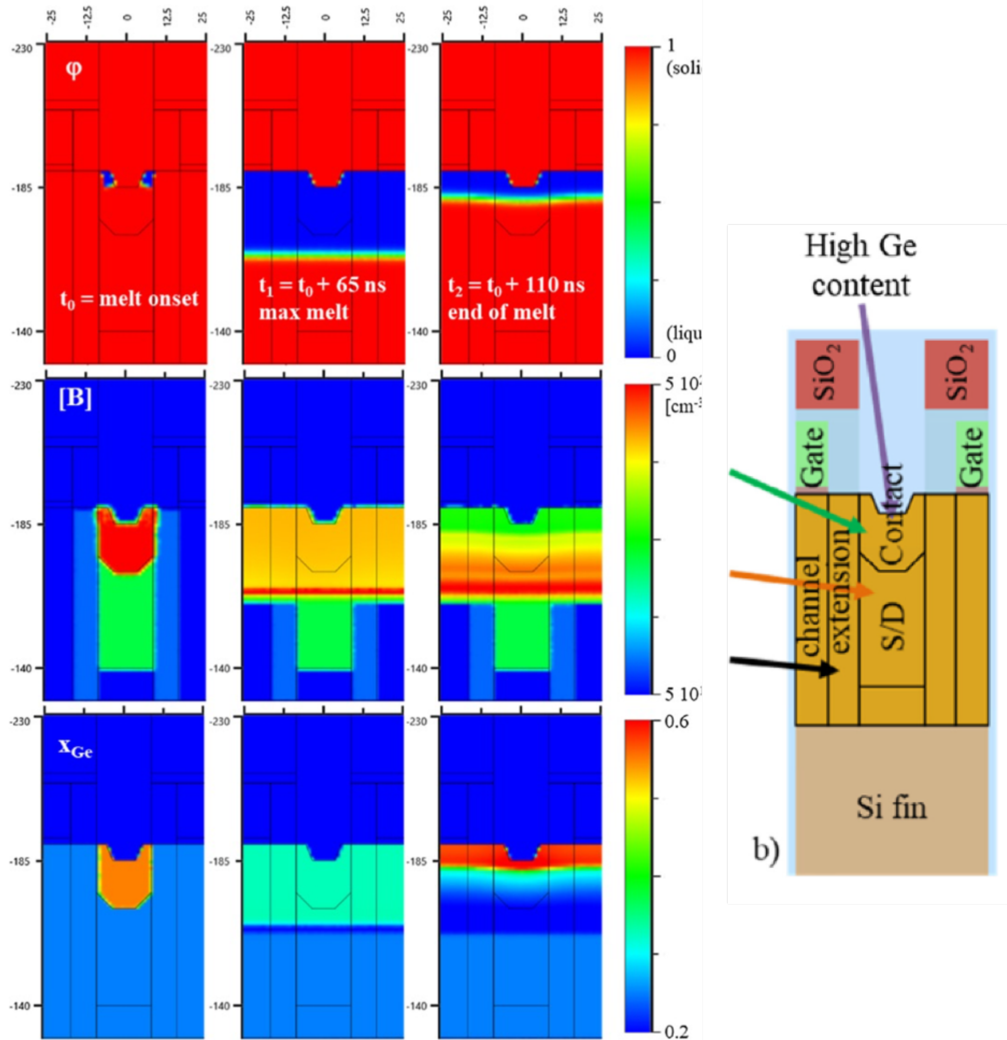

Figure 3.14: Snapshots of Phase (top, 1: solid, 0: liquid), B concentration (center) and Ge fraction (bottom) fields at time of surface melting onset (left), maximum melt (middle), end of melting (right). (B) Ref. [57]

the rapid alloy mixing within this narrow molten zone, the early stage of melting is driven by a melting temperature that interpolates between regions with high Ge content and regions with low Ge concentration. Even in the first nanoseconds after melting begins, the liquid/solid interface curvature becomes very minimal (almost flat) (not shown). The minuscule curvature is induced by a reduction in interface energy as a result of the resolution of the associated temperature and phase field equations, with a flat interface having the least energy. As a result, the energy released by curvature relaxation is greater than the small quantity of latent heat-related energy required to melt the lower Ge fraction region.

The evolution of the Ge percentage shows the expected surface segregation described in previous investigations, with a slightly higher concentration near the structure's core due to the aperture's V shape. A high Ge fraction can be beneficial for p-type contact formation by lowering the Schottky barrier height [21], lowering contact resistance. Finally, B concentration within the molten zone exhibits lateral redistribution, with anomalous diffusion creating a pile-up near the maximum melt depth. Under these settings, unwanted B diffusion occurs in the extension and channel areas, which may result in poor short channel performance.

The first strategy for minimizing such diffusion is to reduce the laser ED to limit the melting region to the contact zone, which requires careful laser energy control. Another possibility is to pre-amorphize a shallow piece of the contact region, increasing the melting temperature differential between the surface and the rest of the structure. In this case, the laser condition will need to be fine-tuned again in order to successfully repair the associated implantation faults.

In this chapter, we discussed the material calibration process for a totally self-consistent laser annealing simulation model incorporated into the LIAB TCAD framework. The calibration approach employs extremely basic structures, including diffusion marker species and uncomplicated characterization techniques. In addition, an in-situ time-resolved metrology system is utilized. We have a solid grasp of the fundamental material qualities that need to be calibrated, which include the diffusion parameters (segregation, diffusion) and the optical properties. The technique was successfully applied to Ge and Si(1-x)Gex (where x = 0.2, 0.3, and 0.4) and acceptable agreement with experimental data was achieved. As

an example 2D application case, the laser annealing of an advanced p-type finFET with SiGe contact areas was modeled. This demonstrated that process flow optimization and precise control of laser annealing settings are necessary to avoid undesirable melt-mediated diffusion effects.

Chapter 4

Nanoscale effects on thermal transport

This chapter concentrates on the original PhD project of implementing phonon-mediated heat transport model corrections in our software. We will provide a thorough theoretical foundation that explains our method and motivations. The heat transpot model is then presented, along with some basic thermal conductivity analyses that serve as a first validation stage. When we compare our results from the revised continuum model with Non Equilibrium Molecular Dynamics (NEMD) simulations done by our colleagues at Fraunhofer institute, we get a more robust validation. As with SiGe, the final validation stage involves using the corrected heat transport model with more complicated structures that are more akin to an actual device grade model than a toy model.

The release of energy towards a processed sample is probably one of the most important aspects of material manipulation processes. Temperature control, heating, annealing and quenching are mandatory keywords of any sample preparation method in the scientific literature. Often, when standard laboratory practices for macroscopic samples are directly applied to the manufacturing of nanoscaled systems, they become critical. If, additionally to the system size, also the process time shrinks (as in the case of Laser Thermal Annealing (LTA) with nanosecond range pulses[60]), the critical issues become huge and the accurate process control requires basic research also supported by reliable modeling. An accu-

rate theoretical approach of heat transport at the nanoscale relies either on direct solutions of the Boltzmann Transport Equation (BTE) for phonons [61], or on atomistic simulations in the Molecular Dynamics framework [62]. These methods are fundamental for achieving a deep understanding of the energy transport in particular nanosystems, but their application could be too cumbersome when applied in a thermal process simulation.

Indeed, an advanced simulation of a thermal process (including a laser process) aims at predicting the modifications of a material presumably in the presence of complex structures (e.g. with nm wide elements made of different materials/phases and in thermal contact with meso- and macroscopic objects like substrates, supports etc.). Moreover, it is generally a multi-physics problem where several "fields" [50, 63, 1, 44, 64, 2, 3, 46, 4] (i.e. electromagnetic field, impurity density, local time-dependent phases, etc.) self-consistently interact with the temperature field. In this framework, heat transport is usually modeled by means of numerical solutions of the Fourier Law (FL), expressed as a Partial Differential equation (PDE), by means of the finite element method (FEM) or similar numerical schemes, when suitable space-time dependent heat sources and boundary conditions are defined.

Such approach shows strong limitations for nanoscale systems with complex boundaries and material specifications, where e.g. the regime of transport for phonons can change from diffusive to ballistic. As a consequence, an appealing improvement of the heat transport model for structures with component sizes comparable to their intrinsic phonon mean-free paths should maintain this continuum description in order to allow for a direct integration in process simulators while introducing a proper formulation for the corrections due to the phonons' dynamics. Advancements in this sense appear in the recent literature [65, 66], where the important general conclusion is that corrections due to the finite size of the system are based on Fourier law-like PDEs (where the thermal conductivity is the only material-dependent parameter in the bulk), whilst boundary conditions (BCs) of the corrections have to be significantly modified in order to consider the transport of phonons.

For the sake of consistency, we report the foundations of our work based on this article from 2017 [65]

4.1 Basic formulation

This work builds on Peraud and Hadjiconstantinou's article [66], in which they demonstrated that the zeroth order solution is the classic Fourier's law solution with fixed temperatures at the boundaries, whereas the first- and second-order solutions involve temperature jumps at the boundaries. Their study establishes that, up to second order, the thermal conductivity in the bulk is identical to the unmodified bulk conductivity regardless of the structure's size. They emphasize that incorporating an effective thermal conductivity into compact structures is not necessary, as thermal transmission is reduced due to temperature jump boundary conditions, not thermal conductivity. They reached the same results in the work that we analyzed and used as a foundation. The primary distinction is that Peraud and Hadjiconstantinou asymptotically expand the entire BTE while concentrating on the small Knudsen number regime. In contrast, the proposed study begins with the McKelvey–Shockley equations and then demonstrates that these equations lead directly to Fourier's law and that temperature jump boundary conditions develop naturally when physically correct boundary conditions are used for the BTE.

Additionally, Peraud and Hadjiconstantinou enhanced their model by incorporating kinetic boundary layer functions to account for non-linear temperature profiles near the boundaries. In this model, we ignore these border layers and apply Fourier's rule to the entire region enclosed by the contacts. Our solution is less precise for moderate Knudsen number(a dimensionless number calculated as the molecular mean free path length divided by a relevant physical length scale) values, but it is exact in the diffusive and ballistic limits. The primary conclusion of this work is consistent with that of Peraud and Hadjiconstantinou—that one should use the unmodified Fourier's law inside a nanostructure but modify the border conditions to a jump type boundary condition.

We begin with the steady-state flux equations as written by Shockley 19,20

$$\frac{dF_Q^+(x)}{dx} = -\frac{dF_Q^+(x)}{\lambda} + \frac{dF_Q^-(x)}{\lambda} + \frac{S}{2} \tag{4.1}$$

$$\frac{dF_Q^-(x)}{dx} = -\frac{dF_Q^+(x)}{\lambda} + \frac{dF_Q^-(x)}{\lambda} - \frac{S}{2} \tag{4.2}$$

where $F_Q^+(x)$ is the forward-directed heat flux, $F_Q^-(x)$is the negative-directed heat flux, and λ is the mean-free-path for backscattering. The term, S, is a heat generation term assumed to be spatially uniform. The mean-free-path for backscattering is related to the conventional mean-free-path, $\Lambda = v_s\tau$20,21

$$\lambda = \frac{4}{3}\Lambda \tag{4.3}$$

Temperatures can be associated with the forward and revers fluxes12

$$F_Q^+ = v_x^+ \frac{C_V}{2} T^+ \tag{4.4}$$

$$F_Q^- = v_x^+ \frac{C_V}{2} T^- \tag{4.5}$$

where $v_x^+ = v_s/2$is the average $+x$-directed velocity, C_V is the specific heat per unit volume, and v_s is the sound velocity. T^+ and T^- should be understood to be temperatures relative to a background temperature, T_0.12 Small deviations in temperature are assumed so that the specific heat can be treated as a constant. Our use of two different temperatures for the forward and reverse streams has been discussed in Ref. [67] and is analogous to how the electrochemical potential has been defined at the nanoscale[68]. As discussed in Ref. [67], the forward and reverse halves of the distribution are assumed to be near-equilibrium distributions characterized by two different temperatures. Although each half is a near-equilibrium distribution, the overall distribution can be very far from equilibrium as the ballistic limit is approached. Local thermodynamic equilibrium, which would characterize the distribution with a single temperature, is not assumed. Finally, we note that the flux equations can be derived from the Boltzmann transport equation. They can be regarded as a type of differential approximation to the equation of phonon radiative transport (EPRT) in which we integrate separately over the forward and reverse directions rather than over all directions. By adding

and subtracting Eqs. 4.1 and 4.2, we find

$$\frac{dF_Q}{dx} = S \tag{4.6}$$

$$F_Q = -kbulk\frac{dT}{dx} \tag{4.7}$$

where

$$F_Q(x) = F_Q^+(x) - F_Q^-(x) \tag{4.8}$$

is the net heat flux,

$$k_{bulk} = \frac{v_x^+ \lambda}{2} C_V = \frac{1}{3} v_s \Lambda C_V \tag{4.9}$$

is the thermal conductivity, and

$$T = (T^+ + T^-)/2 \tag{4.10}$$

is the average temperature of the forward and reverse heat fluxes. Equations4.6 and 4.7 lead to a steady-state heat diffusion equation,

$$\frac{d^2T}{dx^2} = \frac{S}{k_{bulk}}(4.11)$$

that is mathematically identical to equations 4.1 and 4.2 and since they applies from the ballistic to diffusive limits. Accordingly, Eq. 4.11 also applies from the ballistic to diffusive limits. The thermal conductivity, k_{bulk}, is not size dependent (unless we bring in surface roughness scattering). The fact that Fourier's law and the heat diffusionequation can be used from the diffusive to ballistic limits with the bulk thermal conductivity has been discussed in Ref. [67]. We must, however, be careful about the boundary conditions when using 4.11[67] . We shall see that a size dependent "apparent thermal conductivity" results when the proper boundary conditions are used. Peraud and Hadjiconstantinou reached the same conclusion[66]. The boundary conditions for the phonon BTE are the incident heat fluxes from the two contacts. (Ideal black body contacts are assumed.) The temperatures at the two ends of the film are a result of the calculation and can only be imposed in the diffusive limit.

As shown in Ref. [67], when the correct boundary conditions are used, temperature jumps can occur—even for ideal contacts. The temperatures at the two contacts can be written as

$$T(0^+) = T_L - \Delta T(0) \tag{4.12}$$

$$T(L_x^-) = T_R - \Delta T(L_x) \tag{4.13}$$

where T_L is the temperature of the left contact and T_R is the temperature of the right contact. The temperature jumps can be shown to be the product of the net heat flux and one-half of the ballistic thermal resistance12

$$\Delta T(0) = F_Q(0)\frac{R_B A}{2} \tag{4.14}$$

is the net heat flux,

$$\Delta T(L) = F_Q(L)\frac{R_B A}{2} \tag{4.15}$$

where A is the cross-sectional area and

$$R_B A = \frac{2}{C_v v_x^+} \tag{4.16}$$

is the ballistic thermal resistance. Note that R_B is a fundamental thermal boundary resistance for the assumed ideal, reflectionless (black) contacts. Real contacts would have additional interface resistance.

4.2 Heat transport model

Starting from th interesting results of the previous section, we have integrated phonon transport corrections to our existing simulation tool LIAB , in order to reproduce experimental data and predict the behavior of various material structures upon thermal annealing, including laser annealing. Our continuum modelling is thus integrated in a FEM framework and the corrections allow for achieving a calibrated method able to simulate thermal processes from the diffusive to the ballistic regime of phonon dynamics. Within this approach, we have simulated different cases where heating is induced by conventional and laser annealing in

various complex bi- and tri-dimensional (2D and 3D) structures. Results are in excellent agreement with the experiments and demonstrate that a continuous treatment of thermal transport is possible in complex nano-sized systems in thermal contact with macroscopic objects. Here there are a brief recap of the previous conclusions as well our way to implement them in our tool.

The Fourier Law can be expressed as:

$$\vec{F}_Q = -k\nabla T \tag{4.17}$$

where F_Q is the net heat flux, k is the thermal conductivity and T is the temperature. Eq. 4.17 is ubiquitously applied for the study of heat diffusion problems and it can be formally derived from the BTE, for local phonon distributions close to the thermodynamic equilibrium, assuming the continuum limit and the diffusive regime [69]. Recently [66] a systematic expansion in terms of continuum quasi-thermal fields has been derived, indicating that FL is the correct zero-order approximation for the phononic BTE in the (diffusive) limit of a small Knudsen number $\langle Kn \rangle$. We notice that $\langle Kn \rangle$ is a dimensionless number defined as the ratio between the average phonons' mean free path and the representative length of the system in study. In the diffusive approximation the same derivation [66] demonstrates that the usual:

1. Dirichelet: $T = T_0$
2. Neunmann: $\nabla T = 0$
3. Continuity $-k^1\nabla T_1|_\Gamma = -k^2\nabla T_2|_\Gamma$ and $T_1|_\Gamma = T_2|_\Gamma = T$

relations are the correct boundary conditions respectively for: 1) The thermostat at T_0 temperature; 2) The diffusely specular wall; 3) The interface Γ between two materials 1 and 2 with thermal conductivities k_1 and k_2. The analysis of high order corrections in $\langle Kn \rangle$ shows that these are ruled by FL-type equations in the bulk (all ruled by the bulk conductivity), whilst boundary conditions have to be modified with jump-type BCs for the temperature [66]. Interesting analytic results in simple one-dimensional systems [65] show that by using the FL and suitable jump BCs, we can obtain exact solutions in the diffusive $\langle Kn \rangle << 1$ and ballistic $\langle Kn \rangle >> 1$

limit, while the solutions deviate only a few percent points with respect to the BTE solution in the intermediate $\langle Kn \rangle \sim 1$ region. If we consider a system in contact with a thermostat at a T_0 temperature, the jump boundary conditions can be written as:

$$\hat{n} \cdot \vec{F}_Q = k_{bulk} \lambda^{-1} (T - T_0) \tag{4.18}$$

Where $\vec{F}_Q = \vec{F}_Q^+ - \vec{F}_Q^-$ is the combined phonon flux coming from the left and right size of the junction between the nano-system and the thermostat, k_{bulk} is the bulk thermal conductivity of the material and λ is the average phonon scattering length, which can be related to known and measurable material properties as

$$\lambda(T) = 4k_{bulk}(T)/C(T)v_s(T) \tag{4.19}$$

where $v_s(T)$ is the sound velocity and $C(T)$ is the thermal capacitance, which is also used in the time dependent bulk equation for the T field

$$C(T)\frac{\partial T}{\partial t} = \nabla \cdot [k_{bulk}(T)\nabla T] + S(t) \tag{4.20}$$

with $S(t)$ the eventual time dependent internal source. Eq. 4.20 is numerically solved in the simulation results of sec. 4.5.

We note that the interpolating boundary correction Eq. 4.19 derives from a multiple-temperature approach to the local non-equilibrium, due to ballistic effects. T is the average temperature [65] and the multiple temperature collapses to a single T in the diffusive limit. If the system is significantly smaller than λ (ballistic limit, $\langle Kn \rangle << 1$) the corrected BCs in Eq. 4.18 impose that the phonon modes which are in thermal equilibrium with the thermostat at T_0 and at the interface do not thermalize with inner phonon modes: i.e. they reproduce correctly the behaviour in the ballistic regime (details are discussed in Ref. [65]).

Extending this derivation with arguments coming from the Chapman-Enskog like expansion of Ref. [66], we have to consider again the jump solutions at different temperatures T_1 and T_2 at the interface between two regions made of different materials. Consistently to the interpolating correction at the thermostat surface (Eq. 4.18), the discontinuous solutions at the material's boundary Γ are:

$$-k^1_{bulk}\nabla T_1 = \hat{\Gamma}(T_1|^+_\Gamma \hat{n}_1 + T_2|^-_\Gamma \hat{n}_2) \tag{4.21}$$

Where $\hat{n}_1 = -\hat{n}_2$ are the local outward normal unit vectors to the two sides of the boundary and $\hat{\Pi} = (k^1_{bulk}\lambda_1^{-1} + k^2_{bulk}\lambda_2^{-1})|_\Gamma$ is the local phonon scattering functional. Moreover, the energy conservation condition at the boundary has to be imposed as [66]:

$$-k^1_{bulk}\nabla T_1|_\Gamma = -k^2_{bulk}\nabla T_2|_\Gamma \tag{4.22}$$

Eq. 4.22 acts as a closure of the model at the interface location. We note that an external boundary simulating a virtual interface with the same material is still ruled by the Neunmann relation $\nabla T = 0$. In the following we will discuss the impact of the thermal mode equations introduced here (Eqs. 4.18-4.22), by comparing corrected and standard solutions (i.e. solutions with strictly diffusive BCs) in the heating processes of 2D and 3D systems.

4.3 Effective conductivity analysis

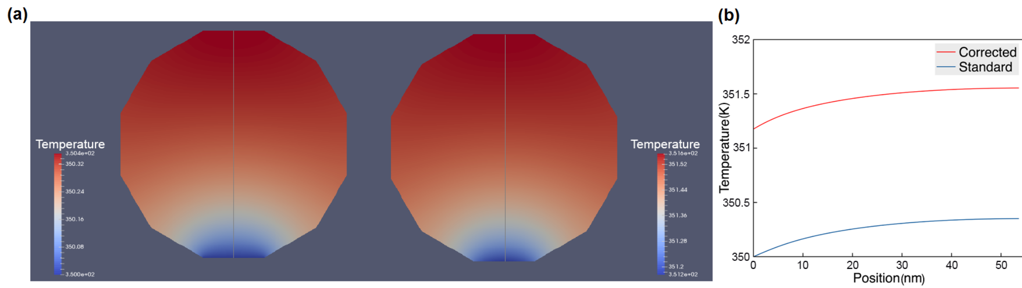

Figure 4.1: : (a) Cross section of a heated Si nanowire with a diameter of 56 nm: standard (left) and corrected (right) solutions. (b) Standard and corrected T values along the nanowire diameter line shown in (a). In the Finite Element Methods used to solve the heat equation, the correction is implemented as a jump-like (i.e., Robin-type) boundary condition. Due to the nanoscale of the system, the discontinuity at the device/thermostat interface reproduces the incomplete thermalization of the internal phonon modes.

We start our analysis with Si nanowires (NWs) having their equilibrium shape [70] (i.e. an almost regular polygon with 12 edges) and different diameters. These are in contact with one or two thermostat(s) along one or two perimeter edge(s), while internally heated by a uniform source. The effective phonon scattering length λ is the only physical quantity of the model which, in all the results presented in this paper, has been calibrated using the experimental values of $k_{bulk}(T)$, $C(T)$ and $v_s(T)$ which can also depend on T.

In Fig. 4.1(a) we report a cross section, perpendicular to the Si NW axis, of the thermal field obtained for the standard Dirichelet BC(s) (left side) and the corrected BC(s) expression (right side) for the edge(s) in contact with the thermostat. The temperature obtained in the two cases along the NW diameter connecting the center of the thermostat edge and the opposite edge is shown in Fig. 4.1(b). For the thermal calibration of Si we used values deriving from Ref. [37] whilst the sound of speed was set to $v_s = 6400 m/s$ [72]. In the simulations of single Si NWs (Fig. 4.2) the internal source is tuned in order to obtain an increase of the order of $\sim 1K$ for the internal temperature with respect to the thermostat. The difference between the standard and the corrected solution is relevant for this structure and it tends to enlarge(decrease) for smaller(larger) NWs (see also section S1 of the supplementary material).

Si NWs are reference systems for the study of phononic energy transport and they have been subjected to extensive experimental analyses. The interest on Si NWs has been intensified from the apparent scaling of the thermal conductivity with the diameter of the NW and several papers reported these evidences. As a consequence, our model predictions could in principle be compared also with the experimental results. As a matter of fact, measurements are based on the "FL equivalent" behavior of the system: they are dependent on the uniform heat source and they have to be correctly interpreted in terms of the real microscopical behavior.

A direct method to compare the experimental [71] and theoretical results uses the apparent conductivity k_{app} concept [65]. k_{app} is a geometry dependent parameter which describes a thermal field distribution T obtained in real and numerical experiments, assuming that the constitutive equation of T is the standard FL. As a consequence $k_{app} \simeq k_{bulk}$ in large systems while in the nanoscale its geometrical dependence includes also

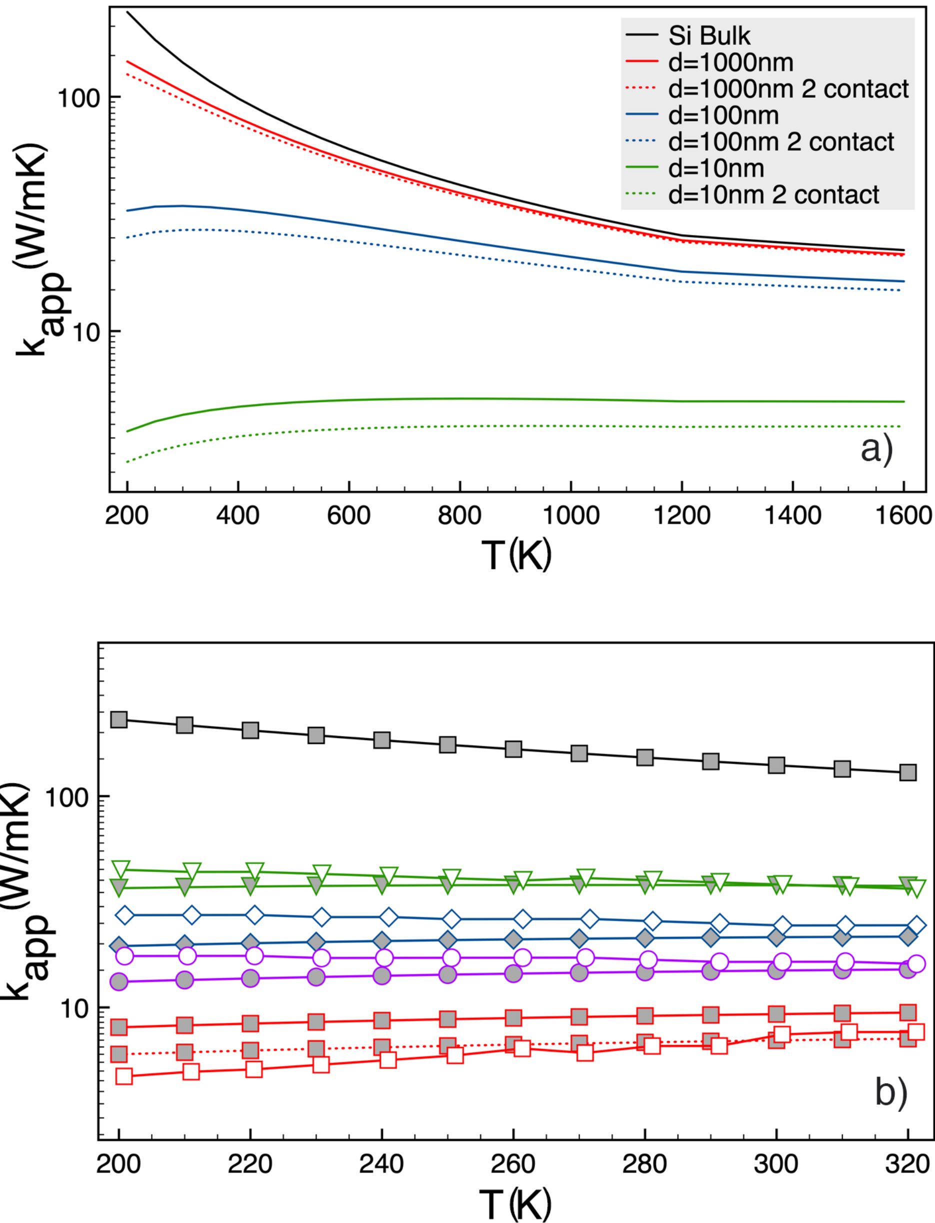

Figure 4.2: a) Evaluation of the apparent thermal conductivity for Si NWs with one and two thermal contacts and different sizes: 10nm (green lines), 100nm (blu lines), 1000nm (red lines). Bulk Si thermal conductivity is shown as a black line. b) Comparison of simulated (filled grey markers, plain line for one contact, dotted for two contacts) and observed (empty markers) thermal conductivity for Si NWs with different sizes: 22 nm (red lines), 37 nm (purple lines), 56 nm (blue lines), 115 nm (green lines). Bulk Si thermal conductivity is shown as a black line. Experimental data extracted from ref. [71]

the real or virtual realization of the thermal contacts with the environment (e.g. the experimental apparatus). Following Ref. [65] we have calculated k_{app} with the results of our NW simulations as

$$k_{app}(T) = k_{bulk}(T)\frac{\langle T_{standard} - T_0\rangle}{\langle T_{corrected} - T_0\rangle} \tag{4.23}$$

where $T_{correct}$ and $T_{standard}$ are the corrected and diffusive temperature fields evaluated numerically, the symbol T_0 is the thermostat temperature while $\langle\rangle$ indicates the average of the field expression over the space region occupied by the structures. The approximate estimates of k_{app} have been compared in Ref. [65] with direct Monte Carlo solutions of the Boltzmann transport for the thin film geometry. The discrepancies between the two methods are globally below 6% and tend to zero in the ballistic and diffusive limits. Similar deviance could be expected if the continuum method is compared to accurate predictions based on the phonon mean free path sampling approach of Ref.[73].

In figure 4.2 (a) the apparent conductivity $k_{app}(T)$, evaluated in a broad temperature range for Si NWs of different sizes and in the cases of the two types of thermal contacts, are compared with the $k_{bulk}(T)$ of bulk Si. We notice that the investigated temperature range starts at 200K since at lower temperatures the phonon quantization makes our continuum analysis unfeasible. $k_{app}(T)$ is close to the bulk value for meso-structures in the μm range, while there is an important average reduction of $k_{app}(T)$ and a strong geometric effect for sizes of the order of $\sim 100nm$ and below. Consistently, we note that the quantitative value $k_{app}(T)$ significantly depends on the contact realization procedure at the nanoscale, while this dependence is less important at the mesoscale.

Our theoretical estimates of $k_{app}(T)$ can be compared with experimental measurements of the thermal conductivity, since any procedure of conductivity measurement implicitly uses the FL for the data analysis (i.e. we could reliably assume that experiments measure the apparent conductivity $k_{app}(T)$ of the nanosystem in a given configuration of the contacts). These comparisons are shown in Fig. 4.2 (b), where experimental data (empty symbols) are extracted by the data discussed in Ref. [74] while the numerical evaluations of $k_{app}(T)$ are plotted for single (solid lines) and double (dashes) contacts. Considering the numerous effects

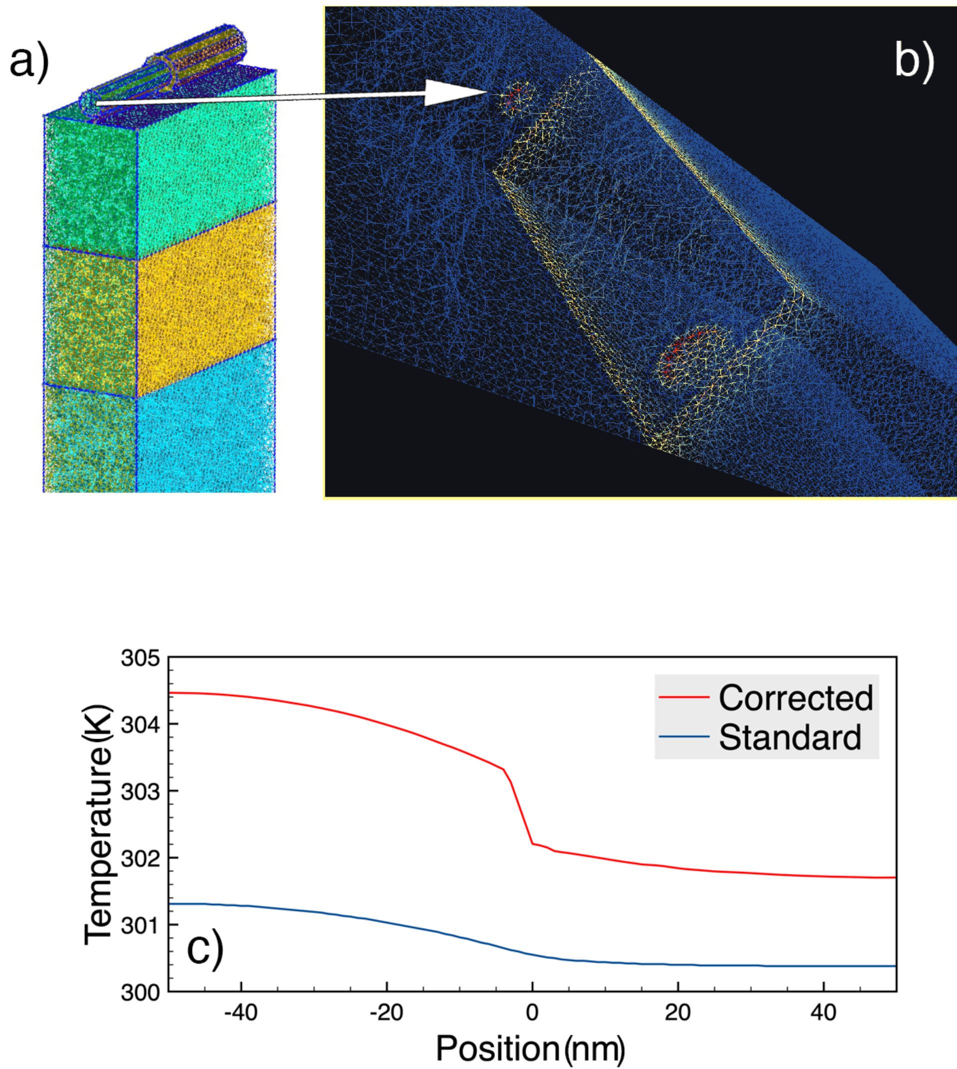

Figure 4.3: (a) CAD model and mesh of a Ge Telescopic NW on a Si substrate; the colors denote the various elements utilized to construct the CAD geometry. (b) The heat source distribution mapped on the FEM-calculated structure mesh. The arrow denotes corresponding locations in panels (a) and (b). (c) Comparison of thermal profiles obtained after 5 ns of simulated LTA using standard and corrected BCs.

that can impact this analysis (e.g. the heat sources and the realization of the thermal contacts, the difference between real and ideal NW edges, the uniformity of the size along the NW axis, etc.), the agreement between calculations and measurements is noteworthy. Finally, we notice that the differences in the calculations of $k_{app}(T)$ for the single and double contacts and fixed size should have a counterpart in the experimental measurements, if the same nano-system is studied with different measurement techniques or procedures.

4.4 Model Validation with non equilibrium molecular dynamics

The first validatation of our continuum model is a comparison of our results with Non-Equilibrium Molecular Dynamics (NEMD) calculations performed in LAMMPS, by considering axial heat transfer along Si nanowires heated uniformly with 15 eV/ps through end lids coated by amorphous SiO2 layers. This structure design provides conditions for axial heat transfer including heat transport through the Si/SiO2 interface. The simulations were performed using Tersoff potentials. The atomic structure of the amorphous silicon dioxide material was simulated by heating of crystalline SiO2 above the melting point, followed by a quench. Periodic boundary conditions were set at the boundaries of the MD simulation box. Unfortunately, such a set-up was difficult to reproduce in continuum approaches. To bridge MD to continuum simulations, Langevin thermostats were applied in the outermost 4 Å of the SiO2 boundary regions to match the Dirichlet boundary conditions used in the continuum approach. In the continuum model taking into consideration phonon transport corrections, separate temperature fields (e.g. T1 and T2) in the material bulk regions are ruled by a Fourier law-like heat equation with the bulk conductivity values (e.g. k1 and k2). Standard continuity conditions (T1=T2) at the interface between different materials are replaced by jump conditions mentioned above.

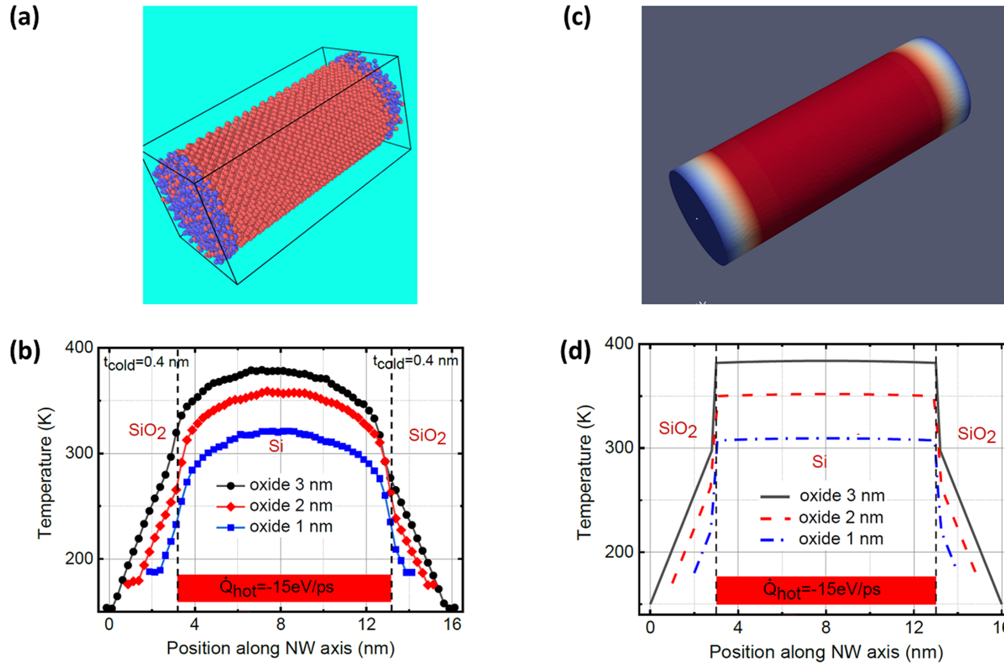

Figure 4.4: (a) Atomistic scheme of a cylindrical Si nanowire end-coated with SiO2. (b) Temperature distribution along the axis of the cylindrical Si nanowire end-coated with SiO2 (see the upper part of the figure) obtained with molecular dynamics within the canonical ensemble (using Langevin thermostats). The lowest temperatures in the thermostat-controlled regions are 187, 175, and 153 K for the a-SiO2 layers with thicknesses of 1, 2, and 3 nm, respectively.(c) Continuum representation of a cylindrical Si nanowire end-coated with SiO2. (d) Temperature distribution along the axis of cylindrical Si nanowires with 1-, 2-, and 3-nm-thick amorphous SiO2 layers on the nanowire tips (upper) obtained within the continuum model.In this case λ_{Si} = 59.6 nm and λ_{SiO2} = 30.2 nm

Results shown in Figure 4.4 show a good quantitative agreement between the MD results and the corrected continuum solutions, particularly with respect to the maximum temperature value reached within the nanowire, as well as with the change of the slope of the thermal conductivity and the interface between the two materials. The used values of the

average phonon scattering lengths are calibration parameters (see Figure 4.4 caption) which agree with the expression in eq. 4.19 when the other quantities are estimated with the same MD scheme. Some variations persist at the edges of the nanowire due to the smooth, non-ideal, interface between Si and SiO2 in the MD simulations, which could require further modeling in the continuum model. Overall, the corrected continuum approach is able to capture most qualitative aspects of the thermal conductivity and appears to be a viable solution with low computational cost for the heat transport in nanostructures.

4.5 Simulations of complex systems

After the integration of the corrected boundary conditions in the computational code of LA, we can simulate the full LA process. As an example, we have investigated the laser thermal treatment of a 56 nm wide infinite Ge nanowire on a Si substrate. The presence in the device structures of an interface between crystalline and amorphous materials needs a proper "ad-hoc" calibration for the interface boundary expression since the average phonon scattering length cannot be properly estimated by means of material properties in the amorphous phase. A ubiquitous example is an interface between the structure and the air. In the modeling of the process we introduced a scattering length λ_{air} to represent the air side of the interface between the studied system and the air portion itself. Figure 4.5(a) shows the heat source distribution deriving from the absorption of a laser pulse of $\approx$ 160 ns width and wavelength of 308 nm after 5 ns heating for a value of the scattering length of λ_{air} = 3 nm. Using this computed source distribution we simulated the heating using corrected and standard boundary conditions. Further analysis of corrected versus standard solutions can be seen in Figure 4.5(b), where the effect of heat confinement is more evident. We notice that the setting of the interface parameters for the crystal-amorphous boundary is a critical issue of the method and deserves further studies also with the aid of MD simulations.

Another demonstration of the reliability of the approach based on jump solutions for the heat transport equation opens perspectives for its application in the simulation of the annealing process of complex

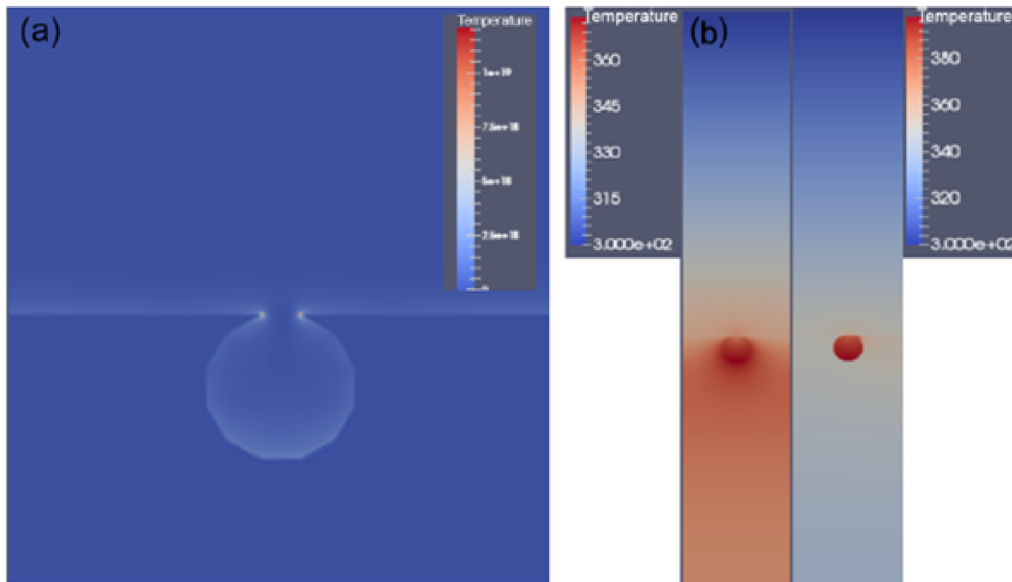

Figure 4.5: (a) Source distribution after 5 ns heating with air = 3 nm. (b) Comparison between the results of the pulsed LA heating process after 30 ns from pulse starting instant with air = 3 nm without (left) and with (right) the corrections.

nanosystems. However, whilst the formal extension of the method is rather straightforward, its numerical implementation is more difficult due to the possible presence of solution discontinuities at the boundaries of the material. We have implemented the discontinuous Galerkin FEM approach in the time-dependent LIAB solver (see supplementary material S2) in order to numerically address this issue. In the following, we present some examples of laser annealing process simulations in complex nanosystems where the conventional and corrected solutions are compared.

The first system (see figure 4.3 (a) where the used computational mesh is shown) is composed by a Ge telescopic NW (10 nm + 15 nm diameters) immersed in air and deposited over a Si substrate. In this geometry a thermal contact forms between the substrate and the larger portion of the telescopic NW. The used value of the speed of sound in Ge is $v_s = 5400 m/s$[75], while the interface with the air is ruled by an effective value of $\lambda_{air} = 3nm$ (see also supplementary materials for a discussion on the effect of this parameter). The calibration of the thermal parameters for Ge is that reported in Ref. [74] (being also the default calibration in LIAB). LIAB implements a self-consistent solution of laser annealing, where the heat source (see Fig. 4.3 (b) for the source distribution of a transverse electric incident wave) is evaluated by means of the solution of the Maxwell equations in the time-harmonic approximation, once the temperature field is known [37]. In our simulation, we use the same laser pulse setting (wave length 308 nm, pulse width $\sim$ 160 ns, see section S3 of the supplementary material) of Ref.[37] and a fixed energy density of $0.4 J/cm^2$.

The solutions (corrected and standard) of the thermal field distribution along the NW axis obtained after 5 ns of simulated annealing are shown in Fig. 4.3 (b). The different temperatures (blue lines) obtained in the two sides of the junction when the standard FL rules the transport are due to a combined effect of different sizes and the differently absorbed heat. However, the solution is obviously smooth along the NW junction axis. A completely different heat distribution is calculated for the corrected solution. Apart from the different average values of the temperature that are caused by overall reduced heat dissipation when phononic corrections are included at the nanoscale (confirmed by the previous anal-

ysis of the apparent conductivity), we can also observe an abrupt change of the temperature at the junction of the telescopic NW. We note that no contact resistance correction has been added in the heat transport model at the junction position, since the junction is not a material boundary, and this jump is caused only by the different types of BCs, considering a finite scattering length for the phonons at the material interfaces (the larger NW only forms a thermal contact with the Si substrate).

LTA has a great application potential for microelectronics and, as a consequence, we have tested our method considering the complex structure of a FIN-shaped field effect transistor (FINFET). The simulation of the LTA process with the FL of heat diffusion for a Si FIN partially embedded in a SiO_2 layer and a tungsten (W) gate (see 4.6 (a)), has been extensively discussed in ref. [37]. The used mesh is shown in figure 4.6 (a) while the heat source distribution evaluated with the corrected model after 5 ns is shown in figure 4.6 (b) (laser energy density of $0.4J/cm^2$). For the phononic correction parameter we used $v_s = 5600$ [76] and $v_s = 5200m/s$ [75] in the SiO_2 and W regions, respectively. A comparison between the temperature field obtained with both the FL and the corrected model along a symmetric axis passing trough the FIN center demonstrates that corrections are necessary for an accurate simulation, although the differences are not so strong as in the telescopic NW case. As discussed previously, the modified geometric constrains can explain this reduced difference of the FL and corrected solutions: (a) the area of the cross-section for the two nano-systems is different (100/165 nm^2 for the NWs, ~ 1000 nm^2 for the FIN, (b) the boundary with the substrate is made of the same material for the FIN, while of two different materials for the telescopic NW, and (c) only one side of the telescopic NW is in contact with the substrate, while the full FIN is in contact with its own substrate.

Our research shows that integrating phononic corrections into continuum heat transport models is a feasible technique for accurately simulating nanosystem heating processes. The technique replaces "ad hoc" geometric calibrations (such as size- and shape-dependent kapp(T) in the FL) with a more robust and universally applicable "material" calibration from experiment or theory. We studied the influence of a first-order phononic correction on 2D and 3D heating models. This adjust-

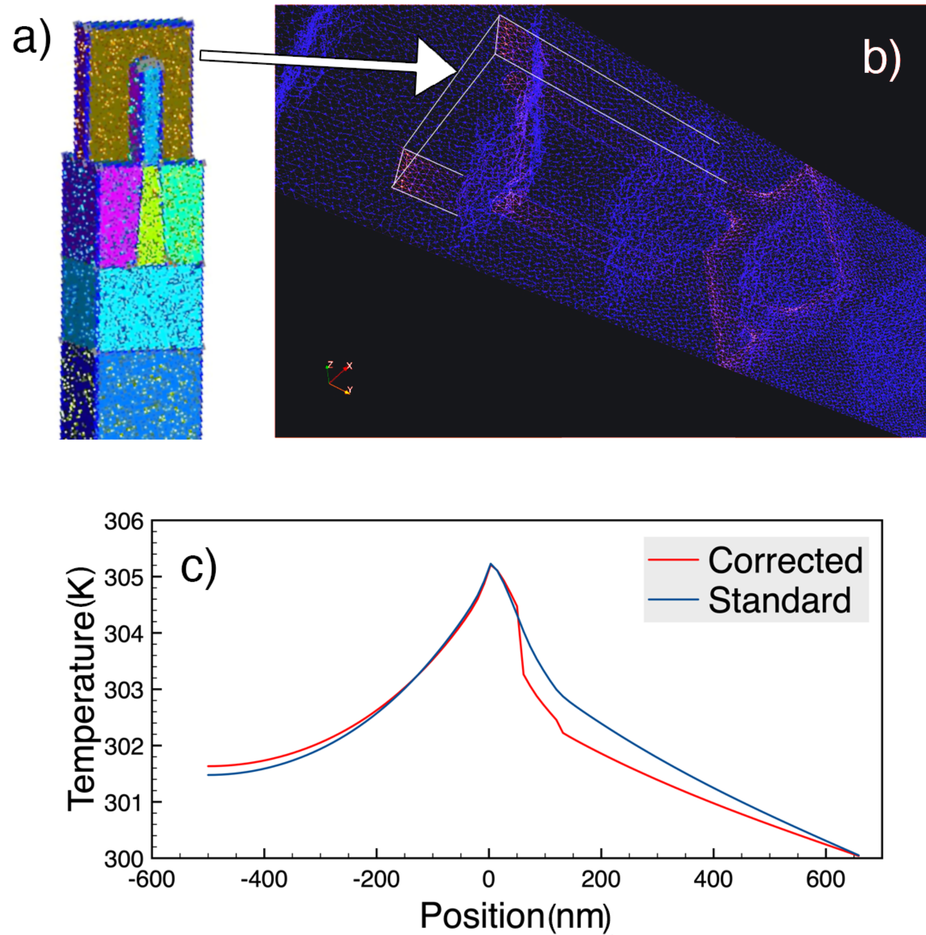

Figure 4.6: (a) CAD model and mesh of a Si-gated FinFET structure. : The colors differentiate the many elements required to construct the CAD geometry. (b) Heat source distribution mapped in the structure mesh used for FEM calculations. The arrow indicates equivalent regions in the panels (a) and (b). (c) Comparison of thermal profiles obtained after 5 ns of simulated LTA using standard and corrected BCs.

ment interpolates between diffusive and ballistic heat transfer by using the average phonon scattering length as the supplementary calibration parameter. Our numerical method yields positive results: adjustments are important at the nanoscale, and the solutions can restore the experimental environment. The current approach contains flaws due to the approximation of phononic energy transmission as a single scalar average field and the formulation of a single phonon scattering length. When working with anisotropic materials, where heat conductivity is governed by a large number of phonon modes, or amorphous or disordered systems, it may be necessary to generalize. Anisotropic materials use the tensor Fourier law. The current deduction involves a formalization of boundary relations. We implicitly assume that each phonon mode has the same average relaxation time. When the relaxation term is incorporated for frequency and polarization, the problem becomes BTE. The qualitative framework of the current (approximate) derivation may nevertheless be useful for disordered or amorphous materials or when heat transfer is unrelated to sound travel. [Cite] In this case, cannot be appropriately linked to the material's attributes; it's an ad hoc model parameter that must be well-fitted. Extra changes to bulk constitutive equations are possible, especially when atomically thin low-dimensional materials are considered. NEMD simulation was utilized to validate this method. This set-up may be used in molecular dynamics and continuum simulations to examine the thermal properties of nanoscaled silicon nanowires. With its help, empirical TCAD continuum models for nanoscaled electron devices may be built and calibrated. These models simulate nanoscaled electron devices.

Chapter 5

Simulations with complex dynamics: 2D explosive crystallization

The goal of this brief chapter is to demonstrate the initial effort put into stabilizing the algorithm with ultrafast phenomena such as Explosive Crystallization. In the first section, we explain what explosive crystallization is and what potential applications it has in today's industry, followed by a 1D simulation and then a 2D simulation that demonstrate our efforts to stabilize the code in several dimensions. However, as previously indicated, the work was placed on hold in favor of other tasks, but I'd like to share it as a starting point for future development of a completely 3d explosive workflow.

Explosive crystallization is a phenomenon that can occur during laser annealing, in which the material being heated rapidly transforms from an amorphous state into a crystalline state. This transformation can cause the material to expand violently, resulting in damage to the surrounding area. EC was first observed in the early 1970s during experiments on laser annealing of amorphous silicon. Since then, it has been observed in a variety of other materials, including germanium, silicon-germanium alloys, and chalcogenide glasses. While EC can be detrimental to the device being fabricated, it can also be exploited for certain applications.

For example, EC can be used to create nanoscale features or to modify the properties of a material.

EC is thought to occur when the rate of heating is high enough that the atoms in the material do not have time to rearrange themselves into a crystalline structure. Instead, they remain in an amorphous state until the temperature gets high enough that they suddenly transform into a crystal. This transformation can cause the material to expand rapidly, resulting in damage to the surrounding area. EC has been observed in a variety of materials, including germanium, silicon-germanium alloys, and chalcogenide glasses. While EC can be detrimental to the device being fabricated, it can also be exploited for certain applications. For example, EC can be used to create nanoscale features or to modify the properties of a material.

In the field of device technology, annealing techniques for amorphous materials are rather common, and in the vast majority of cases, the crystal phase is regained at the end of the operation. In the case of LA application, the procedure can readily deal with Explosive crystallization (EC) is a known mechanism in covalent elemental semiconductors (Si and Ge) and is characterized by a significantly greater (negative) latent heat for the liquid to crystal phase transition compared to the one (positive) for the amorphous to liquid phase transition (see, for example, Ref. [77] and references therein). Because the thermodynamic parameters of the three concurrent phases are out of balance, the model must recover the explosive kinetics of the process

Computer simulations of explosive crystallization are an essential tool for researchers studying this phenomenon. By modeling the behavior of materials under extreme conditions, scientists can gain a better understanding of how the phenomenon works and how to improve them. Additionally, computer simulations can help researchers design new materials that are less likely to experience explosive crystallization.

As computer technology continues to evolve, so too will the capabilities of explosive crystallization simulations. With each new generation of computers, scientists will be able to model the behavior of materials with greater accuracy and detail. Additionally, new simulation techniques and software programs will be developed that will allow researchers to investigate a wider range of materials and conditions. As computer simula-

tions become more sophisticated, they will continue to play a vital role in the study of explosive crystallization.

The quantitative modeling of the EC phenomenon should allow the computation of the contemporary kinetics of the crystal-liquid and liquid-amorphous front on the basis of the thermodynamic parameters of the substance in study. In ref. [74] the authors propose a new method for the tracking of the interface. The proposed formalism is a natural extension of the original phase field one and ensures an efficient computational way to solve a multiple phase problem. The new formulation exploits three local minima of the potential energy density at $-1, 0, 1$ (despite the two minima of the phase field Wheeler's formulation [1] discussed in the previous section) that represent, respectively, the amorphous, liquid and crystal phase. All the physical parameters (including the ones ruling the dopant evolution) in this approach must interpolate the calibrated values in the three phases. Here we report an example of one of the parameters of the model that clearly depends on temperature and phase

$$K(\phi, T) = \theta(\phi) K_c(T) + [1 - \theta(\phi)] K_a(T) + K_l(T) [1 - |\phi|] \tag{5.1}$$

where $\theta(\phi)$ is the Heaviside step function while the c, a, l subscripts indicate crystal, amorphous and liquid phases respectively.

An example of the solution of this three-phase model is reported in Fig. 5.1. The simulation refers to LA processes in samples with an $\tilde{3}5$ nm amorphous layer of Ge (α-Ge) laying on crystalline Ge (c-Ge). The amorphous layer is formed by Phosphours implantation at the energy of 15 keV up to the dose of 1×10^{15} cm^{-2}.

The initial phase variable (see Fig. 5.1)matches the initial phase distribution: The top layer of 35 nm is in the amorphous phase, with value $\phi = -1$ of the phase variable, upon a crystalline bulk up to 50 μm (the substrate thickness) with a value of 1 of ϕ. The initial temperature of the sample is set at the value of 300 K in the whole simulation box. The as-implanted P SIMS profile is also shown in Fig. 5.1 and is used for the initialization of the impurity density field in the LA simulations.

Fig. 5.1 shows snapshots of phase, temperature and dopant fields obtained in the simulation of LA at a fluence of 1.2 J/cm^2 for different times. The red curves with asterisks represent the temperature (scale on

the left side), the black curves with circle represent the phase (only 3 steps but no scale, the lower one is the amorphous, the liquid is in the middle and the upper one is the crystal phase); the blue curves with the rhombus represent the Phosporous distribution and the scale is on the right side. The upper right part of the figures shows the melting temperature of the amorphous phase (magenta line with squares) and the crystalline phase (green line with triangles). In Fig. 5.1 (a) the blue curve represents the as-implanted P SIMS profile.

Fig. 5.1 (a) shows the simulation results after t= 155 ns before the occurrence of the EC nucleation event, where it is possible to see the initial melting of the amorphous film on the surface. There is the liquid phase on the left side ($\phi = 0$), the amorphous one in the middle ($\phi = -1$) and the crystalline in the bulk ($\phi = 1$). The temperature exhibits the typical diffuse decay in the bulk and a plateau (at temperatures slightly larger than the melting point of α-Ge) close to the surface due to both the latent heat absorption and the presence of the liquid phase with its high thermal conductivity.

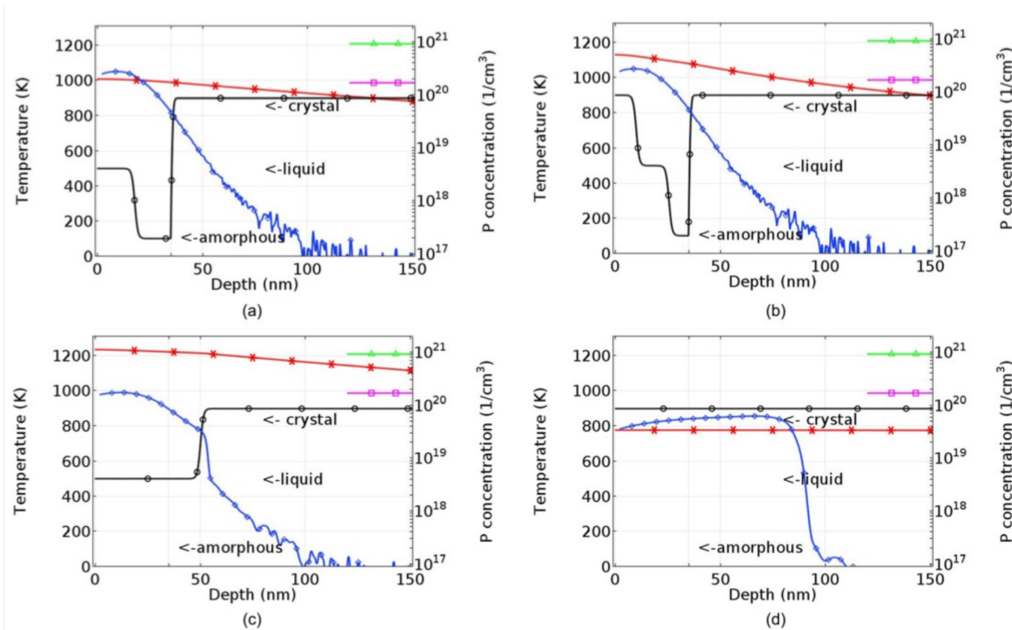

Figure 5.1: Multiple simulation snapshots taken at different times for the 1.2 J/cm^2 fluence case. The scale on the left is for temperature values (red solid line and asterisks), the scale on the right is for dopant density (blue solid line and rhombus), and a text description is provided for the phase (black solid line), which represents the three principal values of the phase field function. ϕ : -1, 0, and 1 corresponding to the amorphous, liquid, and crystalline phases, respectively. Indicated as well are the melting temperatures of the amorphous (magenta segment and squares) and crystalline phases (green segment and triangles). (a) Snapshot of the simulation at t = 155 ns (before the EC event). (b) Snapshot of the simulation at t = 156 ns (EC event). (c) Snapshot of the simulation at t = 210 ns (secondary melting). (d) Snapshot of the simulation at t = 500 ns (final state) [74]. From S. Lombardo et al. J. Appl. Phys. 123, 105105 (2018);

Fig. 5.1 (b) shows the simulation results after t= 156 ns during the EC event. In this situation the liquid phase is in an under-cooled and unstable state which then solidifies in the crystalline phase. The solidification releases the latent heat that heats up locally the sample (consider that the

solidification of the crystalline phase takes place at a higher temperature than the amorphous one). The heat released tends to melt the amorphous part and therefore the liquid/amorphous front moves to the bulk and is followed by the crystalline/amorphous front. From left to right the black curve (the phase) starts with value 1, i.e. the crystal phase, then it drops to 0, which is the cushion of the liquid phase (this layer is about 15 nm thick) and after the liquid layer the value -1 is reached for the remaining part of the amorphous phase. The last part of the phase function is the original crystalline bulk ($\phi = 1$).

The red curve represents the temperature of the specimen in this stage and it shows (from left to right): a significant higher value with respect to the melting point of α-Ge due to the solidification on the surface (i.e. the heat is released); a descending value in the liquid layer; a lower value close to the liquid amorphous/interface (where heat is absorbed) and beyond the amorphous/crystal interface due to the typical diffusion decay. The primary front activated by the EC consumes the amorphous film which is replaced by a nano-crystalline one at the end of the EC phenomenon after a very short time interval ($EC_{time} \sim 1$ ns).

The simulated evolution at t=210 is reproduced in Fig. 5.1 (c)). A secondary (two-phase) front starts to evolve as soon as the (poly)crystal surface reaches the c-Ge melting point and, for the particular irradiation conditions here considered, it reaches a melt depth beyond the original A/C interface.

Depending on the fluence values considered, different scenarios are possible, which we do not report here, but which can be found in full in ref. [74]. In this case, after the EC there is the re-melting of the newly formed crystalline layer, well beyond the initial amorphous crystalline interface.

Figure 5.1 (d) shows the simulation at t=500 ns when the evolution of the phase and dopant fields is practically quenched. Here the sample is fully crystalline ($\phi = 1$). The temperature, the red curve in the figure, shows a rather uniform value in the region of interest and it continues to decrease with time recovering the 300 K value after few tens of μs. One of the most notable achievements of the collaboration with LASSE was the development of a stabilization algorithm for 1D explosive crystallization, which was later expanded to include 2D and 3D crystallization. The

method is fairly similar to the one used for the implementation of the simple phase field, with the exception that we must deal with a double sigmoid instead of a single sigmoid, as is the case with the normal phase field implementation. In a limited 2D case set, the findings were promising; however, the algorithm failed when it was applied to 3D structures, demonstrating that careful selection of input parameters is required for successful results and that a more refined strategy is required to solve the 3D problem. Fig. 5.2 shows a 2D melting front driven by an ultrafast recrystallization in a simple Si slab with a 50 nm narrowing of the structure, in order to test the robustness of the solution with hard edges.

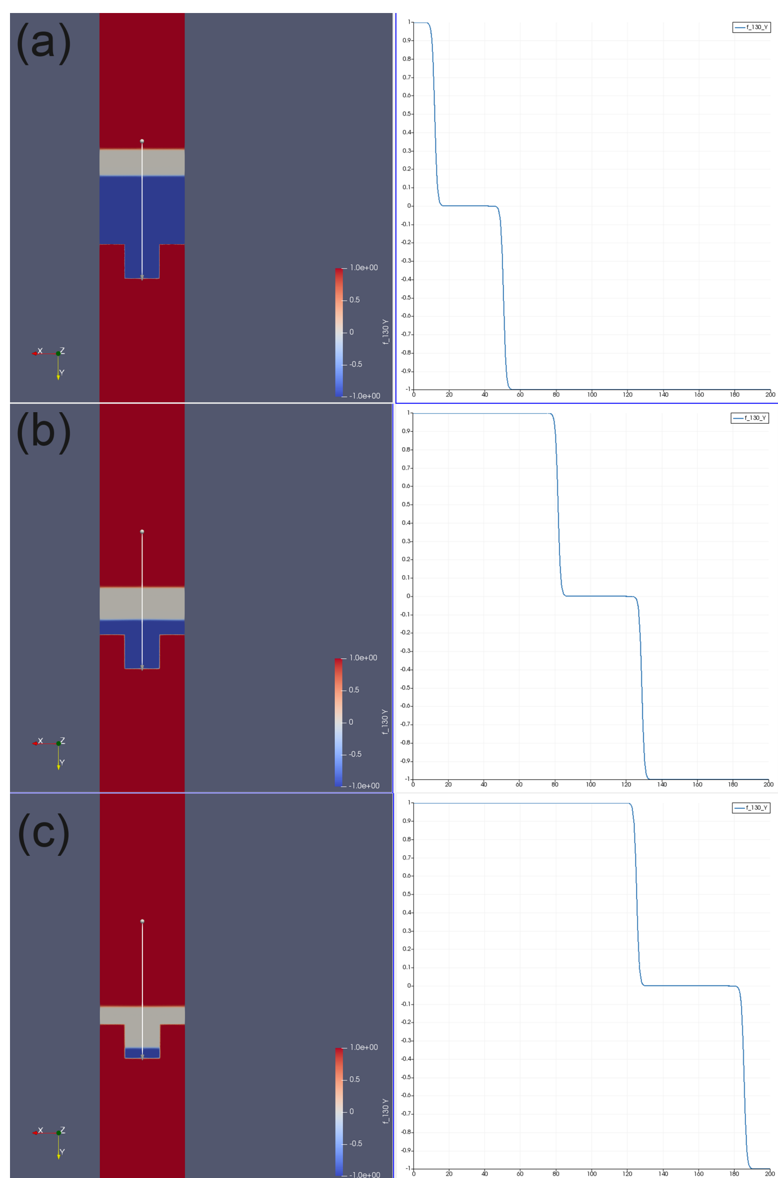

Figure 5.2: Snapshots of 2D explosive crystallization at (a) 78 ns (b) 84 ns and (c) 89 ns.The red, blue, and grey sections are respectively crystalline, amorphous, and liquid. The vertical line indicates the original thickness of the amorphous zone, while the red region at the top is filled with air. The structure's lateral dimension is 50 nm, and periodic boundary conditions are imposed along the x-axis.

In order to get a deeper degree of knowledge and command over increasingly complicated processes, it is vital to be able to evaluate ultrafast phenomena, especially when considering the behavior of alloys and the dispersion of dopants. For this purpose, we have developed a multi-well phase-field model adapted to the modeling of explosive crystallization caused by nanosecond-scale pulsed laser irradiation. This model was created specifically for this type of modeling. Despite the phenomena-caused sudden jumps in interface speed, the numerical implementation of the model remains resilient. Due to time restrictions and the fact that the code was refactored as a result of changes in task priority for the development of the code, we have not conducted too many simulations.

Chapter 6

Conclusions

Laser annealing is a vast topic to cover in detail, especially the simulation aspect, which can be difficult to tackle as a problem. I purposefully left out of the discussion a significant portion of the job, namely the coding itself. Working with an industrial partner has been a fantastic experience, and working with a commercially available program implies that its code must adhere to certain industry standards. A significant portion of these three years was devoted to refactoring the original code, which implies that a significant amount of effort was done on performance optimization and debugging with my colleagues at LASSE. This section of the discussion was left out since it is more appropriate for a thesis in software engineering. I only left some discussion on the implementation of the new features in the first chapter because it is significant to the entire narrative of the thesis. We can now summarize what we have seen in this thesis work.

We talked about how the code handles the interaction between the laser and the matter, taking into account the optical excitations of electrons in solids that are triggered by photons with energies of *sim*eV, as well as the inner interaction that leads to energy transfer from the electron system to the phonon bath (also known as thermalization). Following that, we spoke about the modeling of the LA processes that induce the crystal-liquid-crystal phase transitions. The primary emphasis of this conversation was on the computational difficulties of non-equilibrium impurity kinetics and activation. In the end, we talked about how the code

really works, as well as the changes between the code before and after I completed my PhD.

In the next chapter, we talked about the material calibration methodology for a completely self-consistent laser annealing simulation model that is integrated into the LIAB TCAD framework. The calibration strategy makes use of very simple structures, together with diffusion marker species and straightforward characterisation methods. It also makes use of an in-situ time-resolved metrology system. We have a good understanding of the primary material characteristics that need to be calibrated; they include the diffusion parameters (segregation, diffusion), as well as the optical properties. The approach was successfully applied to Ge and Si(1-x)Gex (where x = 0.2, 0.3, and 0.4), and a reasonable agreement was reached with the experimental results. Last but not least, the laser annealing of an advanced p-type finFET with SiGe contact regions was modeled as a typical 2D use case. This showed that process flow optimization together with an accurate control of laser annealing parameters is required in order to avoid unwanted melt-mediated diffusion effects.

Next, the findings of our research indicate that the integration of phononic corrections into continuum heat transport models is a workable strategy for achieving an accurate simulation of the heating processes that are associated with complex nanosystems. The purpose of the approach is to replace "ad hoc" geometric calibrations (for example, the use of the size- and shape-dependent kapp(T) in the FL) with a more robust and generally applicable "material" calibration that is obtained either from experiment or theory. Within the scope of this study, we investigated the effect that a first-order phononic correction has on simulations of heating carried out for a variety of 2D and 3D systems. This adjustment is able to interpolate between the diffusive and the ballistic regimes of heat transport by making use of the average scattering length for the phonons in the material as the single extra calibration parameter. The findings of our numerical technique are encouraging: the corrections are significant at the nanoscale, and when it is possible to make comparisons with experiments, the solutions are able to restore the same experimental setting. The present technique has certain shortcomings that can be traced back to the approximation of the phononic energy transfer in terms of a single scalar average field and the definition of a single phonon scattering length that

comes as a direct result of this. In situations where this approximation may be too precise, such as when dealing with anisotropic materials, in which the heat conductions are determined by a large number of phonon modes, or when dealing with amorphous or disordered systems, it may be essential to resort to more generalizations. The tensor version of the Fourier law is often utilized in anisotropic materials. Because of this, the framework of the current derivation requires a distinct formalization of the boundary relations. Because of the way we approach the problem, it is implicitly assumed that each phonon mode has the same average relaxation duration. The issue, of course, moves to the BTE level when the relaxation term is accurately included with regard to frequency and polarization. However, the qualitative framework of the current (approximate) derivation might still be relevant even for disordered or amorphous materials or, more generally, when heat transport is scarcely connected with the sound transport mechanism. [Citation needed] In this particular instance, cannot be correctly connected to the qualities of the material; rather, it should be thought of as an ad hoc model parameter that has to be well fitted. In conclusion, more improvements are feasible, such as extra adjustments to the bulk constitutive equations, particularly when atomically thin low-dimensional materials are taken into consideration. For the purpose of validating this approach, a NEMD simulation set-up was used. This set-up is suitable for the assessment of the thermal characteristics of nanoscaled silicon nanowires and may be utilized equivalently in molecular dynamics simulations as well as continuum simulations. It is feasible, with its assistance, to offer necessary data for the construction and calibration of empirical TCAD continuum models that are suited for nanoscaled electron devices. These models may be used to simulate the behavior of nanoscaled electron devices. Explosive crystallization was the last essential component that we included into the programming for our simulation. The ability to analyze this ultrafast phenomena is essential to achieving a deeper level of comprehension and command over more complex processes, in particular when taking into consideration the behavior of alloys and the dispersion of dopants. For this reason, we have constructed a multi-well phase-field model that is tailored to the simulation of explosive crystallization generated by pulsed laser irradiation on the nanosecond time scale. This model is especially designed to accom-

modate this kind of modeling. Despite the abrupt jumps in the interface speed that are caused by the phenomena, the numerical implementation of the model is resilient. On the other hand, since the code was refactored as a result of certain changes in task priority for the code's development, we haven't run too many simulations owing to the fact that we have time constraints.

The LIAB program is currently in a stable state; however, numerous improvements could be made, particularly in the explosive component, which could be further stabilized in 2D and expanded in 3D. In terms of future perspectives, during the past several months, we have been working on a new multiscale technique that simulates a heating scenario at a "wafer-scale" and uses that heatsource to calculate heat and phase distribution at the nanoscale. But LIAB is not only a fully enclosed piece of software; we also built it to be very modular, to be a collection of tools that can be used for independent computations or as a multiphysics platform for Laser Thermal annealing Simulations. This was our goal when we set out to build it and now it's EM and Heating modules are used efficently in the latest project based on the parallel coupling of a continuum, finite elements, μm-scale electromagnetic-thermal solver with a super-lattice Kinetic Monte Carlo atomistic model for melting [78].

Chapter 7

Parameters

In this chapter we present various tables with all the physical paramenters present in the LIAB materials database for the different materials used in our simulations.

Silicon

The material database needed for laser annealing of Silicon substrates is reliable for the solid and the liquid phase due to the large number of investigations dealing with the LA process of Silicon (see table 1). For this material all three phases (i.e. c-Si, l-Si and a-Si) have to be considered. Amorphous phase parameters in the literature have a natural spread due to the possible dependence of physical parameters on the a-phase preparation (e.g. implantation, deposition etc). Anyhow, a preliminary parameter set will be presented as a basis of the joint simulation and experimental work foreseen in T4.2. Direct optical measurements for the a-Si case will be performed only if the validation activity in T4.2 will show discrepancies between simulation predictions and process characterizations. In the three tables below, we report the calibration assessment derived from the literature for the Si-related parameters in the three phases, respectively. Reference literature papers are indicated. We notice that some of these papers refer to a list of previous works where direct measurements are discussed.

Crystal Si			
Symbol [units]	Description	Expression	Ref.
ρ $[Kg/m^3]$	Density	2320	[2]
T_M $[K]$	Melting Temperature	1688	[79]
C $[J/KgK]$	Thermal Capacitance	$10 * T^{-1.034}/(1.02 + 0.01 * T) - 213$	[79]
k $[W/mK]$	Thermal Conductivity	$100 * ((1523.7 * T^{-1.226}) * (T \leq 1200) + (1523.7 * T^{-0.502}) * (T \geq 1200)$	[2]
L $[J/m^3]$	Latent heat	1797000	[2]
ϵ_r	Real Permittivity	11.87	[2]
ϵ_i	Imaginary Permittivity	37.96	[2]
A $[m/s]$	Speed pre-factor	1000	[2]
E_a $[m/s]$	Activation Energy	Range in 0.42-0.45	[2, 57]
N $[at/m^3]$	Atomic Density	4.995E+28	[2]

Liquid Si			
Symbol [units]	Description	Expression	Ref.
ρ $[Kg/m^3]$	Density	2520	[2]
C $[J/KgK]$	Thermal Capacitance	1045	[79]
k $[W/mK]$	Thermal Conductivity	$100 * [0.0502 + 0.000293 * (T - T_M)]$	[2]
ϵ_r	Real Permittivity	-15.734	[2]
ϵ_i	Imaginary Permittivity	10.126	[2]

Amorphous Si			
Symbol [units]	Description	Expression	Ref.
ρ $[Kg/m^3]$	Density	2100	[79]
T_M $[K]$	Melting Temperature	1420	[2]
C $[J/KgK]$	Thermal Capacitance	$10 * T^{-1.034}/(1.02 + 0.01 * T) - 213$	[79]
k $[W/mK]$	Thermal Conductivity	1.8	[2]
L $[J/m^3]$	Latent heat	1317000	[2]
ϵ_r	Real Permittivity	0.333	[2]
ϵ_i	Imaginary Permittivity	21.11	[2]
A $[m/s]$	Speed pre-factor	1000	[2]
E_a $[m/s]$	Activation Energy	0.32	[2]
N $[at/m^3]$	Atomic Density	Range in 4.9-4.995E+28	[80, 2]

We note that a heating problem which considers also melting phenomena requires the parameters appearing in the Fourier law (density, thermal capacitance and conductivity, latent heat) as well as a law of the temperature dependence for the solid-liquid interface speed $v(T)$. A Fulcher-Vogel law (5; 6) is usually assumed, which reads:

$$v(T) = Aexp(E_a/K_bT) * exp\{1 - exp[(/k_bN)(1/T_M - 1/T)]\}$$

Where k_b is the Boltzmann constant.

Germanium

Likewise silicon, the model calibration for germanium is reliable for the solid and the liquid phase, while it has a less stable parameter setting for the amorphous phase.

Crystal Ge			
Symbol [units]	Description	Expression	Ref.
ρ $[Kg/m^3]$	Density	5320	[74]
T_M $[K]$	Melting Temperature	1210	[74]
C $[J/KgK]$	Thermal Capacitance	$1000 * (0.000117 * T + 0.293)$	[74]
k $[W/mK]$	Thermal Conductivity	$60.2 * (T/300)^{-1.25}$	[74]
L $[J/m^3]$	Latent heat	465000	[74]
ϵ_r	Real Permittivity	$3.192E-06T^2 - 1.355 * T + 8.841$	[57]
ϵ_i	Imaginary Permittivity	$-5.2235E-06T^2 + 1.593 * T + 23.571$	[57]
A $[m/s]$	Speed pre-factor	0.3E+04	[74]
E_a $[m/s]$	Activation Energy	0.5	[74]
N $[at/m^3]$	Atomic Density	4.565E+28	[74]

Liquid Ge			
Symbol [units]	Description	Expression	Ref.
ρ $[Kg/m^3]$	Density	$1000 * (5.6 - 0.000625 * (T - 1210))$	[81]
C $[J/KgK]$	Thermal Capacitance	460	[74]
k $[W/mK]$	Thermal Conductivity	29.7	[74]
ϵ_r	Real Permittivity	-16.225	[74]
ϵ_i	Imaginary Permittivity	9.993	[74]

Amorphous Ge			
Symbol [units]	Description	Expression	Ref.
ρ $[Kg/m^3]$	Density	5320	[74]
T_M $[K]$	Melting Temperature	987	[74]
C $[J/KgK]$	Thermal Capacitance	$1000 * (0.000172 * T + 0.2899)$	[74]
k $[W/mK]$	Thermal Conductivity	2.5	[74]
L $[J/m^3]$	Latent heat	350000	[74]
ϵ_r	Real Permittivity	-2.811	[74]
ϵ_i	Imaginary Permittivity	15.606	[74]
A $[m/s]$	Speed pre-factor	0.3E+04	[74]
E_a $[m/s]$	Activation Energy	0.5	[74]
N $[at/m^3]$	Atomic Density	4.12E+28	[74]

SiGe

SiGe is a nearly perfect binary alloy system: Si and Ge are completely miscible across the whole composition range. Because of this, the linear interpolation of the physical properties of Si and Ge (using the alloy fraction variable X) provides a reasonable starting point for the calibration of this material. However, there are several crucial uncertainties. A more precise determination of the optical parameters' dependency on X in each phase is required. Furthermore, direct measurements are insufficient to determine the dependency of the parameters in the disordered phases (liquid and amorphous) on X: The standard technique is to em-

ploy the same relations as for the crystal phase. All of the parameters are expressed in the tables as:

$$P_{SiGe}(T, X) = P_{Ge}(T) \times f_P^n(X) + P_{Si}(T) \times [1 - f_P^n(X)]$$

where $f_P^n(X)$ is monotonically growing polynomial function of degree n satisfying the obvious relationships $f_P(0) = 0$, $f_P(1) = 1$ while $P_{Ge}(T)$ and $P_{Si}(T)$ are the Ge and Si parameters reported in the previous sections. Therefore, only$f_P^n(X)$ will be reported. In the case of linear interpolation we have:

$$f_P^n(X) = f_P^1(X) = X$$

The phase field model effectively obtains the quadratic dependency of the solidus and liquidus curves, by combining the linear dependence of the melting temperature TM on X and the segregation effect for X at the liquid-solid interface.

Crystal SiGe			
Symbol [units]	Description	$f_P^n(X)$	Ref.
ρ $[Kg/m^3]$	Density	$1.2143 \times X - 0.2143 \times X^2$	[74]
T_M $[K]$	Melting Temperature	X	[74]
C $[J/KgK]$	Thermal Capacitance	X	[74]
k $[W/mK]$	Thermal Conductivity	X	[74]
L $[J/m^3]$	Latent heat	X	[74]
ϵ_r	Real Permittivity	$1.023 \times X - 0.023 \times X^2$	[57]
ϵ_i	Imaginary Permittivity	$1.469 \times X - 0.469 \times X^2$	[57]
A $[m/s]$	Speed pre-factor	X	[74]
E_a $[m/s]$	Activation Energy	X	[74]
N $[at/m^3]$	Atomic Density	X	[74]

Liquid SiGe			
Symbol [units]	Description	$f_P^n(X)$	Ref.
ρ $[Kg/m^3]$	Density	$1.2143 \times X - 0.2143 \times X^2$	[81]
C $[J/KgK]$	Thermal Capacitance	X	[74]
k $[W/mK]$	Thermal Conductivity	X	[74]
ϵ_r	Real Permittivity	$1.023 \times X - 0.023 \times X^2$	[74]
ϵ_i	Imaginary Permittivity	$1.469 \times X - 0.469 \times X^2$	[74]

Amorphous SiGe			
Symbol [units]	Description	$f_P^n(X)$	Ref.
ρ $[Kg/m^3]$	Density	$1.2143 \times X - 0.2143 \times X^2$	[74]
T_M $[K]$	Melting Temperature	X	[74]
C $[J/KgK]$	Thermal Capacitance	X	[74]
k $[W/mK]$	Thermal Conductivity	X	[74]
L $[J/m^3]$	Latent heat	X	[74]
ϵ_r	Real Permittivity	$1.023 \times X - 0.023 \times X^2$	[57]
ϵ_i	Imaginary Permittivity	$1.469 \times X - 0.469 \times X^2$	[57]
A $[m/s]$	Speed pre-factor	X	[74]
E_a $[m/s]$	Activation Energy	X	[74]
N $[at/m^3]$	Atomic Density	X	[74]

SiO2

For the SiO2 material, first order phase transitions (i.e. latent heat absorption/release) do not occur. T_M is presented here as the glass transition temperature because it may be of relevance when analyzing the simulated temperature map. The thermal parameters' dependence on T is consistent. There is no need for direct optical measurements, and the constant values presented here are adequate approximations for the early calibration set.

Amorphous SiO2			
Symbol [units]	Description	Expression	Ref.
ρ $[Kg/m^3]$	Density	2203	[2]
T_M $[K]$	Glass Transition Temperature	1986	[2]
C $[J/KgK]$	Thermal Capacitance	$1000 \times (0.604 + 5.188E - 04 \times T)$	[2]
k $[W/mK]$	Thermal Conductivity	$100 \times ((1.005E - 02 + 1.005E - 05T) \times (T$ł$1170) + (2.512E - 02) \times (T \geq 1170))$	[2]
ϵ_r	Real Permittivity	2.245	[57]
ϵ_i	Imaginary Permittivity	0.00036	[2]

Bibliography

[1] A. A. Wheeler, W. J. Boettinger, and G. B. McFadden, "Phase-field model for isothermal phase transitions in binary alloys," *Phys. Rev. A*, vol. 45, pp. 7424–7439, May 1992.

[2] A. La Magna, P. Alippi, V. Privitera, G. Fortunato, M. Camalleri, and B. Svensson, "A phase-field approach to the simulation of the excimer laser annealing process in si," *Journal of Applied Physics*, vol. 95, no. 9, pp. 4806–4814, 2004.

[3] A. La Magna, P. Alippi, V. Privitera, and G. Fortunato, "Role of light scattering in excimer laser annealing of si," *Applied Physics Letters*, vol. 86, no. 16, 2005.

[4] G. Fisicaro, K. Huet, R. Negru, M. Hackenberg, P. Pichler, N. Taleb, and A. La Magna, "Anomalous impurity segregation and local bonding fluctuation in *l*-si," *Phys. Rev. Lett.*, vol. 110, p. 117801, Mar 2013.

[5] G. Impellizzeri, E. Napolitani, S. Boninelli, G. Fisicaro, M. Cuscunà, R. Milazzo, A. L. Magna, G. Fortunato, F. Priolo, and V. Privitera, "B-doping in ge by excimer laser annealing," *Journal of Applied Physics*, vol. 113, no. 11, 2013.

[6] E. Bruno, G. G. Scapellato, A. La Magna, M. Cuscunà, E. Napolitani, S. Boninelli, F. Priolo, G. Fortunato, and V. Privitera, "Anomalous transport of sb in laser irradiated ge," *Applied Physics Letters*, vol. 101, no. 17, 2012.

[7] R. Milazzo, E. Napolitani, G. Impellizzeri, G. Fisicaro, S. Boninelli, M. Cuscunà, D. De Salvador, M. Mastromatteo, M. Italia, A. La Magna, G. Fortunato, F. Priolo, V. Privitera, and A. Carnera, "N-type doping of ge by as implantation and excimer laser annealing," *Journal of Applied Physics*, vol. 115, no. 5, 2014.

[8] K. Huet, G. Fisicaro, J. Venturini, H. Besaucèle, and A. La Magna, "Defect kinetics and dopant activation in submicrosecond laser thermal processes," *Applied Physics Letters*, vol. 95, no. 23, 2009.

[9] G. Fisicaro, A. L. Magna, G. Piccitto, and V. Privitera, "Laser annealing of sige and ge based devices," *Microelectronic Engineering*, vol. 88, no. 4, pp. 488 – 491, 2011. Post-Si-CMOS electronic devices: the role of Ge and III-V materials.

[10] G. Fisicaro, L. Pelaz, M. Aboy, P. Lopez, M. Italia, K. Huet, F. Cristiano, Z. Essa, Q. Yang, E. Bedel-Pereira, M. Quillec, and A. L. Magna, "Kinetic monte carlo simulations of boron activation in implanted si under laser thermal annealing," *Applied Physics Express*, vol. 7, no. 2, p. 021301, 2014.

[11] G. Fisicaro, L. Pelaz, P. Lopez, and A. La Magna, "Kinetic monte carlo simulations for transient thermal fields: Computational methodology and application to the submicrosecond laser processes in implanted silicon," *Phys. Rev. E*, vol. 86, p. 036705, Sep 2012.

[12] G. Fisicaro and A. La Magna, "Modeling of laser annealing," *Journal of Computational Electronics*, vol. 13, no. 1, pp. 70–94, 2014.

[13] R. Milazzo, G. Impellizzeri, D. Piccinotti, A. La Magna, G. Fortunato, D. De Salvador, A. Carnera, A. Portavoce, D. Mangelinck, V. Privitera, and E. Napolitani, "Impurity and defect interactions during laser thermal annealing in ge," *Journal of Applied Physics*, vol. 119, no. 4, 2016.

[14] F. Cristiano, M. Shayesteh, R. Duffy, K. Huet, F. Mazzamuto, Y. Qiu, M. Quillec, H. Henrichsen, P. Nielsen, D. Petersen, A. L. Magna, G. Caruso, and S. Boninelli, "Defect evolution and dopant activation in laser annealed si and ge," *Materials Science in Semiconductor*

Processing, vol. 42, Part 2, pp. 188 – 195, 2016. E-MRS Spring Meeting 2015 Symposium Z: Nanomaterials and processes for advanced semiconductor {CMOS} devices.

[15] Y. Qiu, F. Cristiano, K. Huet, F. Mazzamuto, G. Fisicaro, A. L. Magna, M. Quillec, N. Cherkashin, H. Wang, S. Duguay, and D. Blavette, "Extended defects formation in nanosecond laser-annealed ion implanted silicon," *Nano Letters*, vol. 14, no. 4, pp. 1769–1775, 2014. PMID: 24588318.

[16] B. Yu, Y. Wang, H. Wang, Q. Xiang, C. Riccobene, S. Talwar, and M.-R. Lin, "70 nm MOSFET with ultra-shallow, abrupt, and superdoped s/d extension implemented by laser thermal process (LTP)," in *International Electron Devices Meeting 1999. Technical Digest (Cat. No.99CH36318)*, IEEE.

[17] S. Talwar, S. Felch, D. Downey, and Y. Wang, "Study of laser thermal processing (LTP) to meet sub 130 nm node shallow junction requirements," in *2000 International Conference on Ion Implantation Technology Proceedings. Ion Implantation Technology - 2000 (Cat. No.00EX432)*, IEEE.

[18] K. Goto, T. Yamamoto, T. Kubo, M. Kase, Y. Wang, T. Lin, S. Talwar, and T. Sugii, "Ultra-low contact resistance for deca-nm MOSFETs by laser annealing," in *International Electron Devices Meeting 1999. Technical Digest (Cat. No.99CH36318)*, IEEE, 1999.

[19] K. Pey and P. Lee, "Pulsed laser annealing technology for nanoscale fabrication of silicon-based devices in semiconductors," in *Advances in Laser Materials Processing*, pp. 327–364, Elsevier, 2010.

[20] S.-D. Kim, C.-M. Park, and J. Woo, "Advanced source/drain engineering for box-shaped ultrashallow junction formation using laser annealing and pre-amorphization implantation in sub-100-nm SOI CMOS," *IEEE Transactions on Electron Devices*, vol. 49, pp. 1748–1754, Oct. 2002.

[21] A. Shima, H. Ashihara, T. Mine, Y. Goto, M. Horiuchi, Y. Wang, S. Talwar, and A. Hiraiwa, "Self-limiting laser thermal process for

ultra-shallow junction formation of 50-nm gate CMOS," in *IEEE International Electron Devices Meeting 2003*, IEEE.

[22] A. Shima, H. Ashihara, A. Hiraiwa, T. Mine, and Y. Goto, "Ultra-shallow junction formation by self-limiting LTP and its application to sub-65-nm node MOSFETs," *IEEE Transactions on Electron Devices*, vol. 52, pp. 1165–1171, June 2005.

[23] A. Shima, T. Mine, K. Torii, and A. Hiraiwa, "Enhancement of drain current in planar MOSFETs by dopant profile engineering using non-melt laser spike annealing," *IEEE Transactions on Electron Devices*, vol. 54, pp. 2953–2959, Nov. 2007.

[24] T. Yamamoto, T. Kubo, T. Sukegawa, K. Hashimoto, and M. Kase, "Advanced junction profile engineering featuring laser spike annealing and co-implantation for sub-30-nm strained CMOS devices," in *2006 Symposium on VLSI Technology, 2006. Digest of Technical Papers.*, IEEE.

[25] T. Yamamoto, T. Kubo, T. Sukegawa, E. Takii, Y. Shimamune, N. Tamura, T. Sakoda, M. Nakamura, H. Ohta, T. Miyashita, H. Kurata, S. Satoh, M. Kase, and T. Sugii, "Junction profile engineering with a novel multiple laser spike annealing scheme for 45-nm node high performance and low leakage CMOS technology," in *2007 IEEE International Electron Devices Meeting*, IEEE, Dec. 2007.

[26] V. Privitera, A. L. Magna, C. Spinella, G. Fortunato, L. Mariucci, M. Cuscuna, C. M. Camalleri, A. Magri, G. L. Rosa, B. G. Svensson, E. V. Monakhov, and F. Simon, "Integration of melting excimer laser annealing in power MOS technology," *IEEE Transactions on Electron Devices*, vol. 54, pp. 852–860, Apr. 2007.

[27] G. Fortunato, L. Mariucci, M. Cuscunà, V. Privitera, A. L. Magna, C. Spinella, A. Magrì, M. Camalleri, D. Salinas, F. Simon, B. Svensson, and E. Monakhov, "Bragg reflector based gate stack architecture for process integration of excimer laser annealing," *Applied Physics Letters*, vol. 89, p. 253502, Dec. 2006.

[28] V. Gonda, A. Burtsev, T. Scholtes, and L. Nanver, "Near-ideal implanted shallow-junction diode formation by excimer laser annealing," in *2005 13th International Conference on Advanced Thermal Processing of Semiconductors*, IEEE.

[29] L. K. Nanver, H. Schellevis, T. L. M. Scholtes, L. L. Spina, G. Lorito, F. Sarubbi, V. Gonda, M. Popadic, K. Buisman, L. C. N. de Vreede, C. Huang, S. Milosavljevic, and E. J. G. Goudena, "Improved RF devices for future adaptive wireless systems using two-sided contacting and AlN cooling," *IEEE Journal of Solid-State Circuits*, vol. 44, pp. 2322–2338, Sept. 2009.

[30] D. von der Linde, K. Sokolowski-Tinten, and J. Bialkowski, "Laser–solid interaction in the femtosecond time regime," *Applied Surface Science*, vol. 109-110, pp. 1–10, Feb. 1997.

[31] A. Hu, Y. Zhou, and W. W. Duley, "Femtosecond laser-induced nanowelding: Fundamentals and applications," *The Open Surface Science Journal*, vol. 3, pp. 42–49, Jan. 2010.

[32] N. Buecking, M. Scheffler, P. Kratzer, and A. Knorr, "Theory of optical excitation and relaxation phenomena at semiconductor surfaces: linking density functional and density matrix theory," *Applied Physics A*, vol. 88, pp. 505–518, June 2007.

[33] G. Onida, L. Reining, and A. Rubio, "Electronic excitations: density-functional versus many-body green's-function approaches," *Rev. Mod. Phys.*, vol. 74, pp. 601–659, Jun 2002.

[34] M. Reichelt, T. Meier, S. W. Koch, and M. Rohlfing, "Theory for the nonlinear optical response of semiconductor surfaces: Application to the optical stark effect and spectral oscillations of the si(111)-(2×1) surface exciton," *Phys. Rev. B*, vol. 68, p. 045330, Jul 2003.

[35] B. K. S.I. Anisimov and T. Perel'man, "Electron emission from metal surfaces exposed to ultrashort laser pulses," *JETP*, vol. 39, p. 375, Aug 1974.

[36] L. T. M.I. Kaganov, I.M. Lifshitz, "Relaxation between electrons and the crystalline lattice," *JETP*, vol. 4, p. 173, Feb 1957.

[37] S. Lombardo, G. Fisicaro, I. Deretzis, A. L. Magna, B. Curver, B. Lespinasse, and K. Huet, "Theoretical study of the laser annealing process in FinFET structures," *Applied Surface Science*, vol. 467-468, pp. 666–672, Feb. 2019.

[38] Y.-Y. Z. Luigi Bonati and M. Par-rinello *Proceedings of the National Academy of Science*, vol. 116, no. 36, p. 17641, 2019.

[39] S. F. Lombardo, *Coupled Kinetic and Electromagnetic approaches for the simulation of complex processes*. PhD thesis, 03 2018.

[40] A. Karma and W.-J. Rappel, "Quantitative phase-field modeling of dendritic growth in two and three dimensions," *Phys. Rev. E*, vol. 57, pp. 4323–4349, Apr 1998.

[41] S. Lombardo, S. Boninelli, F. Cristiano, G. Fisicaro, G. Fortunato, M. Grimaldi, G. Impellizzeri, M. Italia, A. Marino, R. Milazzo, E. Napolitani, V. Privitera, and A. La Magna, "Laser annealing in si and ge: Anomalous physical aspects and modeling approaches," *Materials Science in Semiconductor Processing*, vol. 62, pp. 80 – 91, 2017. Advanced doping methods in semiconductor devices and nanostructures.

[42] M. Hackenberg, K. Huet, R. Negru, J. Venturini, G. Fisicaro, A. La Magna, and P. Pichler, "Modeling boron profiles in silicon after pulsed excimer laser annealing," *AIP Conf. Proc.*, vol. 1496, no. 1, pp. 241–244, 2012.

[43] A. B. Tayler, "Free and moving boundary problems. by j. crank. clarendon, oxford, 1984. 425 pp.," *Journal of Fluid Mechanics*, vol. 158, p. 532–533, 1985.

[44] N. A. Ahmad, A. A. Wheeler, W. J. Boettinger, and G. B. McFadden, "Solute trapping and solute drag in a phase-field model of rapid solidification," *Phys. Rev. E*, vol. 58, pp. 3436–3450, Sep 1998.

[45] E. V. Monakhov, B. G. Svensson, M. K. Linnarsson, A. La Magna, M. Italia, V. Privitera, G. Fortunato, M. Cuscunà, and L. Mariucci, "The effect of excimer laser pretreatment on diffusion and activation of boron implanted in silicon," *Applied Physics Letters*, vol. 87, no. 19, 2005.

[46] K. K. Ong, K. L. Pey, P. S. Lee, A. T. S. Wee, X. C. Wang, and Y. F. Chong, "Dopant distribution in the recrystallization transient at the maximum melt depth induced by laser annealing," *Applied Physics Letters*, vol. 89, no. 17, 2006.

[47] I. Štich, R. Car, and M. Parrinello, "Bonding and disorder in liquid silicon," *Phys. Rev. Lett.*, vol. 63, pp. 2240–2243, Nov 1989.

[48] J. T. Okada, P. H.-L. Sit, Y. Watanabe, Y. J. Wang, B. Barbiellini, T. Ishikawa, M. Itou, Y. Sakurai, A. Bansil, R. Ishikawa, M. Hamaishi, T. Masaki, P.-F. Paradis, K. Kimura, T. Ishikawa, and S. Nanao, "Persistence of covalent bonding in liquid silicon probed by inelastic x-ray scattering," *Phys. Rev. Lett.*, vol. 108, p. 067402, Feb 2012.

[49] N. Jakse and A. Pasturel, "Dynamics of liquid and undercooled silicon: An ab initio molecular dynamics study," *Phys. Rev. B*, vol. 79, p. 144206, 04 2009.

[50] P. M. Fahey, P. B. Griffin, and J. D. Plummer, "Point defects and dopant diffusion in silicon," *Rev. Mod. Phys.*, vol. 61, pp. 289–384, Apr 1989.

[51] G. Fisicaro, L. Pelaz, M. Aboy, P. Lopez, M. Italia, K. Huet, F. Cristiano, Z. Essa, Q. Yang, E. Bedel-Pereira, M. Quillec, and A. L. Magna, "Kinetic monte carlo simulations of boron activation in implanted si under laser thermal annealing," *Applied Physics Express*, vol. 7, no. 2, p. 021301, 2014.

[52] G. Fisicaro, M. Italia, V. Privitera, G. Piccitto, K. Huet, J. Venturini, and A. La Magna, "Solid phase phosphorous activation in implanted silicon by excimer laser irradiation," *Journal of Applied Physics*, vol. 109, no. 11, p. 113513, 2011.

[53] T. Ghani, M. Armstrong, C. Auth, M. Bost, P. Charvat, G. Glass, T. Hoffmann, K. Johnson, C. Kenyon, J. Klaus, B. McIntyre, K. Mistry, A. Murthy, J. Sandford, M. Silberstein, S. Sivakumar, P. Smith, K. Zawadzki, S. Thompson, and M. Bohr, "A 90nm high volume manufacturing logic technology featuring novel 45nm gate length strained silicon CMOS transistors," in *IEEE International Electron Devices Meeting 2003*, IEEE.

[54] K. Mistry, R. Chau, C.-H. Choi, G. Ding, K. Fischer, T. Ghani, R. Grover, W. Han, D. Hanken, M. Hattendorf, J. He, C. Allen, J. Hicks, R. Huessner, D. Ingerly, P. Jain, R. James, L. Jong, S. Joshi, C. Kenyon, K. Kuhn, K. Lee, C. Auth, H. Liu, J. Maiz, B. McIntyre, P. Moon, J. Neirynck, S. Pae, C. Parker, D. Parsons, C. Prasad, L. Pipes, B. Beattie, M. Prince, P. Ranade, T. Reynolds, J. Sandford, L. Shifren, J. Sebastian, J. Seiple, D. Simon, S. Sivakumar, P. Smith, D. Bergstrom, C. Thomas, T. Troeger, P. Vandervoorn, S. Williams, K. Zawadzki, M. Bost, M. Brazier, M. Buehler, and A. Cappellani, "A 45nm logic technology with high-kmetal gate transistors, strained silicon, 9 cu interconnect layers, 193nm dry patterning, and 100% pb-free packaging," in *2007 IEEE International Electron Devices Meeting*, IEEE, Dec. 2007.

[55] W.-H. Lee, A. Waite, H. Nii, H. Nayfeh, V. McGahay, H. Nakayama, D. Fried, H. Chen, L. Black, R. Bolam, J. Cheng, D. Chidambarrao, C. Christiansen, M. Cullinan-Scholl, D. Davies, A. Domenicucci, P. Fisher, J. Fitzsimmons, J. Gill, M. Gribelyuk, D. Harmon, J. Holt, K. Ida, M. Kiene, J. Kluth, C. Labelle, A. Madan, K. Malone, P. McLaughlin, M. Minami, D. Mocuta, R. Murphy, C. Muzzy, M. Newport, S. Panda, I. Peidous, A. Sakamoto, T. Sato, G. Sudo, H. VanMeer, T. Yamashita, H. Zhu, P. Agnello, G. Bronner, G. Freeman, S. Huang, T. Ivers, S. Luning, K. Miyamoto, H. Nye, J. Pellerin, K. Rim, D. Schepis, T. Spooner, X. Chen, and M. Khare, "High performance 65 nm SOI technology with enhanced transistor strain and advanced-low-k BEOL," in *IEEE InternationalElectron Devices Meeting, 2005. IEDM Technical Digest.*, IEEE.

[56] W. Haensch, E. J. Nowak, R. H. Dennard, P. M. Solomon, A. Bryant,

O. H. Dokumaci, A. Kumar, X. Wang, J. B. Johnson, and M. V. Fischetti, "Silicon CMOS devices beyond scaling," *IBM Journal of Research and Development*, vol. 50, pp. 339–361, July 2006.

[57] K. Huet, J. Aubin, P.-E. Raynal, B. Curvers, A. Verstraete, B. Lespinasse, F. Mazzamuto, A. Sciuto, S. Lombardo, A. La Magna, P. Acosta-Alba, L. Dagault, C. Licitra, J.-M. Hartmann, and S. Kerdilés, "Pulsed laser annealing for advanced technology nodes: Modeling and calibration," *Applied Surface Science*, vol. 505, p. 144470, 2020.

[58] T. Fühner, T. Schnattinger, G. Ardelean, and A. Erdmann, "Dr.LiTHO: a development and research lithography simulator," in *Optical Microlithography XX* (D. G. Flagello, ed.), SPIE, Mar. 2007.

[59] M. Hackenberg, K. Huet, R. Negru, J. Venturini, G. Fisicaro, A. L. Magna, and P. Pichler, "Modeling boron profiles in silicon after pulsed excimer laser annealing," in *AIP Conference Proceedings*, AIP, 2012.

[60] S. Lombardo, S. Boninelli, F. Cristiano, G. Fisicaro, G. Fortunato, M. Grimaldi, G. Impellizzeri, M. Italia, A. Marino, R. Milazzo, E. Napolitani, V. Privitera, and A. L. Magna, "Laser annealing in si and ge: Anomalous physical aspects and modeling approaches," *Materials Science in Semiconductor Processing*, vol. 62, pp. 80 – 91, 2017.

[61] J. Carrete, B. Vermeersch, A. Katre, A. van Roekeghem, T. Wang, G. K. Madsen, and N. Mingo, "almabte : A solver of the space−time dependent boltzmann transport equation for phonons in structured materials," *Computer Physics Communications*, vol. 220, pp. 351 – 362, 2017.

[62] X. Cartoixà, L. Colombo, and R. Rurali, "Thermal rectification by design in telescopic si nanowires," *Nano Letters*, vol. 15, pp. 8255–8259, 12 2015.

[63] P. A. Stolk, H.-J. Gossmann, D. J. Eaglesham, D. C. Jacobson, C. S. Rafferty, G. H. Gilmer, M. Jaraíz, J. M. Poate, H. S. Luftman, and

T. E. Haynes, "Physical mechanisms of transient enhanced dopant diffusion in ion-implanted silicon," *Journal of Applied Physics*, vol. 81, no. 9, pp. 6031–6050, 1997.

[64] M. Tabbal, M. J. Aziz, C. Madi, S. Charnvanichborikarn, J. S. Williams, and T. C. Christidis, "Excimer laser processing of novel materials for optoelectronic and spintronic applications," *Proc. SPIE*, vol. 6458, pp. 645803–645803–12, 2007.

[65] J. Kaiser, T. Feng, J. Maassen, X. Wang, X. Ruan, and M. Lundstrom, "Thermal transport at the nanoscale: A fourier's law vs. phonon boltzmann equation study," *Journal of Applied Physics*, vol. 121, no. 4, p. 044302, 2017.

[66] J.-P. M. Péraud and N. G. Hadjiconstantinou, "Extending the range of validity of fourier's law into the kinetic transport regime via asymptotic solution of the phonon boltzmann transport equation," *Phys. Rev. B*, vol. 93, p. 045424, Jan 2016.

[67] J. Maassen and M. Lundstrom, "Steady-state heat transport: Ballistic-to-diffusive with fourier's law," *Journal of Applied Physics*, vol. 117, p. 035104, Jan. 2015.

[68] M. J. McLennan, Y. Lee, and S. Datta, "Voltage drop in mesoscopic systems: A numerical study using a quantum kinetic equation," *Physical Review B*, vol. 43, pp. 13846–13884, June 1991.

[69] N. Pottier, *Nonequilibrium Statistical Physics: Linear Irreversible Processes*. Oxford Graduate Texts, OUP Oxford, 2010.

[70] L. Vincent, R. Boukhicha, C. Gardès, C. Renard, V. Yam, F. Fossard, G. Patriarche, and D. Bouchier, "Faceting mechanisms of si nanowires and gold spreading," *Journal of Materials Science*, vol. 47, pp. 1609–1613, Feb 2012.

[71] J. Anaya, J. Jimenez, and T. Rodriguez, "Thermal transport in semiconductor nanowires," in *Nanowires* (X. Peng, ed.), ch. 11, Rijeka: IntechOpen, 2012.

[72] M. A. Hopcroft, W. D. Nix, and T. W. Kenny, "What is the young's modulus of silicon?," *Journal of Microelectromechanical Systems*, vol. 19, pp. 229–238, Apr. 2010.

[73] A. J. H. McGaughey and A. Jain, "Nanostructure thermal conductivity prediction by monte carlo sampling of phonon free paths," *Applied Physics Letters*, vol. 100, no. 6, p. 061911, 2012.

[74] S. F. Lombardo, S. Boninelli, F. Cristiano, I. Deretzis, M. G. Grimaldi, K. Huet, E. Napolitani, and A. La Magna, "Phase field model of the nanoscale evolution during the explosive crystallization phenomenon," *Journal of Applied Physics*, vol. 123, no. 10, p. 105105, 2018.

[75] G. V. Samsonov, ed., *Handbook of the Physicochemical Properties of the Elements*. Springer US, 1968.

[76] I. Zvára, *The Inorganic Radiochemistry of Heavy Elements*. Springer Netherlands, 2008.

[77] G. Götz, "Explosive crystallization processes in silicon," *Applied Physics A*, vol. 40, pp. 29–36, 5 1986.

[78] G. Calogero, D. Raciti, P. Acosta-Alba, F. Cristiano, I. Deretzis, G. Fisicaro, K. Huet, S. Kerdilès, A. Sciuto, and A. L. Magna, "Multiscale modeling of ultrafast melting phenomena," *npj Computational Materials*, vol. 8, Mar. 2022.

[79] A. S. P. A S. Okhotin and V. V. Gorbachev, "Thermophysical properties of semiconductors," 1972.

[80] J. S. Custer, M. O. Thompson, D. C. Jacobson, J. M. Poate, S. Roorda, W. C. Sinke, and F. Spaepen, "Density of amorphous si," *Applied Physics Letters*, vol. 64, pp. 437–439, Jan. 1994.

[81] S. Stiffler, P. Evans, and A. Greer, "Interfacial transport kinetics during the solidification of silicon," *Acta Metallurgica et Materialia*, vol. 40, no. 7, pp. 1617 – 1622, 1992.

Acknowledgements

Ackowledgements are always a tricky part of the thesis, in these three years I've encountered many special people that helped me grow as a scientist and as a person, and mentioning them all will be a hard task. Thanks to all my colleagues at CNR, Thanks Antonino, you're a role model on how to be a real scientist, thanks to Ioannis, Peppe, Gaetano and Domenica, the best work group I've ever worked with. Thanks to the other people around the CNR and mainly around the "Ex kitchen room". Thanks to my academic supervisor, Prof. Grimaldi and all the people from Unict, from my fellow PhD colleagues to all the guys from EPS Young minds Catania.Thanks to all my colleagues at LASSE, Karim, Bobby, Armand and Benoit, your hospitality and work ethics are truely amazing. Thanks to my parents, always ready to support me no matter what. Thanks to all my friends, you have been and still are the pillars of my life. Last but not least, thanks to Beatrice, in this difficult year you have been a light in the darkest days, safe land for a castaway, my best friend and my greatest love.